Experiments with dipole-allowed transitions in trapped ions

Valentin Batteiger

München 2011

Experiments with dipole-allowed transitions in trapped ions

Valentin Batteiger

Dissertation
an der Fakultät der Physik
der Ludwig–Maximilians–Universität
München

vorgelegt von
Valentin Batteiger
aus Miltenberg am Main

München, den 24. 06. 2011

Erstgutachter: Prof. Dr. Theodor W. Hänsch
Zweitgutachter: Prof. Dr. Dietrich Habs
Tag der mündlichen Prüfung: 25. Juli 2011

Kurzfassung

Magnesium findet sich unter den häufigsten Elementen im interstellaren Medium und liegt dort überwiegend in einfach geladener Form vor. Die dominierenden 3s-3p Linien werden entsprechend häufig in astrophysikalischen Spektren beobachtet und spielen bei der Untersuchung des Wertes der Feinstrukturkonstante im frühen Universum eine prägende Rolle. Die vorgelegte Dissertation beschreibt die Spektroskopie dieser Linien in einer Ionenfalle. Absolutfrequenzkalibrierung, die störungsarme Umgebung der Ionenfalle und eine neuartige Spektroskopiemethode ermöglichen eine präzise Messung. Die Übergangsfrequenzen beider Feinstrukturkomponenten in $^{24}Mg^+$ und $^{26}Mg^+$ wurden bestimmt, daraus ergeben sich die Isotopieverschiebung und die Feinstrukturaufspaltung. Diese Messwerte verkleinern die Unsicherheit vorangehende Literaturwerte um mehr als zwei Größenordnungen, die Isotopieverschiebung des $3s_{1/2}$-$3p_{1/2}$ Übergangs und die Isotopieverschiebung der Feinstrukturaufspaltung konnten erstmals bestimmt werden. Weiterhin werden Übergangsfrequenzen in $^{25}Mg^+$ und die Schwerpunktsfrequenz bei natürlicher Isotopenzusammensetzung abgeleitet. Somit ergibt sich ein detailliertes Bild des gesamten Feinstrukturdubletts, das mittlerweile als Referenzwert in spektroskopischen, astrophysikalischen und kernphysikalischen Messungen genutzt wird.

Im Zuge der spektroskopischen Messungen wurden unter dem Einfluß eines blauverstimmten Lasers unerwartete Schwingungen einzelner Ionen beobachtet. Eine Untersuchung ergab Parallelen zwischen diesem mechanischen Schwinger und Laseroszillatoren, außerdem konnte Phasensynchronisation mit einem äußerst kleinen periodischen Signal nachgewiesen werden.

Schließlich werden weitere Experimente mit Dopplergekühlten Ionen vorgeschlagen, unter anderem eine Zweifrequenz-Ionenfalle die komplexe, molekulare Ionen und leichte, laserkühlbare Ionen gemeinsam speichern könnte.

Abstract

Magnesium is among the most abundant elements in the interstellar medium and singly charged magnesium is the predominant form there. The strong 3s-3p fine-structure doublet is therefore a prominent feature in many astrophysical spectra and has substantial influence on studies of the value of the fine-structure constant in the early universe. This dissertation reports on precision spectroscopy of these lines. Absolute frequency determination in a quiet ion trap environment, and a novel spectroscopy method enabled an accurate measurement. The absolute frequencies of both fine-structure components in $^{24}Mg^{+}$ and $^{26}Mg^{+}$ were determined, isotope shifts and fine-structure splittings are deduced. The measured data improve previous literature values by more than two orders of magnitude. The isotope shift of the $3s_{1/2}$-$3p_{1/2}$ transition and the isotope shift of the fine-structure splitting were determined for the first time. $^{25}Mg^{+}$ transition frequencies and the center-of-gravity frequency for a composite line of natural isotopic abundance are evaluated. Hereby we provide detailed data for the whole spectroscopic feature, which is useful as reference for spectroscopic, astrophysical and nuclear physics measurements.

During our spectroscopic work we observed intriguing ion oscillations driven by blue-detuned laser light. An investigation of single-ion oscillations revealed an analogy of our mechanical ion oscillator with optical lasers, a phonon laser. Later we demonstrated phase synchronization of the ion oscillator to an external signal, which may be used for the detection of ultra-weak oscillatory forces.

Finally we propose future experiments on Doppler cooled, trapped ions. This includes a dual frequency trap which may store heavy ion species together with light atomic ions with convenient cooling transition.

Contents

1. Introduction

Resonance fluorescence of laser-cooled ions enabled the visual observation of single atomic particles about three decades ago [1]. To literally 'see atoms' was not only of great philosophical value. It also provided a unique cooling and detection tool for a variety of atomic physics experiments. Efficient fluorescence detection and laser cooling requires high scattering rate from strong cycling transitions, where the excited state rapidly decays back to the ground state. Consequently, spectroscopic measurements of the 3s-3p transitions in Mg^+ were among the first experiments on laser-cooled ions in the early 1980s [2, 3, 4].

But strong transitions are spectrally broad, which limits the precision of a spectroscopic experiment at a given signal-to-noise ratio. Another limitation comes from the cumulative back-action of many scattered photons on the motion of an ion. The equilibrium temperature will critically depend on the detuning of the laser frequency with respect to the atomic resonance. Below resonance (red detuning) we expect Doppler cooling to mK temperatures and fluorescence rates up to 100 MHz from a single particle. A laser tuned above resonance (blue detuning) will increase the motional energy, the ion evades the laser beam and no appreciable fluorescence is observed. The resulting line-shape distortions limited the precision of spectroscopy on strong transitions in trapped ions. These problems remained widely unsolved arguably because of additional technical limitations, like the absence of simple and accurate frequency calibration schemes in many laboratories and theoretical limitations, which did not allow to push predictions for many electron atoms beyond the precision of early spectroscopic work [2]. Meanwhile the situation has changed. Optical frequency synthesizers [5] facilitated experiments and basically removed the calibration uncertainty. Transition frequencies in few electron atoms like Li^+ [6] and Be^+ [7] are meaningfully predicted from first principles. Correction to many-electron atoms like isotopic shifts [8] and relativistic effects [9] surpass the measurement uncertainty of early spectroscopic experiments. One particular example for renewed interest in strong transitions are many-multiplet analyses of quasar absorption spectra [10]. The computational predictions of relativistic corrections and the statistical uncertainty of large astrophysical samples were pushed to new limits. The precision of laboratory reference data became the bottle-neck of fundamental astrophysical investigations [11]. This resulted in a renaissance of spectroscopy on strong transitions in trapped ions [12, 13, 14], where our spectroscopy method gives nowadays the most precise answer to the suppression of systematic effects [15].

Chapter 4 describes the main topic of this thesis, a precise calibration of the 3s-3p

fine-structure doublet in Mg^+ [16]. Our measurement provides an accurate reference for the transition frequencies and isotopic shifts. Since strong fluorescence is desired in many experiments we advertise our measurement as an accurate calibration of useful lines. The main motivation was to provide a laboratory reference for astrophysical spectra. The measured transitions play an integral role in the many multiplet analysis of quasar absorption spectra and our measurement helps to refine the mentioned quest for a space-time variation of the fine-structure constant [17] or studies of isotopic composition in different astrophysical objects [18, 19]. An example from a different field is deep UV Fourier transform spectroscopy, where absolute frequency measurements on bright magnesium lines are used for improved wavenumber calibration [20]. We also set stringent limits for numerical investigations of isotopic shifts [8, 21, 22] and enable investigations of nuclear charge distributions. A recent example from nuclear physics is an envisaged spectroscopic investigation of the $^{21-32}$Mg isotopic chain, where our benchmark measurement on stable Mg^+ isotopes helped to resolve voltage calibration issues at the ISOLDE beam line at CERN [23]. These examples indicate that future applications may follow.

In addition to the line center measurements we present an investigation of the upper-state lifetime from the spectral width of the 3s-3p transitions. The statistical uncertainty of our preliminary lifetime measurement improves the most accurate results from measurements in the time-domain, but a number of systematic effects require further investigations.

A widely unattended topic has been the effect of blue-detuned laser radiation on the motion of trapped ions. During our spectroscopic work we observed intriguing ion oscillations, which were caused by the interplay of a red- and a blue-detuned laser beam. In a series of experiments we interpreted a blue-detuned laser as a source for amplification of ionic motion in the trap potential. An investigation of single, oscillating ions revealed an analogy of our mechanical ion oscillator to optical lasers, a phonon laser [24]. We demonstrated phase synchronization of the ion oscillator to an external signal, which may be used for the detection of ultra-weak oscillatory forces [25]. An overview on our ion oscillator experiments is given in Chapter 5.

Finally, I propose further experiments with Doppler cooled ions for the near future. Measurements on transitions of fundamental interest in Beryllium ions (Section 6.1), a proposal of a dual-frequency ion trap, which is capable to store sympathetically cooled ions with large mass differences (Section 6.2) and a proof-of-principle measurement on dipole-allowed transitions with a deep UV frequency comb (Section 6.3).

Manuscripts in peer-reviewed journals

- **Injection locking of a trapped-ion phonon laser**
  S. Knünz, M. Herrmann, V. Batteiger, G. Saathoff, T. W. Hänsch, K. Vahala and T. Udem
  Physical Review Letters **105**, 013004 (2010)

- **A phonon laser**
  K. Vahala, M. Herrmann, S. Knünz, V. Batteiger, G. Saathoff, T. W. Hänsch and T. Udem
  Nature Physics **5**, 682 (2009)

- **Feasibility of coherent xuv spectroscopy on the 1s-2s transition in singly ionized helium**
  M. Herrmann, M. Haas, U. D. Jentschura, F. Kottmann, D. Leibfried, G. Saathoff, C. Gohle, A. Ozawa, V. Batteiger, S. Knünz, N. Kolachevsky, H. A. Schüssler, T. W. Hänsch and T. Udem
  Physical Review A **79**, 052505 (2009)

- **Precision spectroscopy of the 3s-3p fine structure doublet in Mg^+**
  V. Batteiger, S. Knünz, M. Herrmann, G. Saathoff, H. A. Schüssler, B. Bernhardt, T. Wilken, R. Holzwarth, T. W. Hänsch and T. Udem
  Physical Review A **80**, 022503 (2009)

- **Frequency Metrology on Single Trapped Ions in the Weak Binding Limit: The $3s_{1/2}$-$3p_{3/2}$ Transition in $^{24}Mg^+$**
  M. Herrmann, V. Batteiger, S. Knünz, G. Saathoff, T. Udem and T. W. Hänsch
  Physical Review Letters **102**, 013006 (2009)

2. Basic ion trapping and interactions with laser light

Radio-frequency (RF) ion traps and linear quadrupole mass filters were first developed in the group of Wolfgang Paul in the early 1950's. These visionary concepts were based on experiences with molecular beam and accelerator physics [26]. Linear quadrupole devices found widespread applications in the field of mass spectrometry. Early Paul traps followed a three-dimensional quadrupole approach, with electrode surfaces resembling the equipotential planes as close as possible. Fundamental drawbacks with this design are limited optical access and the cancellation of RF fields at only one point in the middle of the trap. Linear RF traps with axial DC enclosure were pioneered in the late 1980's [27, 28, 29] and quickly became a standard tool for most ion trap experiments. The ideal quadrupole shape of the electrodes was commonly sacrificed for obtaining better optical access to the trap center, since laser cooling [30, 31] and fluorescence detection [32] had become integral parts of virtually all ion trap experiments. The capability to store single, laser-cooled atoms almost at rest in free space enabled spectroscopic measurements and atomic clocks at an utmost precision [33]. The demonstration of laser cooling to the motional ground state [34, 35] and the proposal of the Cirac-Zoller gate in 1995 [36] triggered an ongoing 'quantum revolution' in the field [37]. Di Vincenzo's scalability criterium for the physical implementation of quantum computation [38] inspired many groups to design micro-structured traps and also surface traps, where integrated electrodes create local quadrupolar RF potentials above a chip [39, 40]. However, the advantages of those miniaturized traps are accompanied with technical difficulties, like enhanced heating rates and insulating surfaces close to the trapping regions. Precision traps, e.g., for the nowadays best atomic clock [41] and most impressive gate fidelities [42] step back to more conservative linear quadrupole approaches.

2.1. A single charged particle in a linear RF trap

Ion dynamics in RF traps are usually treated for a single charged particle trapped in quadrupolar static (DC) and dynamic (RF) electric fields. An analytic solution exists and simple approximations for the ion trajectory can be found for a certain range of parameters. The spectroscopy method described in Section 4.2 is based on

one-dimensional chains of 8-10 ions in a linear quadrupole trap. The Coulomb interaction between charged particles prevents an analytical solution for multiple ions. Since the ion dynamics along the principal axes of the trap are widely decoupled, we approximate the radial confinement of each ion in the chain as single particle dynamics in RF electric fields (Section 2.1.1). The dynamics along the trap axis will be approximated by an ensemble of charged particles held by a one-dimensional harmonic potential well (Section 2.3.2).

2.1.1. Radial confinement

Here we will summarize the standard treatment for radial RF confinement, technical details can be found in many manuscripts (e.g. [43],[44]). Dynamic trapping is necessary since the Laplace equation $\Delta\Phi = 0$ has to be fulfilled at any instant of time. This excludes an electrostatic potential minimum in three dimensions (Earnshaw's theorem). The radial potential for an ideal linear RF quadrupole trap reads [43]

$$\Phi(x, y, t) = \frac{1}{4r_0^2}(U_{\mathrm{dc}} + U_{\mathrm{rf}} cos(\Omega t))(x^2 - y^2), \tag{2.1}$$

where r_0 measures the minimal distance from the trap center to the electrode surfaces. Besides the sinusoidal driving voltage U_{rf} with frequency Ω we include an additional static quadrupole potential characterized by U_{dc}. The static quadrupole potential is unstable by its nature. When applied it reduces the stability either in x or y direction. A static quadrupole is therefore unwanted in most ion trap experiments and U_{dc} is usually set to zero. The proposal in Section 6.2 marks one of few exceptions. However, it finds application in linear quadrupole mass filters, since the electrostatic potential couples to the charge of the particle only, while the RF pseudo-potential is intrinsically dynamic and its strength is therefore mass dependent. This allows to set the parameters such that only a selected charge-to-mass ratio may pass a filter. The (historical) reference to quadrupole mass filters is not the only reason for keeping the static term in ion trap physics. Stability diagrams like the one depicted in Figure 2.1 indicate the parameter region where an RF trap is robust against destabilizing stray fields, even if they are usually not quadrupolar. Equation (2.1) is decoupled in the spatial coordinates, so we restrict the treatment to one dimension. From Newton's equation we obtain the equation of motion for a particle of mass m and charge Q

$$m\ddot{x} = -Q\frac{\partial\Phi(x, y, t)}{\partial x} = -\frac{Q}{2r_0^2}(U_{\mathrm{dc}} + U_{\mathrm{rf}} \cos(\Omega t))x, \tag{2.2}$$

which can be transformed into a Mathieu-type differential equation

$$\frac{d^2x}{d\xi^2} + (a - 2q\cos 2\xi)x = 0, \tag{2.3}$$

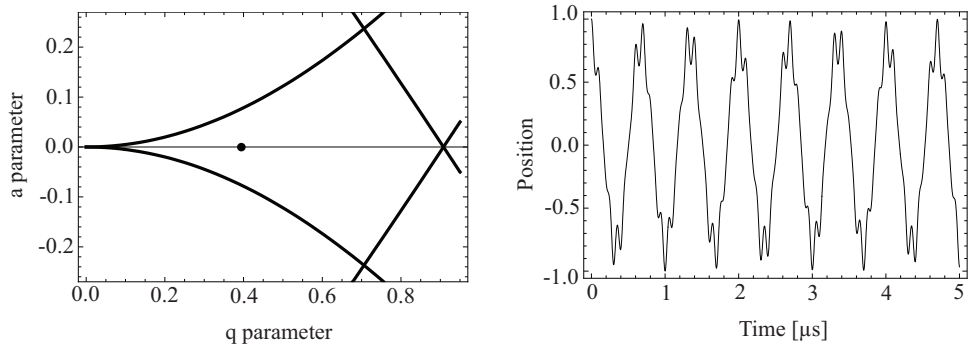

Figure 2.1.: Left: Lowest-order stability diagram of a linear quadrupole RF trap. The solid lines represent the boundaries of the stable range of a and q parameters in x and y direction. The trajectory on the right corresponds to $q = 0.4$, $a = 0$ (black dot). The initial amplitude was set to 1, the trajectory was integrated over 50 cycles of a radio frequency signal at $\Omega/2\pi = 10$ MHz. The dominating secular motion and the superimposed micro-motion are visible.

with the substitutions

$$a := \frac{4QU_{\mathrm{dc}}}{m\Omega^2 r_0^2}, \qquad q := \frac{2QU_{\mathrm{rf}}}{m\Omega^2 r_0^2}, \qquad \xi := \frac{\Omega t}{2}. \tag{2.4}$$

a and q are dimensionless 'stability' parameters characteristic to the static and the dynamic part of the potential, while ξ measures time in units of the driving frequency. A general solution to the Mathieu equation can be obtained via Floquet's theorem. The derivation is rather technical and not particularly instructive (see e.g. [43, 44]). One insight is that stable solutions occur when the stability parameters a and q fall within certain regions in parameter space. The lowest order stability region, this is the region which contains the case of infinitesimally small stability parameters, is depicted in Figure 2.1.
We drop the static quadrupole, $a = 0$, and give an approximation for the ion trajectory for $q^2 \ll 1$

$$x(t) \approx x_0[1 - \frac{q}{2}\cos(\Omega t)]\cos(\frac{q\Omega}{\sqrt{8}}t). \tag{2.5}$$

Equation 2.5 reveals two distinctive frequency components. The so-called 'micro-motion', a driven quiver with frequency Ω and a new frequency component, which dominates the ion dynamics and is commonly denoted as 'secular frequency'[1]

$$\omega_s \approx \frac{q}{\sqrt{8}}\Omega = \frac{Q}{m}\frac{U_{rf}}{\sqrt{2}\Omega r_0^2}. \tag{2.6}$$

[1]The term 'secular' reflects the long duration of an oscillation cycle with respect to the much faster micro-motion.

Equation (2.6) implies that co-stored ion species with different charge-to-mass ratio will oscillate at different secular frequencies. Resonant excitation of secular frequencies can be utilized for mass spectroscopy, purification of an ensemble from unwanted ion species or isotope selective trap loading techniques (Section 3.3.3). It also implies that species with different charge-to-mass ratio see different time-averaged pseudo-potentials

$$\Phi = \frac{1}{2} m \omega_s^2 x^2. \tag{2.7}$$

From the pseudo-potential approximation we estimate the potential depth of a Paul trap. Typical secular frequencies are in the $\omega_s/2\pi = 1$ MHz regime, with $m = 24$ amu for Mg^+ and $x_0 = r_0 = 1$ mm we obtain a potential energy, which corresponds to a mean kinetic energy equivalent to an ion temperature of 38000 K. Therefore, ion traps are capable to store atomic ions at room temperature. Given appropriate vacuum conditions only rare events may expel an ion from such a trap. Equation 2.7 scales with ω_s^2, in our example we approach a trap depth corresponding to room-temperature at $\omega_s/2\pi = 90$ kHz, which illustrates the need for high drive frequencies and correspondingly high voltages when trapping light atomic ions (Section 3.2.4).

2.1.2. Axial confinement

Axial confinement in linear ion traps is usually achieved by an electrostatic potential in z-direction. Common realizations of axial DC potentials include: Neighboring segments at positive DC voltage (Section 3.2.2), ring-shaped electrodes around the RF electrodes (Section 3.2.3) and endcap electrodes at both sides of the trap [42]. The DC fields from symmetric electrodes cancel at the trap center and the potential in the vicinity is harmonic in leading order. The characteristic oscillation frequency associated with the axial potential

$$\omega_{\mathrm{ax}} \propto \sqrt{\frac{Q U_{\mathrm{ax}}}{m}}, \tag{2.8}$$

depends on the charge Q and the mass m of a particle and the voltage U_{ax} applied to the enclosing electrodes. The axial oscillation frequency is often called 'axial secular frequency', yet it is of different nature than the radial secular frequency in the RF pseudo-potential. For pure DC enclosure it is free of micro-motion and the restoring force depends only on the charge state of the trapped particle. The trap depth at a given voltage is mass independent and the equilibrium positions of multiple ions along the trap axis depend solely on their charge. Yet it is possible to identify different species dynamically by RF excitation of their axial frequencies. The axial equilibrium distance d_{eq} between two identical ions in a harmonic potential is given by the balance of the Coulomb repulsion and the restoring force

$$d_{\mathrm{eq}}^3 = \frac{Q^2}{2\pi\epsilon_0 m \omega_{\mathrm{ax}}^2}. \tag{2.9}$$

It depends on known constants and the axial secular frequency ω_{ax}, which is experimentally accessible via resonant RF excitation. We typically operate our trap at $\omega_{ax}/2\pi = 70$ kHz for $^{24}Mg^+$ and obtain a distance of 39 μm between two singly charged ions. This distance measure in the trap enables an accurate calibration of our imaging optics (Section 3.4), which was crucial for the measurements reported in Chapter 5. The resolution of commonly used imaging systems is below 2 μm, inter-ionic distances in the 10 μm regime enable site-resolved detection of single atomic ions in a crystallized structure [45].
The finite length of the electrodes causes a residual axial RF enclosure in linear traps. The magnitude of the residual RF enclosure depends on the geometry of the trap and on the applied RF signal (Section 3.2.4).

2.2. Atomic physics background

2.2.1. The spectrum of Mg^+

Precise computations of energy eigenstates and wave functions in many-electron atoms is a formidable task. Many-body perturbation theory reproduces the energy levels in Mg^+ with 0.2% accuracy [9], which may be compared to $1.5{\cdot}10^{-10}$ fractional uncertainty of our absolute frequency measurement (Section 4.3). Singly charged magnesium ions have one valence electron and show an alkali-like level structure with the ground state configuration [Ne] $3s^1$. Figure 2.2 shows the electronic spectrum of Mg^+, basic features are qualitatively explained from intuitive considerations.
Alkali-like atoms may be viewed as one-electron systems in an effective potential created by the nuclear charge Z and a number of N screening electrons in a radially symmetric closed-shell configuration. The effective potential in the vicinity of the nucleus approximates the Coulomb potential of the bare nuclear charge Z, while it approaches a Coulomb potential of charge $Z - N$ for large distances. The potential deviates from the hydrogenic $1/r$ potential and degeneracy with respect to the orbital angular momentum quantum number l is therefore no longer valid, while radial symmetry is preserved and induces m_l degeneracy. The probability to find the valence electron close to the nucleus decreases with l. Therefore we find, for small principal quantum numbers n, that states with low l have considerably higher binding energy.
The valence electron has spin 1/2 and all levels besides the s-states (l=0) are split into doublets by spin-orbit coupling. The most famous alkali doublet is the 3s-3p fine-structure doublet at 589 nm in sodium, historically labeled as D_1 ($3s_{1/2}$-$3p_{1/2}$) and D_2 ($3s_{1/2}$-$3p_{3/2}$) Fraunhofer lines. We adopt this notation for the corresponding 3s-3p transitions in the isoelectronic Mg^+ ion.
Magnesium has three stable isotopes ^{24}Mg, ^{25}Mg and ^{26}Mg (natural abundances

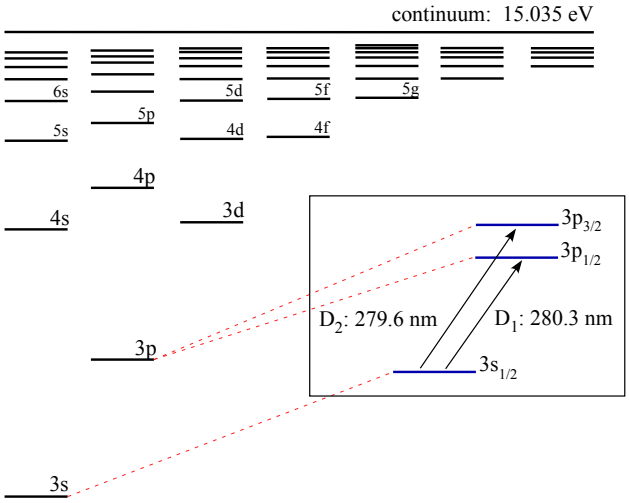

Figure 2.2.: The electronic spectrum of Mg^+ is typical for an alkali atom. All states correspond to the excitation of a single valence electron, transitions are dipole-allowed when $|\Delta l| = 1$. States with low angular momentum quantum number l are tightly bound since the electron wave function penetrates the shielding neon configuration of the atomic core. This effect decreases at higher principle quantum number n and the spectrum gets hydrogenic towards the Rydberg states. All states with angular momentum $l > 0$ are split into fine-structure doublets by spin-orbit coupling. The strongest lines in the spectrum are the 3s-3p transitions. These lines are isoelectronic to the 3s-3p doublet in sodium, historically labeled as D_1 and D_2 Fraunhofer lines. We adopt this notation.

79:10:11). ^{24}Mg and ^{26}Mg isotopes are even-even nuclei without nuclear spin $I = 0$, while ^{25}Mg has nuclear spin $I = 5/2$. The differences in nuclear mass, charge distribution and nuclear magnetic moment influence the energy eigenstates of the atom. For the resulting isotopic shifts and hyperfine structure splittings we refer to Sections 4.5 and 4.6.

2.2.2. Dipole transitions

The transitions between s-states and p-states in alkali systems fulfill the selection rules for dipole-allowed transitions. Thus, transitions from alkali ground states to the first excited p-state are strong cycling transitions, where a single excited state rapidly decays back to the ground state (Figure 2.2). Such transitions are suitable for Doppler cooling and fluorescence detection in atomic physics experiments. Most features of dipole-allowed cycling transitions can be deduced from the two-level atom. This semi-classical model for atom-light interaction can be found in many atomic physics textbooks, we review basic results for following sections.
The two-level atom consists of the ground state and one excited level with an energy

difference $\hbar\omega_0$ between them. A narrow-band laser is modeled by the light field $E = E_0 \cos[(\omega_0+\delta)t]$, where the detuning $\delta = \omega-\omega_0$ measures the difference between the laser frequency ω and the atomic resonance frequency ω_0. The probability to find the atom in the excited state oscillates on resonance ($\delta = 0$) between 0 and 1 with the resonant Rabi frequency $\Omega_0 = d_{\mathrm{eg}}E_0/\hbar$. The Rabi frequency is given by the electric field amplitude of the light field E_0 and therefore depends on the intensity of the laser beam. Theoretical investigations of transition dipole moments $d_{\mathrm{eg}} = <\mathrm{e}|\widehat{d}\,|\mathrm{g}>$ are usually elaborate, since electron wave functions in many-electron atoms need to be known. The transition dipole moment can also be expressed in terms of the Einstein A coefficient, which is identical with the spontaneous decay rate Γ in a two-level system and often experimentally accessible

$$\Gamma = \frac{1}{\tau} = A = \frac{d_{eg}^2\omega_0^3}{3\pi\epsilon_0\hbar c^3}. \tag{2.10}$$

Spontaneous emission quenches the coherent Rabi oscillations at random instants in time, where the mean decay rate is given by the inverse upper state lifetime $\Gamma = 1/\tau$. The two-level system remains no longer in a pure quantum state, the time-evolution can be described by the density matrix of the system

$$\hat{\rho} = \begin{pmatrix} \rho_{11} & \rho_{12} \\ \rho_{21} & \rho_{22} \end{pmatrix}, \tag{2.11}$$

and is given by damped optical Bloch equations. The inversion $w = \rho_{22} - \rho_{11}$ is defined as the difference between the excited state and the ground state population[2]. In equilibrium ($t \gg \tau$) it is given by $w = -1/(1+S)$ with the saturation parameter S defined as

$$S := \frac{\Omega_0^2/2}{\delta^2 + \Gamma^2/4}. \tag{2.12}$$

The saturation parameter on resonance is $S_0 = 2\Omega_0^2/\Gamma^2$ and we define an intensity measure $S_0 := I/I_{sat}$, which is characteristic to the involved atomic transition. $S_0 = 1$ corresponds to the saturation intensity at wavelength λ and excited state lifetime τ

$$I_{\mathrm{sat}} := \frac{\pi hc}{3\lambda^3\tau}. \tag{2.13}$$

For the D_2 transition in Mg^+ we find $I_{\mathrm{sat}} = 2497\ \mathrm{W/m^2}$ ($\tau = 3.81(4)$ ns [46]). The upper state population ρ_{22} at equilibrium is

$$\rho_{22} = \frac{1}{2}(1+w) = \frac{S}{2(1+S)} = \frac{S_0/2}{1+S_0+4\delta^2/\Gamma^2}. \tag{2.14}$$

We infer the fluorescence rate $\gamma = \Gamma\rho_{22}$ from the mean upper state occupation times the decay rate. On resonance, we find a fluorescence rate of $\Gamma/4$ at saturation

[2] $w = -1$ corresponds to the ground state, 1 to the excited state

intensity and approximately $\Gamma/2$ for large saturation parameters. For the 3s-3p transitions in Mg^+ we obtain a maximum scattering rate of 130 MHz, which enables bright fluorescence detection of single atoms. From the scattered intensity at low saturation parameter one obtains the resonant scattering cross section of a dipole-allowed transition

$$\sigma = \frac{3\lambda^2}{2\pi}. \tag{2.15}$$

We may rewrite the steady state fluorescence rate $\gamma = \Gamma\rho_{22}$ and obtain

$$\gamma_L(\delta) = \Gamma\rho_{22} = \frac{S_0}{1+S_0}\frac{\Gamma/2}{1+4\delta^2/\Gamma'^2} \text{ where } \Gamma' = \Gamma\sqrt{1+S_0}. \tag{2.16}$$

The index in $\gamma_L(\delta)$ reflects the Lorentzian spectrum of the fluorescence rate as a function of the detuning δ. The linewidth of the Lorentz profile depends on the decay rate Γ and the intensity of the illuminating laser beam. The natural linewidth of the D_2 transition in Mg^+ has a full width at half maximum of $\Gamma/2\pi = 41.8$ MHz. The fluorescence rate in a real experiment will also depend on the velocity of the atom, since the Doppler effect shifts the laser frequency in the rest frame of the atom. The spectral width of a thermal ensemble of atoms of mass m at temperature T due to Doppler broadening is [47]

$$\Delta\omega_D = \sqrt{\frac{8\ln 2\ k_B T\omega_0^2}{mc^2}}, \tag{2.17}$$

where ω_0 is the transition frequency at rest. The corresponding fluorescence rate, often denoted as Doppler profile is Gaussian

$$\gamma_D(\delta) = \sqrt{\frac{4\ln 2}{\pi\Delta\omega_D^2}}\exp\left[\frac{-4\ln 2\ \delta^2}{\Delta\omega_D^2}\right]. \tag{2.18}$$

The Doppler broadening for the 3s-3p transitions in $^{24}Mg^+$ is 2.7 GHz at 300 K and 5 MHz at 1 mK. The resulting fluorescence rate at a certain temperature T is given by a Voigt type absorption spectrum, which is a convolution of the Lorentzian response of the atom at rest and the Gaussian Doppler broadening. An analytic expression for the convolution integral does not exist, it can be expressed in terms of the complex error function, which we use for our line shape models.
Finally we note that the two-level system is a semi-classical model and provides a simplified derivation of basic light-atom interactions. The fluorescence rate at low laser intensity $I \ll I_{\text{sat}}$ is, for example, dominated by resonant Rayleigh scattering and may be viewed as an elastic redistribution of photons, rather than inelastic scattering via excitation and decay of an excited state.

2.2.3. Laser cooling

The random redistribution of near-resonant photons results in a radiation pressure on the scattering atom, since the cumulative momenta $\hbar k$ of highly directed photons from a laser beam are transfered to the atom, while the net-momentum of the nearly isotropically scattered photons averages to zero. At a scattering rate γ we obtain a mean radiation pressure force $|F| = \hbar k\gamma$, which can be used to cool the motion of an atom [48, 49]. The frequencies of two counter-propagating laser beams are set to red detuning ($\omega < \omega_0$) in a field free general case. An atom with a velocity component towards one of the laser beams can shift in resonance with the opposing laser due to the Doppler effect, while it is shifted out of resonance with its counterpart. Scattering events are therefore more likely from the counter-propagating laser beam, so the decelerating radiation pressure against the atom's direction of motion surpasses the accelerating pressure in the direction of motion. The result is a net-damping of the velocity component, which is usually referred to as Doppler cooling. Efficient Doppler cooling from several hundreds of Kelvin to the milli-Kelvin regime requires closed-level schemes with a high scattering rate, like the strong 3s-3p cycling transitions in Mg^+. With regard to Chapter 5 we remark that blue-detuned laser beams ($\omega > \omega_0$) will have the opposite effect, scattering is more likely when the atom moves in the propagation direction of a blue detuned laser beam. The net result is positive feedback on the existing motion (see Chapter 4.1 in [50]).

Laser cooling in a harmonic trap

The case of Doppler cooling in a harmonic trapping potential is reviewed in [43]. Here a single laser beam can provide cooling, since the restoring potential reverses the motion and fills the role of the counter-propagating laser. This argument also holds for three-dimensional cooling, given a non-zero projection of the single laser beam onto all trap axes.
The oscillatory motion of the ion in the trap potential will in general modify the energy eigenstates of the atom-trap system and generate a sideband structure at the trap frequencies. This sideband structure gets washed out, once the oscillation frequency in the trap is smaller than the linewidth of the atomic transition, $\omega_s \ll \Gamma$ [51]. In the frequency domain this corresponds to an unresolved sideband structure. In the time domain the coherence time associated with the scattering event is much shorter than the oscillation period in the trap. This regime is commonly called weak binding or unresolved sideband limit and the absorption spectrum is well described by a Voigt profile, similar to an ensemble of unbound atoms [51].
In present experiment we create a Mg^+ ion by photo-ionization of a Mg atom within the trapping volume (Section 3.3). The Doppler shift of several hundreds of Kelvin is about two orders of magnitude larger than the natural linewidth of the cooling

transition and the mean velocity corresponds to several hundreds of m/s. In the case of unbound atoms efficient cooling requires a fast tuning of the resonance frequency, e.g., in a Zeeman slower [52]. The storage time in an ion trap is virtually unlimited and a hot ion on a classical trajectory moves with slow velocities at the turning points of the oscillation. It is convenient to keep a single cooling laser beam at fixed (red) detuning and simply wait until the ion is cooled to mK temperatures [30, 31]. The temperature limit for Doppler cooling is given by an equilibrium condition between the velocity-dependent cooling process and stochastic heating by random recoil kicks associated with each scattering event. The cooling limit is evaluated in [43] for a low saturation parameter S_0 and a purely harmonic trap potential. It is given by the cycle-averaged cooling power

$$\langle P_c \rangle = \langle \hbar k \gamma_L(S_0, \delta(t)) v_0 \cos(\omega_s t) \rangle, \tag{2.19}$$

in balance with the cycle-averaged heating power from spontaneous emission kicks

$$\langle P_s \rangle = \langle \frac{7\hbar^2 k^2}{10m} \gamma_L(S_0, \delta(t)) \rangle, \tag{2.20}$$

where γ_L reflects the Lorentzian scattering rate (Equation 2.16), while the time dependent detuning $\delta(t)$ takes the ion's motion into account.
An expression for the equilibrium temperature can be obtained in the limit of small velocities, where the residual Doppler broadening $\Delta\omega_D$ (Equation 2.17) is small compared to the natural linewidth Γ of the cooling transition [43]

$$k_B T = \frac{7\hbar\Gamma}{40} \left[(1 + S_0) \frac{\Gamma}{2\delta} + \frac{2\delta}{\Gamma} \right]. \tag{2.21}$$

In the limit of a vanishing scattering rate, $S_0 \to 0$ we obtain a minimum equilibrium temperature of $7\hbar\Gamma/20k_B$ at a detuning $\delta = \Gamma/2$. The prefactor 7/20 is due to the non-isotropic emission pattern of a dipole transition. The minimum equilibrium temperature at a non-vanishing saturation parameter is higher and shifted to larger detunings (Figure 2.3). In our experiments we set the detuning to $\delta = 3\Gamma/2$ where we find stable long-term operation at slightly increased equilibrium temperature.
Doppler cooling limits are given by the linewidth Γ of the cooling transition. For the D_2 transition in Mg^+ ($\Gamma/2\pi = 41.8$ MHz [46]) we find $T_{\min} = 0.7$ mK, the mean thermal energy $k_B T_{\min}$ corresponds to the energy $\hbar\omega_s$ of 15 vibrational quanta at a secular frequency $\omega_s/2\pi = 1$ MHz. Further cooling to the quantum mechanical ground state of motion in the trap potential is possible with various cooling schemes [43]. Ground state cooling is required in many ion trap experiments for initial quantum state preparation. Our aim is different, the long term goal of our ion trap project is a proposed 1s-2s spectroscopy experiment in He^+. In [53] we have shown that the signal rate for this experiment is optimized at 1.3 mK. For this reason we proceed without ground state cooling and focus on experiments with Doppler-cooled ions.

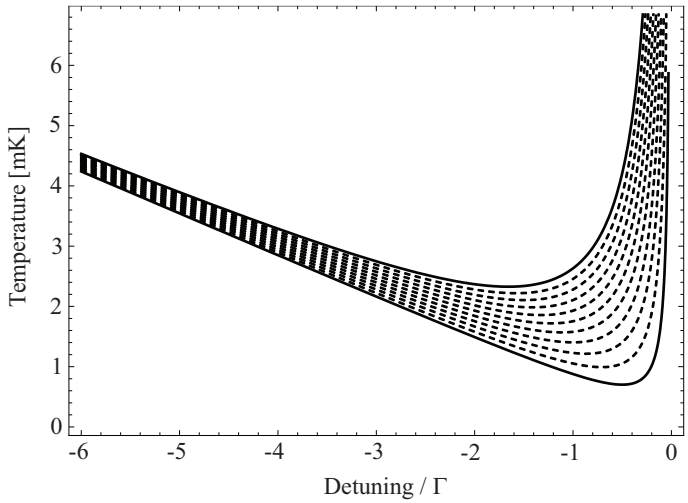

Figure 2.3.: Equilibrium temperature according to Equation 2.21 for Doppler cooling on the D_2 transition in Mg^+. The detuning $\omega - \omega_0$ is given in units of the linewidth $\Gamma/2\pi = 41.8$ MHz, while temperatures are converted to mK. In the limit of small intensity $S_0 \to 0$ we obtain a minimum temperature of 0.7 mK at a detuning of $\Gamma/2$. Dashed lines represent a stepwise increase of one saturation intensity, the upper thick curve corresponds to $S_0 = 10$. The temperature diverges for $\omega \to \omega_0$, since the cooling power decreases and heating by spontaneous emission kicks dominates. Our spectroscopy method [15] removes this limitation by sympathetic cooling (Figure 4.3).

2.3. Laser-cooled ions in the trap potential

2.3.1. Motion of a laser-cooled ion

In Section 2.1 we treated the trajectory of a single ion in the trap potential as an undamped oscillatory motion of a classical point mass. This motion is now damped by radiation pressure and a cooling limit is found at an equilibrium of the stochastic damping process with stochastic recoil events (Section 2.2.3). This stochastic motion may be viewed as Brownian motion of a classical particle in a harmonic potential, which results in a Gaussian distribution of the time-averaged ion position [54], see also [55] and Section 3.2.1. in [56] for further details. The root-mean-square displacement[3] z_{rms} from the trap center can be estimated from the thermal energy at the ion's equilibrium temperature

$$k_B T = m\omega_{\mathrm{ax}}^2 z_{\mathrm{rms}}^2. \tag{2.22}$$

In our four-rod trap (Section 3.2.3) we can decrease the axial trap frequency to few kHz and resolve the time-averaged distribution of the ion position (Figure 2.4) with

[3] The root-mean-square displacement of a Gaussian distribution corresponds to $1/(2\sqrt{2\ln 2})$ times the full width at half maximum.

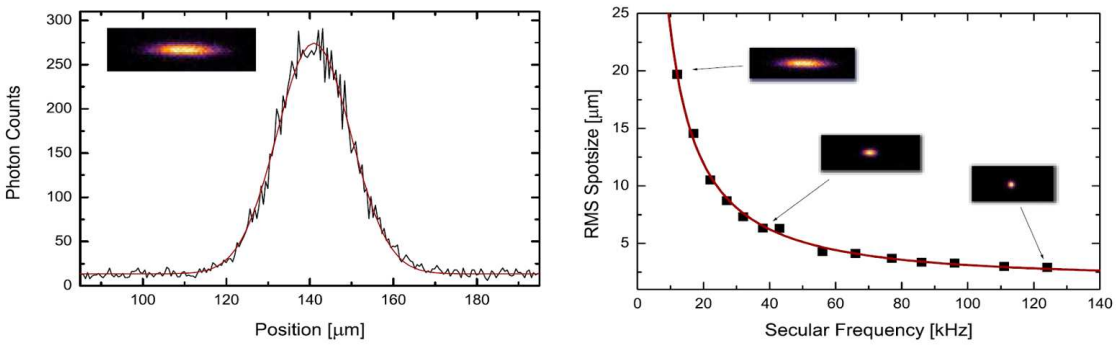

Figure 2.4.: Thermal distribution of the position of a single, laser cooled ion in a harmonic trap potential. Left: We lower the axial trap potential until the thermal spread is clearly resolved by our imaging optics. We find a thermal distribution, which is well described by a Gaussian. Right: We fit Equation 2.22 to the thermal spread at different axial secular frequencies. From the fit we obtain the ion temperature 1.1(1) mK and the point spread function of our imaging system 1.7(1) μm (see Section 3.2.1. in [56] for further details).

our imaging optics (Section 3.4). We can also vary the detuning of the cooling laser (change in temperature T according to Equation 2.21) or the strength of the axial trap frequency ω_{ax} and observe the change in z_{rms} from images of single ions. Least-square-fits of Equation 2.22 to the data reveal the 'temperature' associated with the position distribution of the ion and the point-spread-function of our imaging optics (see Section 3.2.1. in [56]).

2.3.2. Crystallized ion chains

Our spectroscopy experiment is based on crystallized chains of laser-cooled ions (Section 4.2). The radial confinement of each individual ion in the chain may be viewed as single-particle confinement in a RF potential (Section 2.1). In axial direction we treat the ions as a number of charged particles located in a one-dimensional harmonic potential. A minimization of the potential energy enables a numerical determination of the equilibrium positions for a chain of N ions [57]. The dynamics of such a chain are given by the N eigenmodes of the system. Normalized relative displacements are listed for small excursion from the equilibrium positions in Table II in [57]. Displacement amplitudes are shown for a chain of five ions in Figure 2.5. Each ion resides in its individual potential well and small displacements translate into small velocity amplitudes. For a given eigenmode we expect that the efficiency of a velocity-dependent damping process, like Doppler cooling, will in general depend on the particular site of a laser-cooled ion in a chain. For our spectroscopic measurements we trap chains of 8-10 ions. We laser-cool 2-3 ions at one end of the chain and perform spectroscopy on 2-3 ions at the opposite end of the chain

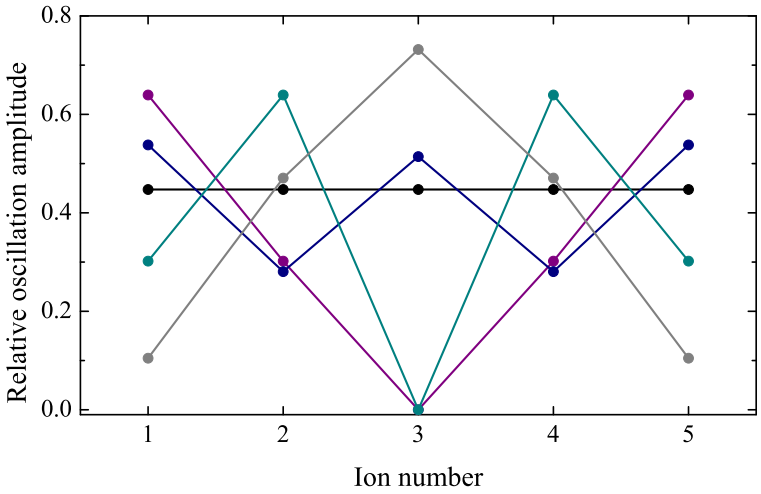

Figure 2.5.: Normalized relative displacement amplitudes, for small excursion from the equilibrium positions in a one-dimensional chain of five ions (from Table 2 in [57]). The relative displacements translate into velocity amplitudes. Velocity amplitudes reveal how efficient a certain eigenmode is Doppler-cooled when we address a certain subset of ions with a cooling laser. The apparent symmetry results in strong motional coupling of symmetric ions along the chain. The center ion does not move for two breathing-type eigenmodes, but dominates one eigenmode (grey), which is not efficiently cooled by the outer ions. From this behavior we draw the following conclusions: Ions at opposite ends of the chain participate with equal strength to each particular eigenmode, sympathetic cooling is most efficient here, while the dominant eigenmodes for center ions are less efficiently coupled to ions at either end of the chain.

(Section 4.2). The motion of cooling and spectroscopy ions is tied to each other for symmetry reasons, i.e. they show equal velocity amplitude for each eigenmode. A molecular dynamic simulation by Thomas Udem confirmed that the temperature under cooling and spectroscopy of ions at both ends of the chain is identical for typical parameters of our experiment (Figure 4.3). Sympathetic cooling of center ions is less efficient, since certain eigenmodes are less efficiently damped at the sites of the coolant ions (Figure 5.1).

3. Experimental setup

In this chapter we give a description of our experimental setup. Most components were also discussed in the preceding theses by Maximilian Herrmann [50] and Sebastian Knünz [56]. These works include, e.g., a detailed description of our vacuum system, our ion traps and our imaging optics. Here we will only give an overview and references to respective chapters in the aforementioned theses. On the other side we will give a more extensive description of other constituents like the laser systems and selected topics like photo-ionization. The chapter is not balanced as a consequence, unless it is viewed as complementary to prior work.

3.1. Laser systems

To create, cool and manipulate Mg^+ ions, we run laser systems at different UV wavelengths: Light at 285 nm for resonant photo-ionization of neutral Mg atoms and light at 280 nm to address the 3s-3p dipole-allowed transitions in Mg^+. We use a frequency-quadrupled fiber laser and dye laser systems. Over time we further developed and modified our laser apparatus in response to technical issues and experimental requirements.

3.1.1. Fiber laser system

The heart of the fiber laser system [58] is a commercial ytterbium fiber laser, which was specified to emit 2 W single-frequency radiation at 1118 nm (Koheras Boostik). It incorporates a fiber laser oscillator with a fiber Bragg grating as frequency-selective element. The oscillator operates on a single-frequency mode and can be run as a convenient 'turn key system'. Coarse tuning of the laser frequency is achieved by a temperature change of the active fiber, while fine tuning and feedback is applied by a piezoelectric actuator, which stretches the fiber. The tuning range is limited to 90 GHz and our fiber laser can only address the D_2 transition in Mg^+. About 2.2 mW seed laser power get amplified to 135 mW by two pre-amplifier stages, before the power level is boosted to 2 W in the main amplifier.
The oscillator and all amplifiers are made of polarization-independent fibers. Linear polarization is defined in the seed laser, but it is scrambled in the consecutive fiber components. The output polarization is therefore in a random but pure polarization state. This polarization state is rotated to the desired linear polarization with a

combination of a half- and a quarter-wave plate. The polarization changes rapidly during a warm-up time of about 1.5 h, but is reproducible from day to day. The light is then sent to a free-space optical isolator to prevent back-reflections into the power amplifier. The measured transmission of the isolator was $T = 0.83$ at maximum extinction of the back-reflected beam.
During our spectroscopic measurements (Chapter 4) we operated the laser system as a 'black box' in its original case. After repeated failures and considerable down-times of this commercial fiber laser system, we decided to investigate the notorious problems by ourselves, together with Tobias Wilken and Menlo Systems as experienced partners. The fiber laser in its present shape was strongly modified. All electronics were removed from the original case, which now contains the fiber components and the pump diodes only. An external rack houses the temperature stabilization module for the oscillator as well as temperature and current controllers for the pump laser diodes of the seed oscillator and both pre-amplifiers[1]. Two high power laser diodes pump the main amplifier, they are not temperature stabilized and connected in series. The current is supplied by a conventional power supply and the specified laser power of 2 W was reached at a pump diode current of 3.13 A. We restrict the current to 2.8 A, which correspond to about 1.65 W optical output power, since we assume that operation below specifications helps to prevent further breakdowns. It is crucial to seed all amplifier stages before they are consecutively switched on, otherwise they may Q-switch and destroy components.

3.1.2. Second harmonic generation cavities I

Green light at an intermediate wavelength of 559 nm and the desired UV light at 280 nm is obtained from the fiber laser by resonantly enhanced second harmonic generation (SHG). Detailed descriptions of our home-built enhancement cavities can be found in [50, 58, 59]. The 1118 nm $\rightarrow$ 559 nm cavity incorporates a 15 mm long temperature phase-matched LBO crystal ($T = 91.4°C$). Temperature phase matching is free of walk-off and preserves a good beam profile at 559 nm. The green beam is matched to the second SHG stage with a single lens ($f = 100$ mm). The 559 nm $\rightarrow$ 280 nm cavity houses a 1 cm long angle phase-matched BBO crystal, which is kept at 50°C to prevent moisture absorption. Both crystals reside in the focal arm of bow-tie resonators, they are rectangular cut and anti-reflection coated for the respective wavelengths. Each cavity length is stabilized with a piezo-actuated mirror and the required error signals are obtained via the Hänsch-Couillaud method [60]. Typically we obtain about 400 mW of green light at 559 nm and, after astigmatism compensation with cylindrical lenses and spatial filtering with a 50 μm pinhole, 10 mW UV light at 280 nm.

[1] Thorlabs PRO8000 rack, TED8040 temperature controllers, LDC8010 current controllers, set points: 447 mA (seed), 650 mA (pre-ampI), 740 mA (pre-ampII)

During the down-times of the fiber laser system we fed about 350 mW of 559 nm light from our dye laser (Section 3.1.3) into this 559 nm → 280 nm SHG stage. We solely adjusted the coupling into the TEM_{00} mode of the cavity, such that the following beam path remained unchanged. A repositionable mirror enabled complementary use of both laser systems.

3.1.3. Dye laser systems

Single frequency ring dye lasers are rather complex and anachronistic, but still competitive light sources in the green-yellow to red wavelength regime, where simple solid-state laser systems are not yet available[2]. Here, barely hazardous, efficient and highly photo-stable Rhodamine dyes can be conveniently pumped by green diode pumped solid state lasers. The advantages of dye lasers are their flexibility and reliability. The wavelength can be arbitrarily set over several tens of nanometers and the laser system can serve in different experiments over decades. These advantages go along with great expenses in cost, laboratory space and maintenance.
We were running two Coherent 699 cw-dye laser systems. One was initially used for photo-ionization, but the mentioned problems with the fiber laser forced us to switch the output wavelength from 570 nm to 560 nm to address the 3s-3p transitions at 280 nm. As intermediate photo-ionization source we ran another Coherent 699 dye laser, meanwhile we changed to a pulsed dye laser for photo-ionization. The pulsed dye laser was not used for our spectroscopic experiments (Chapter 4) and we refer to Appendix A for a description.
The work horse for most of our published experiments was a Coherent 699 ring dye laser. A Coherent Verdi V10 Nd:YVO_4 laser provides up to 10 W pump power at 532 nm. The dye solution is circulated at 11 bar by a high pressure pump (Radiant Dyes RD1000). It passes an air cushion before a dye jet is shaped by a sapphire nozzle, which can handle higher pressures than the original steel nozzle. The ring laser is build in vertical configuration on an invar rod for passive stability. The resonator contains several frequency selective elements (three-stage birefringent filter, two etalons), an optical diode for uni-directional operation, quartz rhombs for astigmatism compensation and a quartz plate near Brewster's angle, which can be tilted to adjust the optical length of the resonator. A sample of the output beam is fed into a heated low-finesse reference cavity for active stabilization of the resonator length. Another tiltable quartz plate within the reference cavity is used to tune the laser frequency in loop. The optical length of the resonator is thereby adjusted by the quartz plate and the thinner etalon, while fast changes are compensated by

[2]Recent advances in solid state laser engineering like optically pumped semi-conductor lasers (e.g. Coherent) or Raman amplified fiber laser systems (e.g. MPB Communications), in combination with novel single pass wavelength conversion modules (e.g. NTT electronics) are in the process of filling this gap.

the 'tweeter', a small mirror glued to a piezoelectric actuator. The resulting laser linewidth is in the 1-3 MHz regime and the long-term stability is sufficient to continuously address the $\Gamma/2\pi = 41.8$ MHz cooling transitions in Mg^+ for alignment purposes. For measurements we stabilize the optical frequency with the schemes described in Section 3.1.6. Hereby we connect a low bandwidth error signal to the external input of the commercial control box, this signal adjusts the quartz plate in the reference cavity and the laser frequency follows in loop.
For a typical dye mixture we solve 0.5 g Rhodamine 19 in 125 ml benzyl alcohol, 875 ml ethylene glycol is added since the formation of a clean dye jet requires a viscous solution. This dye recipe worked fairly well when the laser was operated at 570 nm for photo-ionization. When we changed the operation wavelength to 560 nm we chemically shifted the gain profile to shorter wavelength by adding a basic solution of 8 g KOH in 40 ml methanol[3].
We demonstrated an output power of 1 W at 560 nm and 7.2 W pump power. With fresh dye solution we usually produce 300 mW at 4 W pump power. We try to keep this power level over a typical operation period of 2-3 month, during which we increase the pump power gradually to 6 W. Then we exchange the degraded dye[4], since the decrease in conversion efficiency causes a decrease in output stability. The output beam profile was measured with the knife-edge method [61]. A fit to the data yielded a beam waist of $w_0 = 461$ μm at a position 24.4 cm after (outside) the output facet of the dye laser. Mode-matching with the consecutive enhancement cavity was achieved by placing one $f = 500$ mm lens at a distance of 42.8 cm in front of the incoupling mirror of the enhancement cavity. It is likely that the beam characteristics have changed somewhat over time due to extensive realignments and exchange of cavity mirrors.
A sample of the dye laser output is reflected by an uncoated microscope slide and again divided by a 50/50 beam splitter. One arm is coupled into a single-mode fiber and guided to a Burleigh WA-1500 Michelson type wavemeter. The other arm is beated against the frequency-doubled output of a diode laser at 1118 nm (Figure 3.1). Single-frequency operation of the dye laser is monitored by the fringe pattern of the Michelson wavemeter or directly observed in the beat signal with the

[3]The recipe is widely adopted from Tobias Schätz and is optimized for Rhodamine 19 dye from the former Lambda Physics company, which is no longer available. At the moment the laser runs on Rhodamine 19 from Radiant Dyes and chemical shifting is not as effective any more. KOH pieces conveniently solve in methanol using an ultrasonic bath.

[4]Procedure: Make sure the laser is properly aligned before exchanging the dye. Reduce the pressure to about 4 bar and close the valve between the air cushion and the nozzle. Carefully insert e.g. nitrogen at about 5 bar into the air cushion (fill level 5-10 cm). The pump pressure is gradually reduced and the nitrogen atmosphere presses the dye back into the reservoir. Close the valve between the pump unit and the air cushion. Reduce the pump pressure to minimum pump speed and pump the dye out of the reservoir via the disposal valve. Make sure that the pump never runs 'on air' during the whole procedure, this will create bubbles, which can prevent stable operation of the dye laser for about one day.

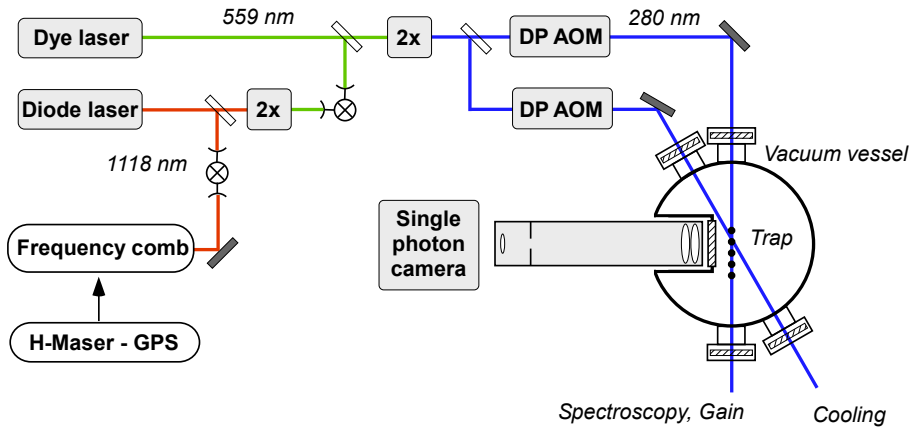

Figure 3.1.: Schematic setup. In this scheme we produce a cooling and a spectroscopy beam from a single laser source. Hereby we split the laser beam and tune the spectroscopy arm with a double-pass AOM setup (Section 3.1.5). The laser frequencies are phase-locked to a GPS disciplined hydrogen maser. The phase coherent link between the RF reference and the UV regime via a fiber laser frequency comb and a transfer diode laser is schematically shown. Color changes indicate frequency conversion. The spectroscopy laser is called gain laser in our ion oscillator experiments (Chapter 5). An alternative setup is shown in Figure 4.6, where cooling light resonant to the D_2 transition is provided by our frequency-quadrupled fiber laser, while the spectroscopy beam is produced by the dye laser. In this case we tune the dye laser frequency against the transfer diode laser by changing an offset frequency in loop.

diode laser and the transmission spectrum of an aligned SHG cavity.
Once the fiber laser had its first major malfunction we promoted our former photo-ionization laser to a cooling laser. However we had learned to appreciate the advantages of photo-ionization compared to electron impact ionization [62]. Therefore we decided to employ another Coherent 699 laser, which was initially set up by Guido Saathoff for an experiment with metastable Li^+ ions [63]. This laser was pumped with an optical power of about 8 W from a Coherent Innova-400 multi-line argon ion laser, which predominantly lases at 515 nm. The presence of shorter wavelength lines in the pump light led to faster degradation of the dye mixture. The yellow laser output at 570 nm was coupled into a single mode fiber and guided onto our optical table. Here it was fed into an enhancement cavity to produce light at 285 nm. This dye laser turned out to be considerable less stable in operation than the identically constructed Coherent 699 laser for cooling and spectroscopy. It required great efforts to make this system run on a day-to-day basis, even though the requirements for photo-ionization are substantially relaxed. In spite of this it served its task and created all ions for the measurements described in Chapter 4.

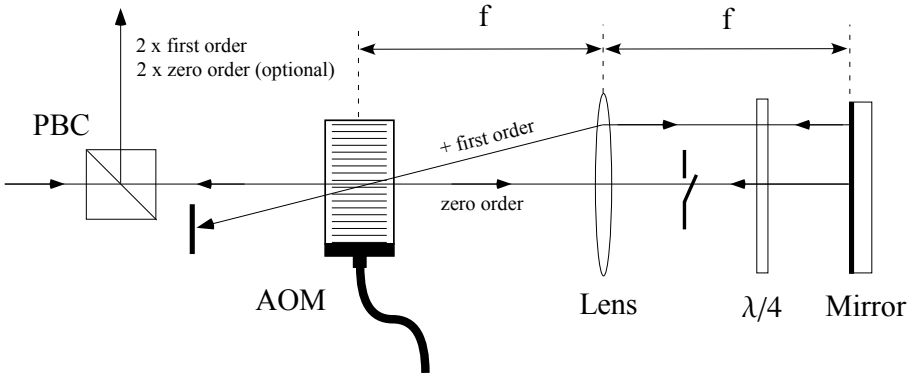

Figure 3.2.: Double pass AOM setup. The linearly polarized input beam passes a polarizing beam splitter cube (PBC). The Bragg grating in the AOM deflects the beam and the frequency of the first diffraction order is up-shifted by the drive frequency of the AOM. A single lens and a mirror in an effective 4f-configuration ensure counter-propagating beams, independent of the deflection angle and therefore independent of the drive frequency of the AOM. Two passes through a quarter-wave-plate ($\lambda/4$) rotate the linear polarization by 90°. The AOM is passed in reversed direction and the first order diffraction now counter-propagates to the incoming beam. Finally it is reflected by the PBC. The unshifted zero-order beam is blocked during our measurements, but utilized for trap loading as an additional, further red-detuned laser beam.

3.1.4. Second harmonic generation cavities II

We built two additional resonant SHG cavities for the dye laser systems. The first one for frequency doubling of our initial photo-ionization dye laser at 570 nm. The second one for frequency doubling at 560 nm for experiments with two different laser sources at 280 nm. Here we use Brewster-cut BBO crystals in both cavities. The performance of the second 560 nm $\rightarrow$ 280 nm cavity corresponds to the respective cavity of the fiber laser system (Section 3.1.2). Frequency doubling from 570 nm to 285 nm was slightly less effective, since we used mirrors and crystals designed for 560 nm. With the initial photo-ionization dye laser we obtained up to 10 mW at 285 nm from 300 mW fundamental light, after spatial filtering we were left with about 2 mW on a day-to-day basis. With the Argon ion laser pumped dye laser we ran a daily optimization procedure until we obtained about 1 mW at 285 nm. Here we omitted spatial filtering since power was more valuable than a good beam profile for photo-ionization.

3.1.5. Frequency shifters

The experiments described in Chapters 4 and 5 require two UV laser beams at separately controllable, slightly different frequencies. A cooling laser needs to stay at

a fixed frequency below the investigated transition, while a spectroscopy laser is to be tuned across the atomic resonance with a frequency range of 180 MHz ($>4\Gamma/2\pi$, Section 4.2). Both beams can be produced from a single UV laser. We split the beam with a 50/50 beam splitter and send each sample to an acousto-optic frequency shifter (Brimrose QZF-150-100, center frequency 150 MHz) in double-pass configuration (Figure 3.2)[64]. Each output beam is frequency-(up)shifted by twice the drive frequency and it counter-propagates with respect to the incoming beam. It is convenient to split both beams with a polarization scheme (Figure 3.2), even though UV AOMs made from quartz glass show an unfavorable polarization dependence of the diffraction efficiency for the retro-reflected beam.
For intensity stabilization we take samples of both beams behind the acousto optic modulator (AOM) setups and direct the beams onto UV photo diodes. The output voltage is compared to a chosen set point and a PI controller adjusts laser intensities via the drive powers of the AOMs.
One feature of the double-pass arrangement is the geometrical overlap of the unshifted zero order, with the frequency-shifted first order diffraction (Figure 3.2). We utilize this during trap loading. The zero-order beam acts as an additional laser beam, which is red-detuned by about 300 MHz with respect to the first diffraction order. The benefit for the loading process is twofold: the additional laser field enhances the ionization probability for the resonant photo-ionization process (significant only for cw-laser ionization) and the further red-detuned laser enables faster Doppler cooling of motionally hot Mg^+ ions to mK temperatures. Fast fluorescence detection is advantageous for loading a wanted number of single ions.

3.1.6. Laser stabilization and absolute frequency calibration

For frequency stabilization we take advantage of a convenient feature of our particular laboratory environment, namely the availability of accurate optical and radio frequency reference signals 'out of the socket' [65]. The RF reference for all involved frequency combs, phase-locked loops, counters and the spectroscopy AOM is provided by a hydrogen maser. A comparison between the free-running maser and the global positioning system showed a deviation smaller than 1.7×10^{-13} over the whole period of our spectroscopic measurements, which is more than sufficient for our purpose (Section 4.4). Optical reference signals from two different erbium fiber laser frequency combs were available via optical fiber: A frequency comb with 100 MHz repetition rate (20 MHz CE offset frequency) located in our groups 'clock room' and a frequency comb with 250 MHz repetition rate (37 MHz CE offset frequency) located in the neighboring 'hydrogen laboratory'. In both cases we used a sample of the super-continuum, which is initially generated for the comb's f-2f interferometers and reached well into the fourth sub-harmonic of the Mg^+ doublet at about 1118 nm. We recorded a free-space beat note between the optical monitor port of the cw-fiber laser and a neighboring frequency comb mode at 1118 nm. The

signal-to-noise ratio of this beat note (> 30 dB in 400 kHz bandwidth) was sufficient for our phase detectors [66] and redundant counters (HP53131A). A fortunate value of the $^{24}Mg^{+}$ D_2 transition frequency enabled a convenient offset lock 40 MHz next to a mode of the 100 MHz frequency comb. Adjusting the frequency of the stabilized fiber laser was possible with the double-pass AOM scheme described in the preceding Section 3.1.5.

The failure of our fiber laser system required absolute frequency calibration of the green dye laser output at 560 nm. Here we employed an additional transfer diode laser at 1118 nm, which was stabilized to a frequency comb mode. The output of the diode laser is frequency-doubled in a 18 mm long, anti-reflection coated LBO crystal in single-pass configuration. We use the second harmonic of the diode laser to record a beat note with a sample of the dye laser output (Figure 3.1). We mix the beat frequency with a synthesizer and obtain a fixed offset lock frequency of 80 MHz. Changing the synthesizer frequency in closed loop sets the dye laser to arbitrary frequencies with respect to the comb modes. This technique was also used to tune the spectroscopy laser, when we cooled the ion chain with the independent fiber laser system (Figure 4.6).

A disadvantage of direct locking to a frequency comb mode is frequency jitter. The comb modes jitter on time scales of milliseconds with an excursion of about 1 MHz at 1118 nm, which corresponds to 4 MHz in the UV. A servo loop with large bandwidth will imprint this jitter on the spectroscopy laser. The dye laser is locked with very low bandwidth and hardly follows the millisecond jitter of the comb. We observed in-loop frequency excursion in the beat signal between the frequency-doubled diode laser and the dye laser (Figure 3.1) with our eyes, from that we estimate a servo bandwidth of about 10 Hz. The frequency excursions showed an amplitude of about 1 MHz at 560 nm, while the short-term stability was given by the reference cavity of the dye laser. From a beat measurement against the frequency-doubled cavity-stabilized diode laser (see Chapter 2.2.3. in [56]) we infer a linewidth in the 1-3 MHz range at 560 nm. A conservative upper estimate on the UV linewidth is 6 MHz, centered around a stabilized absolute frequency. This rather broad linewidth of our spectroscopy laser limited the accuracy of our spectroscopic measurement (Section 4.4).

The linewidth of the fiber laser is specified to be smaller than 70 kHz, but we observed frequency drifts up to 1 MHz/s. For magnesium spectroscopy (Section 4.3) and our first ion oscillator experiments (Section 5.2) we stabilized the laser frequency directly to a comb mode of the 100 MHz fiber laser frequency comb. The piezoelectric actuator as fastest feedback element in the fiber laser oscillator showed a modulation bandwidth of about 200 Hz. The frequency jitter of the comb modes was still present in the in-loop beat note between the fiber laser and the frequency comb, which indicates that the fiber laser frequency did not entirely follow the comb's excursions. We did not have a good measure for the effective linewidth of the absolute frequency-stabilized fiber laser, a conservative upper bound is given by

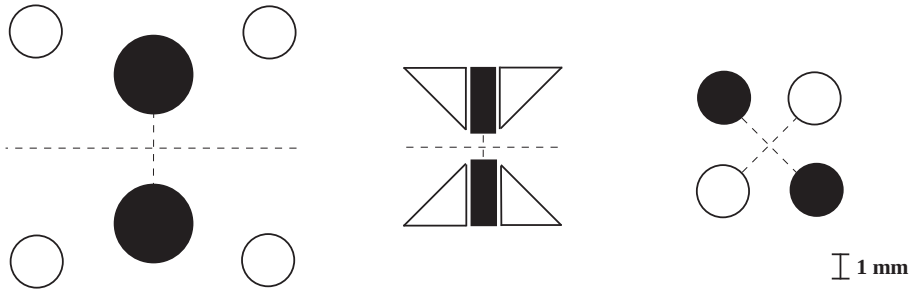

Figure 3.3.: Radial electrode structure of three different linear ion traps. The RF signal is applied to the black electrodes, white electrodes indicate RF ground, dashed lines represent the principal axes of the trap. From left to right. Six-rod trap (Section 3.2.1, Figure 3.4), linear endcap trap (Section 3.2.2, Figure 3.5), four-rod trap (Section 3.2.3, Figure 3.6).

1 MHz at 1118 nm. In the present setup we stabilize the fiber laser frequency to an external reference cavity via our transfer diode laser (see Chapter 2.2.3. in [56]). The in-loop beat-note between the stabilized diode laser and the fiber laser has a width of 60 kHz. This states an upper bound for the short term stability of the fiber laser which is free-running on time scales of ms. The maximum drift rate of the reference cavity was measured to be 15 Hz/s. Counting the beat note with a frequency comb mode enables automated drift correction on the time scale of seconds by adapting an offset lock frequency.

3.2. Ion trap apparatus

During the time period of this thesis we experimented with three different ion traps. We introduce all traps with a focus on design ideas. We point to limitations and experimental requirements, which led to revised trap designs, while we refer to the corresponding Chapters in [50, 56, 62] for technical details. Afterwards we give a short introduction to the vacuum vessel, which housed the 'linear endcap trap' and the 'four rod trap' and was employed for the experiments described in Chapters 4 and 5.

3.2.1. Six-rod trap

The ion trap project in our group was started from scratch and aims at a measurement of the 1s-2s transition in He^+ [53]. The 'six-rod trap' was brought along by Hans Schüssler and set the playground for our first steps in this field. First ions were created by electron impact, trapped and detected with a channeltron [62]. We detected fluorescence from the 285 nm transition in neutral Mg and trap loading via resonant photo-ionization was subsequently demonstrated. Then we observed first

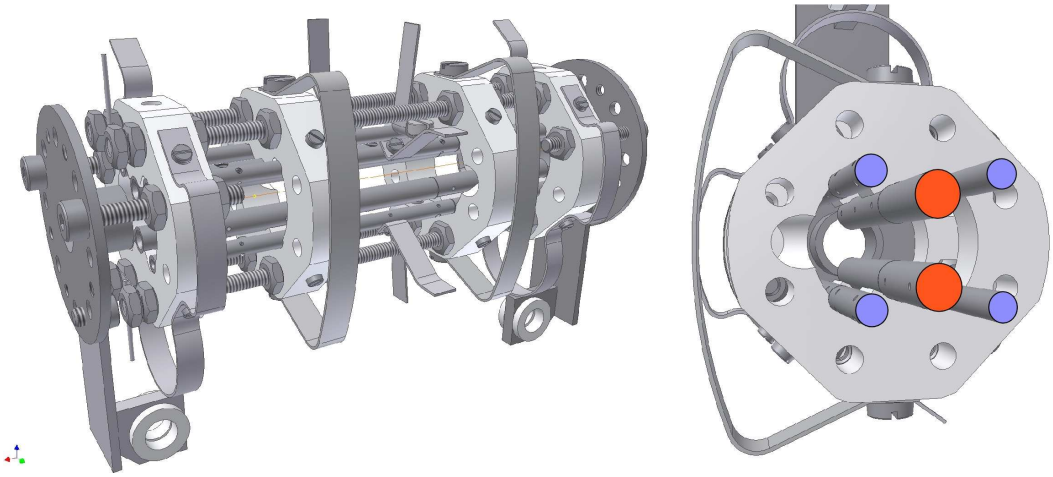

Figure 3.4.: Six-rod trap. The extensive use of insulating ceramics (Macor, light grey) makes the trap prone to stray potentials. RF and DC signals where applied to two center electrodes (red). Grounded electrodes (blue) step behind the center electrodes for enhanced optical access to the trap center.

fluorescence signals from trapped, laser-cooled Mg^+ ions and performed mass spectroscopy by optical secular excitation scans [62]. Later we tried to provide cold He^+ ions sympathetically cooled by Mg^+. Here we did not succeed to obtain conclusive He^+ signatures from secular excitation, which motivated the decision to build laser systems for lighter Be^+ ions (Section 6.1).
RF and DC signals were simultaneously applied to two rods 3 mm in diameter, at a separation of $2r_0 = 2.8$ mm to each other. RF and DC ground was set by four hidden rods behind the main electrodes, such that the optical access angle was increased to 70.9° (Figure 3.3). One particular feature was the large trapping volume. We counted as much as 10^6 trapped Mg^+ ions with a channeltron and fluorescence could be seen by the bare eye, when we imaged the UV light on a sheet of white paper. Huge ion samples and a compact size of the vacuum vessel [62] enabled fast progress in an early stage. However the six-rod trap also quickly revealed limitations due to its design. Extensive use of isolating spacers from Marcor ceramics (Figure 3.4) caused strong stray potentials after ion trap loading by electron impact, which is necessary to ionize neutral helium atoms. This resulted in transient DC potentials and considerable displacements of the ion sample from the initial trap center. We had to re-adjust compensation voltages after each trap loading. The two-rod geometry enabled a large optical access angle at the expense of a shallower trapping potential [62]. Yet the optical access was greater then the numerical aperture of our imaging optics. Four-electrode structures with adapted electrode geometries offer a better trade-off between optical access and trap stiffness.

Figure 3.5.: One half of our linear endcap trap, we refer to Figure 3.3 for the electrode structure in radial direction. RF and DC signals are applied to different segments, while grounded endcap electrodes extend over the full length of the trap. For our spectroscopy (Chapter 4) and ion oscillator experiments (Chapter 5) we used a single long segment of the trap.

3.2.2. Linear endcap trap

The linear endcap trap[5] served for the experiments described in [15, 16, 24] (Sections 4.3 and 5.2). The trap was designed by Maximilian Herrmann, a thorough description can be found in Chapter 2.1.5 in [50]. RF and DC signals were simultaneously applied to two opposing rectangular electrodes facing each other, the distance between the electrodes was $2r_0 = 1$ mm. Four wedged 'endcap' electrodes, set to RF and DC ground, enclosed the center electrodes (Figure 3.3). The trap design aimed at a high optical access angle and experiments with single or few trapped ions. The segmentation of the trap (Figure 3.5) reflected the proposed experimental scheme for 1s-2s spectroscopy in He^+ [53].
Two drawbacks common to the linear endcap trap and the six-rod trap design were coupling of RF and DC signals to the same electrodes and the orientation of the principal trap axes (Figure 3.3). The former required additional low pass filters for DC coupling, which limited the resonance frequency of the RF circuit. The latter resulted, in combination with the optical access to our vacuum vessel, in limited projections of 15° and 4° on the radial trap axes. This corresponds to theoretical Doppler limits of 0.7 mK in axial, 3.5 mK in horizontal and 41.6 mK in vertical radial direction [15]. The Doppler temperature in radial direction did not limit our

[5]The name is adopted due to close analogies to the so-called 'linear endcap trap' design of Volker H. Ludsteck [67] in the former group of Herbert Walther.

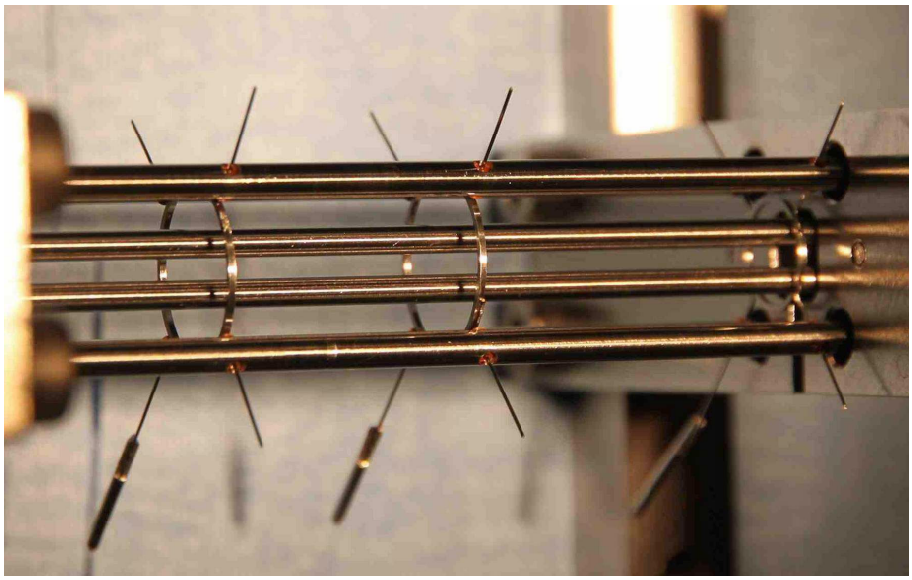

Figure 3.6.: Four-rod trap, side view. Only two of the four center electrodes are visible, we refer to Figure 3.3 for the radial electrode structure. We apply DC voltages to ring electrodes surrounding the center rods for axial confinement. Low residual axial RF enclosure is obtained by an elongated, solid electrode structure. Insulating surfaces in line of sight to the trap center are carefully avoided. The small ring electrode at the right edge of the trap is the signal electrode for the injection-locking experiments described in Section 5.3.

axial chain spectroscopy and ion oscillator experiments.
It also turned out that the aspect ratio between the electrode distance (1 mm) and the spacing between the individual segments (0.5 mm) was sufficiently large to create a local minimum in the RF potential, such that ions could be trapped in between segments. During our spectroscopy and ion oscillator experiments we used only one 5 mm long segment at a time, all other segments and DC offsets were disconnected [50]. This increased the resonance frequency, while axial enclosure was established by the residual RF potential.

3.2.3. Four-rod trap

Our four-rod trap was designed by Sebastian Knünz and we refer to Section 2.1.2. in [56] for a detailed description. The trap consists of four symmetrically arranged tungsten rods, 80 mm in length and 2 mm in diameter (Figure 3.3). It approximates the classical linear quadrupole trap design, while electrodes differ from the ideal equipotential shape to offer good access for laser beams and imaging optics. DC enclosure is established by ring-shaped electrodes surrounding the rods (Figure 3.6). The design was optimized for different purposes. One was low residual axial RF

enclosure. In order to minimize axial RF potentials we use long, solid rods as radial RF electrodes and surrounding rings as axial DC electrodes. This was beneficial for our experiments with the ion oscillator (Chapter 5) and enabled a direct observation of the thermal distribution of a Doppler-cooled ion in a shallow potential (Figure 2.4). Second we carefully avoided insulators in line-of-sight with the trap center, in order to reduce the influence of unwanted patch potential in case of electron gun loading. The latter was triggered by the problems with electron gun loading of He^+ ions in the six-rod trap and dedicated for future experiments with ion species like (Be^+), $^*Li^+$, He^+ where resonant photo-ionization sources are not readily available (in our laboratory). We also chose a big trapping volume ($2r_0 = 2.95$ mm), aiming at experiments with large ion crystals as proposed in Section 6.3.
The limitations and disadvantages of this trap are downsides of our design goals. Low axial RF enclosure excludes dense segmentation, the trap is not designed for ion shuttling schemes as proposed in [53]. The large trapping volume is not ideal for experiments with single ions or small ion chains. One-by-one loading of a defined ion number is harder than with the linear endcap trap, since ions evade the cooling laser on extended orbits and sometimes appear with a delay of seconds. A large trap radius also restricts the range of accessible radial secular frequencies, since it requires high RF voltages (Equation 2.4). The axial oscillation frequency is also limited due to a different effect. The electric field of the ring electrodes is effectively screened by the trap electrodes and an upper limit on the axial secular frequency is $\omega_{ax}/2\pi \approx$ 120 kHz. The corresponding DC voltage of 2 kV approaches the breakdown voltage of several components ($\omega_{ax} \propto \sqrt{U_{ax}}$, Equation 2.8).

3.2.4. Resonant RF circuits

The stability conditions introduced in Section 2.1.1 are also fulfilled for slow radio frequency signals and low voltage amplitudes, yet such a trap would show a shallow trap potential (compare Equation 2.7). The trap depth for a $^{24}Mg^+$ in an ideal quadrupole trap ($r_0 = 1.475$ mm) at $\Omega/2\pi = 1$ MHz and $U_{\mathrm{rf}} = 1.5$ V ($q = 0.14$) is only 200 K. We operated our trap at about $\Omega/2\pi = 22$ MHz, which requires several hundreds of Volts amplitude ($U_{\mathrm{rf}} = 725$ V at $q = 0.14$), but offers a trap depth above 100 000 K in this example. Such RF signals are not readily available from conventional signal sources and amplifiers, due to the high RF power consumption and impedance mismatch with the trap capacitance. Resonant RF circuits are widely used for voltage enhancement and impedance matching. Thorough design guidelines for so-called tank circuits can be found in the thesis of Maximilian Herrmann [50].
Our LCR circuit consist of the trap itself in series with the vacuum feed through as capacitance, Ohmic losses and a coil with inductance $L = 3.4$ μH. As signal source

we use an analog synthesizer[6]. The amplified signal (Mini Circuits ZHL 5W-1) passes a directional coupler, which monitors the coupling via an adjustable current loop surrounding the coil of the tank circuit. Typical resonance frequencies were about $\Omega/2\pi = 15.8$ MHz for a single segment of the the linear endcap trap and $\Omega/2\pi = 22.6$ MHz for the four-rod trap. Typical radial secular frequencies were about $\omega_s/2\pi = 1$ MHz for the linear endcap trap and $\omega_s/2\pi = 1.4$ MHz for the four-rod trap. The residual axial RF potentials correspond to an axial secular frequencies of about $\omega_{ax}/2\pi = 70$ kHz in the endcap trap and below $\omega_{ax}/2\pi = 1$ kHz in the four-rod trap.

3.2.5. Vacuum system

Stable trapping of atomic ions requires an ultra-high-vacuum (UHV) environment, which reduces the probability for collisions with background gas particles. In the experiments described in [62] and Chapter 5 in [50] we trapped ions in a helium buffer gas atmosphere. Here we found that we could maintain a thermal cloud of laser-cooled Mg^+ ions up to a He pressure level of about 10^{-6} mbar for our specific experimental conditions. In absence of He buffer gas we easily reached pressure levels below 10^{-9} mbar, where collisional effects with background gas particles become negligible on time scales of seconds and we observed Coulomb crystallization of laser-cooled ion samples.
To obtain the precision of our spectroscopic experiment (Section 4.3) we require stable conditions for several tens of minutes. Two pressure-related perturbing effects were observed. First, collisions with background gas particles, which removed an ion from its site within the crystallized structure. We believe this was mostly due to elastic collisions, because Mg^+ ions frequently stayed trapped on high energy orbits, got re-cooled and re-arranged into the crystalline structure within a time scale of seconds. Second, chemical reactions with the background gas, more specifically the chemical formation of MgH^+ ions [68]. We observed a fluorescing Mg^+ ion turning dark spontaneously, the dark ion stayed initially within the crystalline structure. The dark ion then changed its position within an ion chain on time scales of several seconds[7]. It was possible to remove MgH^+ from an ion chain when we applied a RF signal resonant to its radial secular frequency (Section 3.3.3). UHV conditions at pressure levels below 10^{-10} mbar and low hydrogen content in the background gas are preferred for our measurements.
Our vacuum vessel including all pumps and the bake-out procedure was described in Chapter 2.3.2. in [50], meanwhile we additionally apply a degassing current of

[6] Marconi 2020A. We have learned that digital synthesizers limited a quantum information experiment at the University of Innsbruck (Rainer Blatt, private communication). We are probably not sensitive to this subtle effect, yet we use an analog synthesizer for this reason.

[7] Reference [69] showed that the hopping rate within an ion chain depends on the axial potential, random configurations may be 'freezed' for several seconds by increasing the axial DC enclosure.

32.8 A to the filaments of the titanium sublimation pump throughout the bake-out period. We used different forevacuum pumps to achieve a crude vacuum of about 10^{-2} mbar or better. The forepumps are followed by a turbo pump. After the baking procedure we disconnect the mechanical pumps from the vacuum chamber with an all-metal angle valve. This excludes unwanted vibrations and prevents ventilation in case of a power blackout. The turbo pump would also act as a low pass filter for light species like hydrogen. The sealed chamber is internally pumped by a combined titanium sublimation and ion pump (Varian VacIon Plus 300), the titanium sublimation pump is particularly important since it pumps hydrogen more efficiently than the ion pump. In good operation condition we achieve a pressure below 10^{-11} mBar, which is below the measurement range of our cold-cathode gauge. Here we note that the gauge is based on electron impact ionization of background gas particles and has a reduced sensitivity to hydrogen. Hydrogen molecules cause the formation of dark MgH^+ ions and the titanium sublimation pump may be flashed once the creation rate of MgH^+ is suspected to have increased.

3.3. Ion creation

Atomic ions in RF traps can be stored at room-temperature (Section 2.1). It is convenient to initially trap the ions and apply subsequent Doppler cooling, which is then possible with a single laser beam at fixed detuning (Section 2.2.3). The ion trap resides in ultra high vacuum and the trap potential is essentially conservative. This suggests loading schemes in which ions are created from neutral particles within the trapping volume. Two popular ionization techniques are electron bombardment and resonantly enhanced photo-ionization. We usually vaporize neutral magnesium atoms from an oven and create Mg^+ ions by photo-ionization. Electron guns are also implemented into our setup. Here we refer to [50, 62] since electron impact ionization was not used for the experiments described in Chapters 4 and 5.

3.3.1. Atom oven

Technical details about the atom oven are described Chapter 2.6.1. in [50]. A piece of Mg wire is put into a tantalum tube with 1 mm diameter, which is heated by a tantalum wire. For the particular atomic oven, which is currently in use, we apply an electric power of 0.8 W. Mg atoms evaporate and drift out of the tube. A shielding cap with a 0.1 mm aperture in the center is placed about 7 mm away from the tube. This reduces the divergence of the beam and prevents excessive coating of trap electrodes. The trajectory of atoms in UHV are well approximated by straight lines. A small aperture will image the tube facet another 7 mm behind the shielding cap, from that we estimate a divergence angle of about 8°. A fraction of the atomic beam will hit and coat the electrodes, which introduces unwanted contact potentials

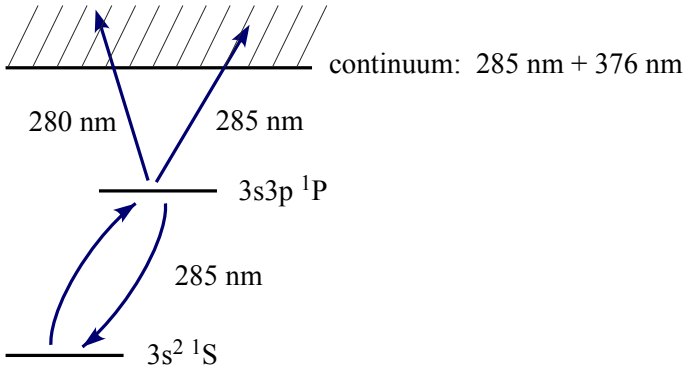

Figure 3.7.: Simplified level scheme for resonant photo-ionization of Mg atoms. A laser beam at 285 nm is resonant to the 3s^2 ^{1}S - 3s3p ^{1}P dipole-allowed cycling transition. Ionization into the continuum is possible with additional photons from the photo-ionization laser or from the cooling laser at 280 nm. The dipole-allowed cycling transition is saturated with moderate laser power, while the ionization step has a more than six orders of magnitude smaller cross section.

between the Mg layer and the electrode material. The atomic ovens therefore point at a certain segment of our linear traps, the 'loading' segment. Alternately we used to load single ions directly in the experimental segment, albeit the atomic beam pointed at a different part of the trap (compare Section 3.2.2). To load single ions or short ion chains we reduce the oven current until fluorescing ions appear one by one. We block the photo-ionization laser once the desired number of ions is observed.

3.3.2. Photo-ionization

A clean and species-selective method for ion creation is resonant photo-ionization. The longest-wavelengths dipole-allowed transition in neutral magnesium is the 3s^2 ^{1}S - 3s3p ^{1}P transition at 285 nm, the absolute frequency of the resonant transition was measured with an uncertainty of 5 MHz [70]. A second photon from the photo-ionization laser at 285 nm or a photon from the cooling laser at 280 nm may ionize the atom (Figure 3.7).
An investigation of the time constants and cross sections provides insight into the photo-ionization process from order-of-magnitude considerations. The absorption cross section for a dipole-allowed transition is $3\lambda^2/2\pi = 3.9\times10^{-14}\mathrm{m}^2$ at 285 nm, while the cross section for the ionization step is more than six orders of magnitude smaller. It was measured to be $\sigma_{ion} = 8.1(2.3)\times10^{-21}\mathrm{m}^2$ in a 285 nm magneto-optical trap for Mg atoms [71]. The saturation intensity $I_{sat} = 4400$ W/m^2 of the dipole-allowed transition is obtained with a moderate laser power of 0.55 mW, loosely focused to a beam diameter of 0.4 mm.
The mean velocity of a ^{24}Mg atom at 400°C oven temperature is about 770 m/s,

such an atom crosses a 0.4 mm diameter laser beam in a mean flight-time of 520 ns. This transit time is long against Rabi frequency cycles associated with the saturated dipole-allowed transition ($\tau \approx 2$ ns). Therefore we may treat the saturated atomic beam as a sample of constant particle number and approximate the upper state occupation by a factor one half[8]. The ionization rate for a single, saturated atom reads

$$r_{ion} \approx \sigma_{ion} \frac{\lambda I}{2hc}, \tag{3.1}$$

where we consider the photon flux density at intensity I and wavelength λ (h: Planck's constant, c: speed of light). At the saturation intensity of the resonant level we obtain a single particle ionization rate of only 25 Hz. An increase of this ionization rate to the inverse of the transit time would require a UV laser power of 42 W at a beam diameter of 0.4 mm.
To summarize, the resonant step may be saturated by a moderate amount of laser power. The two-step photo-ionization may then be viewed as a one-photon process with constant lower state population. The ionization cross section is much smaller and additional photons e.g. from a cooling laser at 280 nm can be fully employed to enhance the ionization rate. Viewed as an unsaturated one-photon transition the ionization rate is maximized by loose focusing, since the number of addressed atoms increases with w_0^3 while the intensity dependence scales $1/w_0^2$. This argument holds for photo-ionization of a magnesium background atmosphere. The optimum beam waist for trap loading will also depend on geometric overlap with the trapping volume and the atomic beam.

3.3.3. Isotope-selective trap loading

Alkali-like ions are commonly loaded via resonant photo-ionization from a thermal beam of neutral atoms. Isotope selective photo-ionization was demonstrated by a number of groups [72, 73, 74, 75, 76] using narrow linewidth laser beams perpendicular to carefully collimated atomic beams. Magnesium has three stable isotopes (natural abundance: ^{24}Mg 79%, ^{25}Mg 10%, ^{26}Mg 11%). The moderate atomic mass of magnesium results in relatively large isotope shifts of the 285 nm transition. The $^{25-24}$Mg and $^{26-24}$Mg isotope shifts[9] were determined to be 743.8(3.0) MHz and 1415.3(5.0) MHz respectively [77]. This compares to the natural linewidth of

[8] Depletion of a certain velocity class by a narrow bandwidth laser is a minor effect here. The maximum scattering rate is given by $\Gamma/2$, each recoil event will cause a velocity change of a ^{24}Mg atom which corresponds to a Doppler shift of 205 kHz. About 430 scattering events are necessary to obtain a $\Gamma/2\pi$-frequency shift, about 120 photons are scattered within the transit time of 500 ns.

[9] The $3s^2\ ^1S$ ground state of magnesium atoms shows no hyperfine-structure (J = 0). This excludes pumping into dark hyperfine states by a narrow-linewidth laser, which would considerably suppress the $^{25}Mg^+$ loading rate.

$\Gamma/2\pi = 78$ MHz and a Doppler broadening of about 4 GHz at 400°C oven temperature. The isotopic substructure is therefore unresolved unless the Doppler broadening is geometrically reduced by a well defined angle between the atomic beam and the laser beam. The specific geometry of our setup offered only limited isotope selectivity during our spectroscopic measurements (Chapter 4). We detuned the photo-ionization laser to the low frequency side of the unresolved resonance and loaded isotopically pure chains of 10-20 ions of the abundant ^{24}Mg component by chance. This approach is statistically almost excluded for ^{26}Mg. Yet we were able to load purified $^{26}Mg^+$ ion chains, when we swept an additional radio frequency signal over the $^{24}Mg^+$ and $^{25}Mg^+$ radial secular frequencies during the loading period. Such a RF signal (10 Vpp) was applied to an endcap electrode parallel to the trap axis of the linear endcap trap (Figure 3.3). This loading scheme enabled our spectroscopic measurements on the $^{26}Mg^+$ component without changing the vacuum part of the setup. It also greatly relaxes the spectral requirements of a photo-ionization laser source. We reproduced this isotope-selective loading method with a spectrally broad pulsed photo-ionization laser (Appendix A) in the geometrically different four-rod trap (Section 3.2.3), from which we infer the generality of the approach. We demonstrated purified ion chains of more than 30 low-abundant $^{26}Mg^+$ ions. Via radial secular excitation it was also possible to remove dark ions of different mass from a crystallized chain. In this procedure we exploit that resonantly driven radial motion decouples from axial motion, so we can selectively drive particles of different charge-to-mass ratio.

3.4. Imaging system

3.4.1. Imaging optics

We collect fluorescence photons with a four-lens condenser of 72 mm focal length. The first lens of the condenser has an aperture of 50 mm in diameter and is placed in a working distance of 75 mm to the trap center. Hereby we obtain a magnification of about 5. An aperture in front of the condenser can improve imaging at the expense of photon collection solid angle. Another aperture at the intermediate focal plane suppresses stray light. We use a microscope objective with 11.5 mm focal length and 6.8 mm working distance (Newport U-13X) to obtain an overall magnification of about 90, which is necessary due to the relatively large 'pixel size' of the multichannel plate based single-photon camera (Section 3.4.2). We refer to Section 2.3.4. and Figure 2.19 in [50] for further details and a technical drawing of the optics assembly.
The resolution and the magnification of our optics is most accurately calibrated with single-ion images. The physical distance of two ions at a certain secular frequency is obtained from Equation 2.9, from which we deduce a pixel-to-distance conversion

factor of 0.526 μm/px. The point-spread function at a given aperture in front of the first lens array can be determined from the thermal distribution of a single laser-cooled ion in a harmonic potential (Equation 2.22). We imaged a single ion and varied the equilibrium temperature (laser detuning) and the axial potential depth, least square fits to the thermal distributions revealed point-spreads of 1.7(1) μm and 1.87(5) μm, respectively (Chapter 3.2. in [56]). The differences in the point-spreads can be attributed to slightly different settings of the aperture.

3.4.2. Single-photon camera

We detect UV photons with a single-photon imaging detector, which may be viewed as a spatially resolving photo-multiplier (Quantar Technology Model 2601B Mepsicron II). Single photons release photo-electrons from a photo-cathode in front of a micro-channel plate. The secondary electron burst is read out resistively and the position gets encoded in X-Y voltage signals (0.5 - 4.5 V each). The detector is 23 mm in diameter and the resolution is specified to be typically better than 55 μm. Two key features of the camera are a good single-photon timing resolution of 100 ps and a dark count rate of less than 100 Hz over the whole detector area at room temperature. These properties enabled essentially background-free images as raw data for our spectroscopic measurements (Section 4.3) and a time-resolved investigation of the ion oscillator spectrum (Section 5.4). A particular difference between our single-photon camera and a photomultiplier is, apart from the spatial resolution, the dead time characteristics, since the position encoding electronics introduce additional rejection criteria for photon counts. This leads to an involved mixture of paralyzable, non-paralyzable and even position-dependent dead times (see Section 4.10). The maximum overall count rate is limited to about 60 kHz and dead time related non-linearities are pronounced above a count rate of about 10 kHz. We investigated the impact of the camera dead times on Voigt fits to artificial data sets. The nonlinear reduction in count rate has no appreciable effect on the center frequency of our absolute frequency measurements (Section 4.3), yet we observed a severe systematic effect on the Gaussian and Lorentzian contribution to the Voigt profiles (Section 4.10).
The detection efficiency of the whole imaging system was estimated to be 6.2×10^{-3} (Section 2.4.3 in [50]).

3.4.3. Camera readout

Each photon count from our camera is forwarded by a trigger signal with good timing resolution and X-Y voltages for position encoding. The signals are sent to an oscilloscope in X-Y mode for real-time observation and alignment purposes. The digital data acquisition and our measurement software were written and designed by Sebastian Knünz [56]. We digitize the X-Y position voltages in 512 $\times$ 512 pixel

images, which are displayed and stored after a chosen integration time. Each pixel represents a spatially resolved count rate and the images are the raw data for most of our measurements. The integration time is synchronized with our experimental hardware, which enables a fully automated measurement run. The count rate from a predefined spatial origin (region of interest) is directly forwarded for preliminary evaluation, which is a valuable diagnostic tool during our measurements.
Time-resolved photon counting is required for spectral and phase-sensitive diagnostics of our ion oscillator [56]. For stroboscopic imaging (Figure 5.5) we accept a trigger signal only in coincidence with a periodic gate interval, before we proceed with the image acquisition. To obtain the motional spectrum (Figure 5.4) of the ion oscillator we set discriminator levels for the position encoding X-Y voltages, hereby we preselect a spatial origin. Timing signals are only forwarded to a FFT device in coincidence with the chosen spatial origin, in this case the turning point of the ion oscillation.

4. Spectroscopy of the 3s-3p fine-structure doublet in Mg^+

In this chapter we present the main topic of this thesis: a precise measurement of the astrophysically relevant 3s-3p fine-structure doublet in Mg^+. Our work is motivated by a demand for more accurate laboratory reference data for astrophysical investigations, in particular for comparison with quasar absorption spectra, which indicate a space-time variation of the fine-structure constant. After an introduction to our method for precision spectroscopy of strong transitions in trapped ions [15] we discuss our measurement. Then we deduce $^{25}Mg^+$ transition frequencies and compare our results to related literature. Finally we present progress towards a precision lifetime measurement from the Lorentzian contribution to the linewidth.

4.1. Astrophysical motivation

Magnesium is among the most abundant elements in the interstellar medium [78]. Singly ionized magnesium is the dominant form there, since the ionization potential of Mg^+ is above the Lyman-α limit of the interstellar radiation field, which is not the case for neutral magnesium [79]. The strongest lines in Mg^+ are the 3s-3p transitions near 280 nm, which are therefore a prominent feature in many astrophysical spectra [80].

Space-time variation of the fine-structure constant

The main astrophysical motivation is a precise laboratory re-calibration of the Mg^+ 3s-3p transition frequencies for comparison with quasar absorption spectra [11], which have suggested a space-time variation of the fine-structure constant

$$\alpha = \frac{1}{4\pi\epsilon_0}\frac{e^2}{\hbar c}. \tag{4.1}$$

The fine-structure constant is the coupling constant of the electromagnetic interaction and is therefore of fundamental importance. The invariance of fundamental constants is an assumption which is especially important on cosmic space-time scales. This hypothesis is linked to Einstein's equivalence principle and needs to be experimentally validated [82]. Any variation in the fundamental constants requires

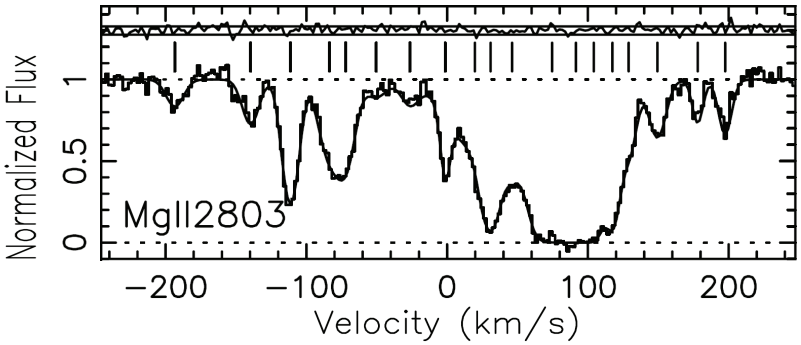

Figure 4.1.: Mg^+ D_1 absorption spectra observed towards the quasar Q1213-003 at $z = 1.554$. Tick-marks above the individual Mg^+ D_1 absorption lines indicate different velocity components in the absorber. The dashed lines indicate the continuum level of the illuminating quasar and zero photon flux. The frequency axis is given in terms of a velocity, 100 km/s correspond to 357 GHz at 280 nm. The remarkable precision of many-multiplet studies is gained by comparison with different absorption spectra (mainly Fe^+) from the same absorber and statistical evaluation of many quasar absorption systems. Taken from Figure 1 in [81].

a refinement of commonly accepted physical laws and would be of greatest interest as a test of novel theories [83]. The fine-structure constant governs in particular the atomic structure, in turn spectroscopic investigations of atoms allow to conclude on α. Todays most accurate studies of α in distant regions of our universe come from quasar absorption spectra. Quasars are among the most luminous objects of our universe and many of them are observed at high redshifts z. The line of sight between a telescope and a quasar is now intersected by interstellar gas clouds. Atoms in these gas clouds leave an absorption signal[1] as footprint in the continuous quasar spectrum (Figure 4.1).

The cosmological redshift z prevents a direct comparison of astrophysical spectra with laboratory measurements. Long look-back times are desired here, so most of the analyzed lines have rest frequencies deep in the UV regime, while they get observed through the optical transmission window of our earth's atmosphere. One has to identify at least two lines from the same cosmological object to disentangle the huge cosmological redshift from the faint contribution that may have had its origin in a different fine-structure constant. Furthermore the gross atomic structure shows the same α^2 scaling for all atoms, i.e. a change in α results in a common factor to all transition frequencies and would mimic a small additional redshift. An intuitive technique to circumvent this problem is the alkali-doublet method. It employs that the fine-structure splitting in alkali-like atomic systems is caused by spin-orbit

[1]The relatively quiet environment of the gas clouds results in narrow absorption signals and therefore in more accurate determinations of transition wavelengths than emission lines in high luminosity objects.

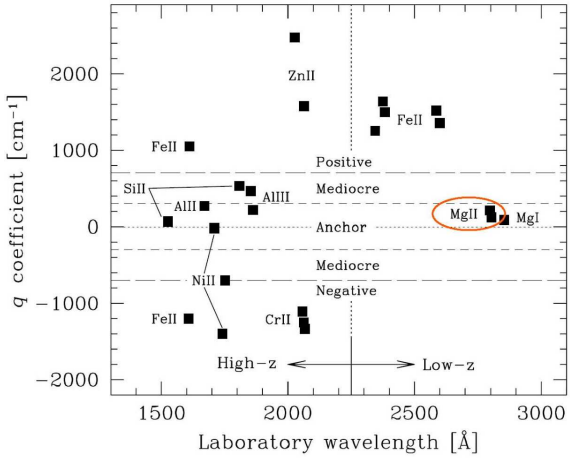

Figure 4.2.: Sensitivity coefficients q for low and high red-shift samples from Figure 1 in [90]. Mg and Fe lines dominate many-multiplet analyses at low red-shifts ($0.6 < z < 1.6$). The Mg^+ 3s-3p fine-structure doublet at 280 nm is highlighted (MgII is Mg^+). The sensitivity coefficients for Mg^+ are $q_{(D1)} = 120(10)$ cm^{-1} and $q_{(D2)} = 211(10)$ cm^{-1}, the alkali-doublet method is sensitive to this difference. Higher sensitivity is gained in many-multiplet analyses by a comparison of Fe^+ with Mg lines.

coupling and scales with α^4. Once both lines of an alkali-doublet are observed one may infer the redshift from the (weighted mean) wavelength $\langle\lambda\rangle_z$ and use the fine-structure splitting $\Delta\lambda$ as a probe for a variation in α [84]

$$\frac{\alpha_z}{\alpha} = \sqrt{\frac{\Delta\lambda_z}{\langle\lambda\rangle_z} / \frac{\Delta\lambda_{lab}}{\langle\lambda\rangle_{lab}}}. \tag{4.2}$$

This method was first suggested by Savedoff in 1956 [85] and applied to the Mg^+ 3s-3p fine-structure doublet by Wolfe and co-workers in 1976 [86]. More recent analyses of alkali doublets are compatible with zero drift of α at an uncertainty level of about 10^{-5} [87, 88, 89].

Webb and co-workers introduced the so-called many-multiplet method in 1999 [9, 10]. The many-multiplet method is a generalization of the alkali-doublet method where transitions in different atomic species from the same astrophysical object are probed. This is advantageous since more lines can be included, which improves the statistics and also reduces species-specific systematic effects [90]. Relativistic corrections (which scale with higher orders of α) are more pronounced for ground states rather than upper states involved in electronic transitions, a comparison of different species, and therefore different ground states, considerably enhances the sensitivity. One prominent example is the comparison between Mg^+ and Fe^+ lines. The relativistic corrections to the Fe^+ lines are larger than the corrections in Mg^+

thus a small variation in α will barely alter the Mg^+ transition frequencies, but influence the Fe^+ lines. The many-multiplet method requires numerical input for the sensitivity of all involved transitions frequencies to changes in α. Dzuba and co-workers express the rest-frequency ω_z (here given in wavenumbers) as

$$\omega_z = \omega_0 + q(\frac{\alpha_z^2}{\alpha^2} - 1), \tag{4.3}$$

where ω_0 is the laboratory reference frequency, q is the so-called sensitivity coefficient determined by many-body perturbation theory (Figure 4.2) and α_z is the hypothetical fine-structure constant in the astronomical object. α_z is varied in the analysis and a least square fit to all lines in a particular sample reveals its most likely value.
The many-multiplet method was first applied to Fe^+ transitions measured against the Mg^+ doublet and indicated that α was smaller than the present day value $\Delta\alpha/\alpha = (-1.9 \pm 0.5) \cdot 10^{-5}$ for redshifts[2] $z > 1$ [10]. The same group extended their studies to larger samples and further absorption lines [90, 91], which finally resulted in a statistically significant signature of a smaller fine-structure constant $\Delta\alpha/\alpha = (-0.57 \pm 0.11) \cdot 10^{-5}$. In this study 77 of 143 evaluated quasar absorption samples were low-z Mg/Fe absorbers [92]. All spectra were observed by the Keck observatory[3], attempts to reproduce the results with 23 Mg/Fe samples observed by the VLT[4] suggest a drift consistent with zero $\Delta\alpha/\alpha = (-0.06 \pm 0.06) \cdot 10^{-5}$ [93]. This work and further investigations consistent with zero drift are summarized and disputed in [94]. Recently Webb and co-workers published a new set of 153 quasar absorption measurements from the VLT and found that α appears to have been larger in the past [17]. A combination of the data from both telescopes covers the sky over the northern (Keck, Mauna Kea, Hawaii) and southern (VLT, Paranal, Chile) hemisphere and suggests a spatial variation of the fine-structure constant rather than a variation in look-back time. A dipolar spatial variation was reported with a statistical significance of 4 σ [17].

Requirements on laboratory reference data

Comparison with quasar absorption spectra requires laboratory reference data with an accuracy of better than 10^{-4}Å [11], which corresponds to about 40 MHz at 280 nm. This accuracy was fairly met by the 60 MHz uncertainty level of previous literature values (Section 4.7). Absolute frequency calibrated measurements in the favorable environment of an ion trap can provide laboratory reference data that may be regarded as 'exact' for comparisons with astrophysical spectra. Besides high accuracy it is particularly important to provide isotopically resolved data. Magnesium

[2] $z = 1$ corresponds to about $8 \cdot 10^9$ years ago, $z = (\nu_{emit} - \nu_{obs})/\nu_{obs}$.
[3] www.keckobservatory.org
[4] Very Large Telescope, www.eso.org

has three stable isotopes with mass numbers 24, 25 and 26 (natural abundances on earth 79:10:11), and the $^{26-24}Mg^+$ isotope shifts for the 3s-3p lines amount to about 3 GHz. Different Mg^+ abundances in the investigated astronomical objects were identified as an important source of systematic errors in many-multiplet analyses, moreover, an investigation of the chemical evolution of isotope abundances itself is of interest [18, 19, 95, 96, 97]. Both the fine-structure constant and the isotopic abundance in the investigated object can be obtained from the fit to the astrophysical spectra once the isotope shifts are accurately known [19, 97].

Constraints by optical clocks

Terrestrial comparisons of optical clocks based on different atomic transitions set strong constraints on present-day temporal variations of α. Optical clocks may only be compared on time scales of years, but their tremendous accuracy allows to probe temporal variations of α about an order of magnitude more accurately than many-multiplet studies, if a linear drift over 10^{10} years look-back time is assumed. Measurements of an Al^+ clock against a Hg^+ clock at NIST suggested $\dot{\alpha}/\alpha = (-1.6 \pm 2.3) \cdot 10^{-17}$/year [98]. A spatial variation of the fine-structure constant may be probed by a comparison of clocks over the course of a year. It was estimated in [99], that a two-orders of magnitude improvement in the measurement sensitivity of optical clocks is required to confirm or contradict the reported spatial dipole variation [17].

4.2. Spectroscopy method

Spectroscopy on strong transitions in trapped ions

Todays most precise spectroscopic measurements probe narrow transitions in single trapped ions. The fractional frequency uncertainty for the Al^+-Mg^+ clock at NIST is below 10^{-17} [41]. Key prerequisites [100] for such a precision are laser-cooled ions at the field-free center of a RF trap, narrow-linewidth transitions, high-fidelity readout of single-photon events via electron shelving [32], and a (first-order) Doppler and recoil free absorption spectrum in the trap potential [101] similar to Mößbauer spectroscopy. The latter requires strong binding conditions, i.e. the linewidth Γ of the probed transition is small against the trap frequency ω_s, a valid assumption for narrow optical transitions in RF ion traps.
The Mg^+ 3s-3p lines are strong dipole-allowed transitions and require different spectroscopic approaches. The favorable sideband-resolved absorption spectrum is hard to establish since the natural linewidth $\Gamma/2\pi = 41.8$ MHz well exceeds typical secular trap frequencies. In the weak binding limit $\omega_s \ll \Gamma$ the motional sidebands overlap and form a continuous Voigt-type fluorescence profile, as it is the case for an unbound atom. The detection of the fluorescence signal with good signal-to-noise

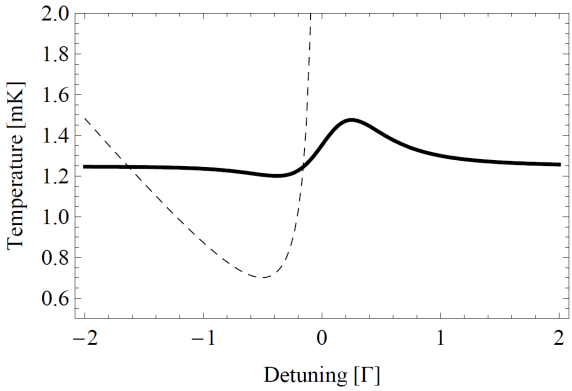

Figure 4.3.: Equilibrium temperatures for a two-ion model. One ion is laser cooled at a detuning of $\delta/2\pi = -64$ MHz and saturation parameter $S_{0,c} = 0.5$, the other ion is addressed by a scanning laser at $S_{0,s} = 0.004$. The dashed line shows the uncooled spectroscopy ion for comparison ($S_{0,c} = 0$, see Figure 2.3) and illustrates the need to suppress detuning dependent line shape distortions. Taken from [50].

ratio requires many scattering events, which changes the equilibrium temperature of the ion according to Equation 2.21. A single laser beam adiabatically tuned from the low frequency side over the resonance, will lead to a detuning-dependent temperature and thus results in a strongly distorted Voigt profile with varying thermal (Gaussian) contribution to the linewidth. The equilibrium temperature diverges near resonance, since the heating effect from the stochastic redistribution of photons overcomes the cooling power (Figure 4.3), the driven ion evades the laser beam and the fluorescence drops towards zero. The fluorescence rate reaches its maximum slightly red-detuned to the transition frequency (Inset in Figure 4.7). The position of this fluorescence peak with respect to the line center is hard to predict, since it depends on additional parameters which are difficult to control, like electronic heating mechanisms in the ion trap.

A precision measurement on dipole-allowed transitions requires the suppression of these adverse temperature variations induced by the spectroscopy laser. Previously used approaches in ion traps include a two-laser method [2], a double resonance scheme [3], buffer gas cooling [102] and chopped detection [12]. Our spectroscopy technique is based on continuous sympathetic cooling and spatially separated fluorescence detection. The method was developed by Maximilian Herrmann and is described in detail in [15] and [50], here we will review basic features. A crystallized chain of ions is prepared and continuously Doppler-cooled at one side only (see Figure 4.4). A weak spectroscopy laser probes sympathetically cooled ions at the other end of the chain. Here we collect a basically background-free fluorescence signal. This arrangement not only minimizes background counts but also the ac Stark shift from the cooling laser. Our spectroscopy technique allows us to record nearly unperturbed Voigt profiles with high signal-to-noise ratio (Figure 4.7). The influence

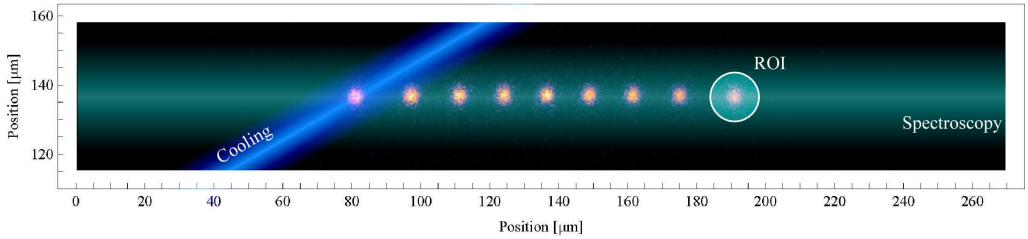

Figure 4.4.: An artist's view on our spectroscopy technique. A tightly focused laser beam cools an ion chain at one side only. A weaker spectroscopy beam is applied on axis to be insensitive to radial micro-motion. An imaging photo-detector together with software allows us to extract an essentially background-free fluorescence signal from a region-of-interest (ROI) around a single, sympathetically cooled ion. Taken from [50].

of residual line-shape distortions is discussed in the next section.

Accuracy of the spectroscopy method

The presence of the weak spectroscopy laser introduces residual detuning-dependent temperature variations (Figure 4.3). Their impact on the measurement accuracy was investigated in Chapter 3.2 in [50]. The quantitative analysis was based on a two-ion model. One ion is continuously laser cooled at constant red detuning $\delta/2\pi = -64$ MHz, while the other ion is addressed by a scanning spectroscopy laser. Both ions are at common equilibrium temperature, since they equally share the motional energy of both eigenmodes in the harmonic trap potential. Expressions for the cycle-averaged cooling or heating power of the near-resonant laser beams and the heating power due to the random recoil-kicks by re-distributed photons from both beams are given by Equations 2.19 and 2.20. Equilibrium temperatures are evaluated from a power balance condition for different detunings and laser intensities (Figure 4.3). Artificial scattering profiles are generated with different Gaussian contributions at each detuning of the spectroscopy laser, according to the respective equilibrium temperature. Then a Voigt profile is fitted to this artificial data-set and the offset of the fitted line center from the real transition frequency is determined. For the Mg^+ 3s-3p transitions ($\Gamma/2\pi = 41.8$ MHz) the deviation of the fitted line center was smaller than 4 kHz even for intensity ratios between the spectroscopy laser and the cooling laser $r = S_{0,s}/S_{0,c}$ close to one (see Figure 3.12 in [50]), which enables a measurement at high signal-to-noise ratios.
The measurements themselves were performed with chains of about 8-10 ions for practical reasons. The case of longer chains is more complicated since individual ions show different velocity amplitudes for most of the eigenmodes of the system (Section 2.3.2). In our spectroscopy scheme we cool ions at one end of a chain,

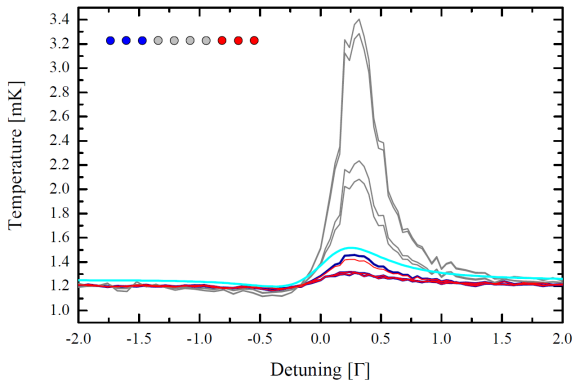

Figure 4.5.: Molecular dynamics simulation of sympathetic cooling along a chain of 10 ions. Three ions are cooled at $\delta/2\pi = -64$ MHz and $S_{0,c} = 0.5$ (blue dots, blue curves), while an on-axis spectroscopy laser at $S_{0,s} = 0.0007$ interacts with all ions (compare to Figure 4.4). Three spectroscopy ions are indicated by red dots (red curves). The cyan line shows the two-ion model for comparison. From the agreement we infer that the findings from the two-ion model also apply for short ion chains. Sympathetic cooling of the center ions (grey dots, grey curves) is considerably less efficient due to the symmetry in the eigenmode structure of the chain (Section 2.3.2 and Figure 5.1), which is in sharp contrast to the heat conductivity model in macroscopic solid state systems. Taken from [50].

which damps the eigenmodes with different efficiency. Yet the eigenmode structure is symmetric, which gives rise to an efficient coupling of cooling ions and spectroscopy ions at opposite ends of the chain. Molecular dynamics simulations by Thomas Udem showed that sympathetically cooled ions at one end of a 10-ion chain are cooled just as efficiently as directly cooled ions at the opposite end (Figure 4.5). Therefore we are confident that the two-ion model is a good approximation for our measurement.

4.3. Measurements

Most components of our setup were already described in Chapter 3, including the vacuum system (Section 3.2.5), the linear endcap ion trap (Section 3.2.2) and ion creation by resonant photo-ionization (Section 3.3). Cooling and spectroscopy light was either provided by a frequency doubled dye laser (Section 3.1.3) or a frequency quadrupled fiber laser system at 1118 nm (Section 3.1.1). The fiber laser system could only interact with the D_2 transition since its tuning range was limited to 90 GHz, while the fine-structure splitting amounts to 2.7 THz.
Schematics of two different beam geometries are depicted in Figures 3.1 and 4.6. Because of failures of the fiber laser, cooling and spectroscopy beams were generated most of the time by the frequency doubled dye laser only. In this case we split the UV output and send the beams through two double-pass acousto-optic modulator

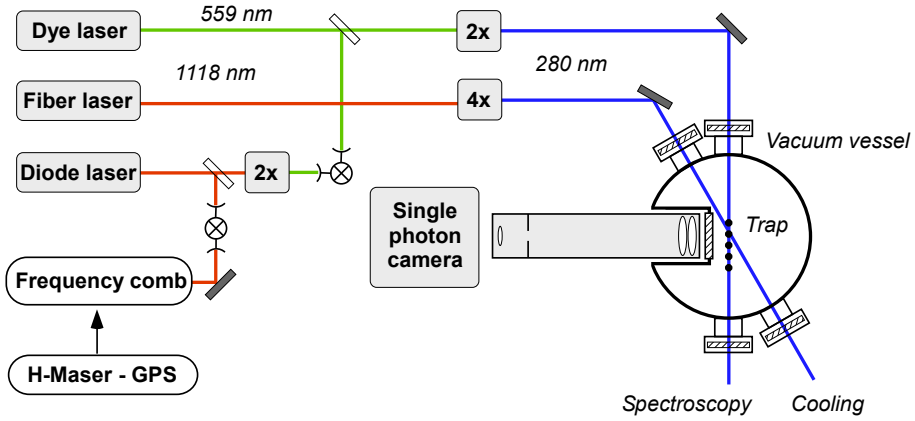

Figure 4.6.: Simplified schematic setup. The laser frequencies are phase-locked to a GPS disciplined hydrogen maser. The phase-coherent link between the RF reference and the UV regime via a fiber laser frequency comb and a transfer diode laser is only shown for the spectroscopy dye laser. Color changes indicate frequency conversion. Figure 3.1 shows an alternative scheme, where we produce cooling and spectroscopy light from a single laser source with a double-pass AOM setup (Section 3.1.5).

setups (Section 3.1.5), where we independently control the frequency and intensity of both beams. The practical tuning range of the spectroscopy laser was hereby limited to about 180 MHz, since the diffraction efficiency of the scanning double-pass AOM drops towards the edges of the tuning range. The corresponding intensity variations over the tuning range were compensated within the dynamic range of our intensity stabilization, yet the intensity locks were slightly less stable at the edges of the tuning range. Scanning the double-pass AOMs also caused frequency-dependent beam profile distortions (Figure 4.9), which were suppressed by spatial filtering with a small pinhole (diameter 15 μm).

These problems were avoided when independent cooling and spectroscopy laser systems were available. A schematic setup using both lasers is shown in Figure 4.6. Here, the spectroscopy laser was tuned by changing an offset lock frequency in loop (Section 3.1.6) and an AOM stabilized the intensity at constant drive frequency. The enhanced tuning range is then technically limited by the bandwidth of the locking electronics and less variations in the input intensity are beneficial for the performance of the intensity stabilization. The AOM at fixed frequency is not expected to cause detuning-dependent beam profile distortions, however we still continue spatial filtering with the 15 μm pinhole.

The intensities of the cooling and the spectroscopy laser were set to saturation parameters $S_{0,c} \approx 0.5$ and $S_{0,s} \approx 7 \times 10^{-4}$ in units of the saturation intensity ($I_{sat} \sim 2497$ W/m^2). The cooling beam was detuned $\delta/2\pi = -64$ MHz below resonance ($\Gamma/2\pi = 41.8$ MHz) and tightly focused to a beam waist of $w_0 \approx 20\,\mu$m. The beam enclosed an angle of about 15° with the trap axis predefined by the optical

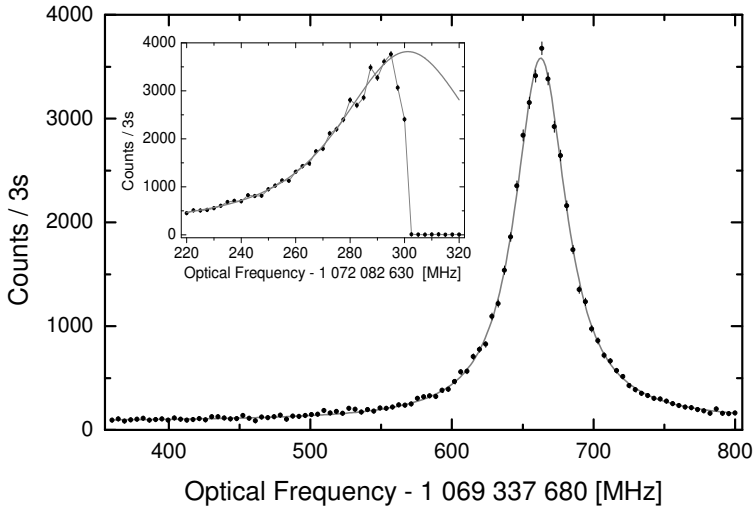

Figure 4.7.: 450 MHz wide demonstration scan across the $^{24}Mg^+$ D_1 resonance. Fluorescence photons were collected for 3s per data point, the detunings where randomized in order. For measurement runs we restricted the tuning range to 180 MHz around the line center and record 30-40 data points. Inset: For comparison we show an asymmetric $^{24}Mg^+$ D_2 line profile scanned from the low frequency side, overlayed is a Voigt fit to the rising edge, which was artificially centered around the measured transition frequency. Here the ion was essentially uncooled, only a weak cooling beam was superimposed to prevent fluorescence breakdown during the scan time.

access of our vacuum vessel. Given that geometry we found optimal experimental conditions when we cooled 2-3 outer ions of a chain containing 8-10 ions. This enabled spectroscopy at low background on 2-3 ions at the other end of the chain. Working with shorter chains decreased the number of low background spectroscopy ions and therefore statistics, longer chains increased the probability that a MgH^+ ion was generated by a chemical reaction with the background gas. Dark MgH^+ ions are embedded in the chain and change their site on time scales of few seconds, while the recording of one line scan took about two minutes. Once a non-resonant ion enters the cooling or spectroscopy region it turns dark, which alters the cooling dynamics and disturbs the fluorescence recording. We therefore discarded such a measurement run and reloaded our trap once an impurity ion was observed. Towards the end of the measurement we found out that dark MgH^+ ions can be conveniently removed from the chain, when we applied a radial radio frequency field resonant to the radial secular frequency of MgH^+.

The spectroscopy beam collinear with the ion chain was loosely focused to about

Table 4.1.: Absolute transition frequencies for individual isotopic components. Pickering and co-workers do not explicitly specify an uncertainty for the $^{24}Mg^+$ component (see Table 1 in [103]), for comparison we adopt the 60 MHz uncertainty of the composite line. All frequencies are given in MHz.

Transition	This work	Drullinger [2]	Pickering [103]
$^{24}Mg^+$ D_1	1 069 338 342.56(16)	-	1 069 338 293(60)
$^{26}Mg^+$ D_1	1 069 341 427.47(16)	-	-
$^{24}Mg^+$ D_2	1 072 082 934.33(16)	1 072 082 833(120)	1 072 082 862(60)
$^{26}Mg^+$ D_2	1 072 086 021.89(16)	1 072 085 883(156)	-

$w_0 \sim 200$ μm in the trapping region. Every single measurement consisted of 30 - 40 frequency points within a 180 MHz ($> 4\ \Gamma/2\pi$) wide range around the line center. Fluorescence photon counts were recorded for 3 s at each detuning. The chronological order of probe laser frequencies was randomized for each line scan to be insensitive to a variety of possible drifts. We collect fluorescence with our imaging photo detection system (Section 3.4). Our raw data consists of time-averaged images of the ion chain, which encode a spatially resolved count rate. For stray light suppression we adjust our imaging optics such that only spectroscopy ions are in the field of view. To read out the fluorescence of a single ion we set a circular region of interest around an ion (Figure 4.4) using our data evaluation software. An example for an extensive line scan is shown in Figure 4.7.

Figure 4.8 shows our measurement of the $^{24}Mg^+$ D_2 line on eleven measurement days (264 line scans, statistical uncertainty 15 kHz), the $^{26}Mg^+$ D_2 line on six measurement days (152 line scans, statistical uncertainty 14 kHz) and the $^{24}Mg^+$ D_1 line on five measurement days (119 line scans, statistical uncertainty 20 kHz). After one measurement day of the $^{26}Mg^+$ D_1 component (Measurement Day 5 in Figure 4.8c) we had a technical problem with our ion trap. The 92 kHz statistical uncertainty of this measurement day is already smaller then our systematic uncertainty estimate of 160 kHz (see Section 4.4). Fortunately we had performed a backup measurement on all components before we proceeded with statistically improved measurements of the individual lines. This data is presented as Measurement Day 1-4 in Figure 4.8c and was taken about three month prior to the last data point. Overall we recorded 67 $^{26}Mg^+$ D_1 line scans in five measurement days and the statistical uncertainty reached 32 kHz (see Figure 4.8c). The numerical values of the transition frequencies are given in Table 4.1.

From the transition frequencies we deduce isotope shifts and fine-structure splittings (Table 4.2). We point out that our measurement uncertainty is sufficient to resolve the $^{26-24}Mg^+$ isotope shift of the fine-structure interval for the first time.

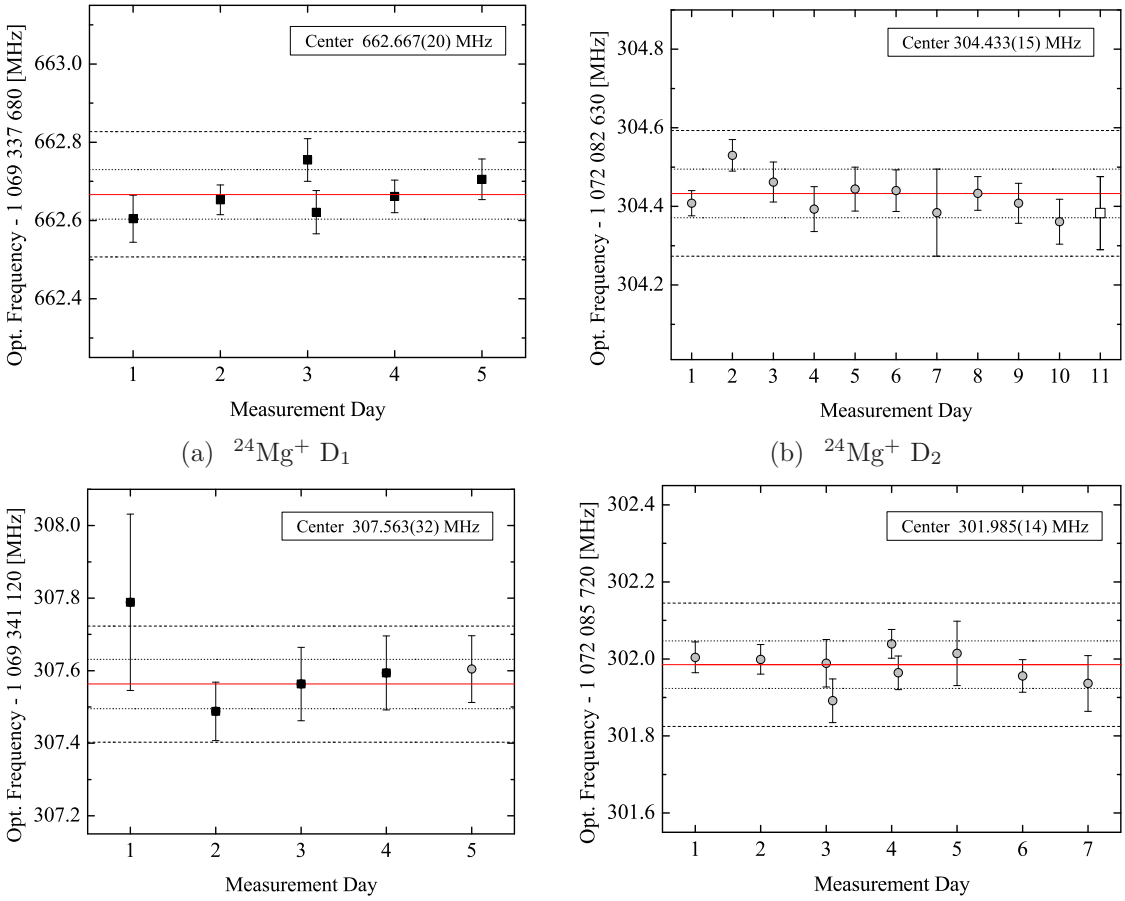

(a) $^{24}Mg^+$ D_1 (b) $^{24}Mg^+$ D_2

(c) $^{26}Mg^+$ D_1 (d) $^{26}Mg^+$ D_2

Figure 4.8.: Measurements of the D_1 and D_2 transition frequencies in $^{24}Mg^+$ and $^{26}Mg^+$ (red lines). Outer dashed lines represent the 160 kHz uncertainty on the absolute transition frequencies due to possible asymmetries in the dye laser spectrum (Section 4.4). This effect is expected to be suppressed for relative quantities. Inner dotted lines represent the reduced error bar for the evaluation of isotope shifts and fine-structure splittings (Table 4.2). Day 11 in the $^{24}Mg^+$ D_2 measurement (hollow square) is the only data point that was taken with the fiber laser (Section 3.1.1). All remaining data was taken with the dye laser (Section 3.1.3), since the fiber laser is not resonant to the D_1 transition and was only operational at one D_2 measurement day. Filled squares indicate measurements with two laser systems according to Figure 4.6, circles indicate measurements with the double-pass AOM scheme described in Figure 3.1.
Note: Optical frequencies in this figure correspond to our experimental data and represent the counted frequencies of the spectroscopy laser. The transition frequencies listed in Table 4.1 are corrected for the recoil shift and thus differ by -106 kHz from $^{24}Mg^+$ and -98 kHz from $^{26}Mg^+$ measurement frequencies.

Table 4.2.: Isotope shifts ($\delta\nu^{A',A}$) of the D_1 and D_2 lines, fine-structure splittings (FS) of both isotopes and the isotope shift of the fine-structure splitting deduced from our absolute frequency measurements. The error bars are reduced due to common mode rejection of systematic effects. Only the isotope shift of the D_2 line was measured before (3050 (100) MHz [2]) and is in agreement with our three orders of magnitude more accurate result.

$\delta\nu^{26,24}$ D_1 ($3s_{1/2}$-$3p_{1/2}$)	3084.905 (93) MHz
$\delta\nu^{26,24}$ D_2 ($3s_{1/2}$-$3p_{3/2}$)	3087.560 (87) MHz
$^{24}Mg^+$ FS ($3p_{1/2}$-$3p_{3/2}$)	2 744 591.767 (88) MHz
$^{26}Mg^+$ FS ($3p_{1/2}$-$3p_{3/2}$)	2 744 594.422 (92) MHz
$\delta\nu^{26,24}$ FS ($3p_{1/2}$-$3p_{3/2}$)	2.66 (13) MHz

4.4. Measurement uncertainty

Our estimate of the measurement uncertainty is 160 kHz and it was dominated by a possible asymmetry in the frequency spectrum of our spectroscopy dye laser (Section 3.1.3). Due to cancellation of this effect we reduce our uncertainty estimate for relative quantities, like isotope shifts and fine-structure splittings, as we discuss in this section.

Beam profile

At an immature stage of our experiment we suffered from reproducible, frequency-dependent distortions of the spectroscopy laser's intensity profile (Figure 4.9). The distortions were induced by the scanning double-pass AOM (Section 3.1.5) and were observable with a beam profiling camera. Apparently the Bragg grating in the modulator showed inhomogeneities characteristic to the drive frequency. The spectroscopy beam collinear with the ion chain was stabilized in intensity and loosely focused to about $w_0 \sim 200\,\mu$m beam waist, while the radial motion of a single ion is confined below 1 μm. We stabilized the total laser intensity, but the ions sampled local, frequency-dependent intensity variations. This resulted in a reproducible alignment sensitivity of the line center returned from Voigt fits to the data. It was possible to shift the fitted 'line center' by as much as 1 MHz when we displaced the spectroscopy beam. Filtering with a 15 μm size pinhole[5] removed apparent beam profile distortions and the alignment sensitivity of the line center was suppressed below the day-to-day reproducibility level of our measurement (about 60 kHz). Binning the data into measurement days serves as an important consistency check against

[5]Single mode fiber would have been beneficial for spatial filtering and beam pointing stability, however, we are not aware of single mode fibers available for 280 nm

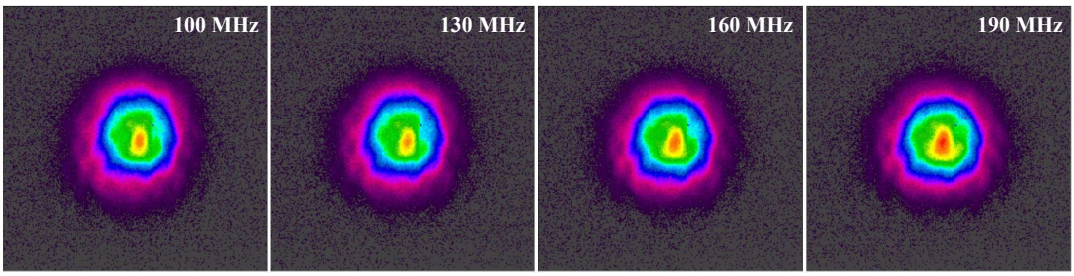

Figure 4.9.: Reproducible changes in the beam profile of the spectroscopy laser at different drive frequencies of our double-pass AOM. Frequency dependent local intensity variations, at stabilized total intensity, shifted the fitted line centers by as much as 1 MHz. Spatial filtering with a 15 μm pinhole removed these distortions.

this and possible other systematics induced by operators and the laboratory environment.

Magnetic fields

The D_2 transition shows two magnetic sublevels for the $s_{1/2}$ ground state and four magnetic sublevels for the $p_{3/2}$ excited state. Magnetic fields in direction of the spectroscopy laser therefore shift the line center if the polarization is not perfectly linear. To compensate such shifts we introduced a quarter-wave plate (QWP) into the beam path. We rotated the QWP in 45° steps and measured the line center as function of the polarization. We observed the expected sinusoidal modulation of the line center with a maximum amplitude of 950 kHz for all line scans, a sinusoidal fit to the data compensates linear Zeeman shifts (see Figure 4 in [15]). Each measurement day in Figure 4.8b and 4.8d consisted of at least one QWP rotation scan. Since the $s_{1/2}$ and $p_{1/2}$ levels show two magnetic sublevels each, only line broadening is expected for the D_1 line. Nevertheless we continued with the QWP evaluation scheme to rule out unexpected polarization effects on the line center. No statistically significant polarization dependence of the D_1 line was observed.

Laser spectrum

We assume that the limiting systematic uncertainty is introduced by possible asymmetries in the rather broad spectrum of the frequency-doubled dye laser. The laser linewidth was several MHz in the UV, while the statistical uncertainty of the $^{26}Mg^+$ D_2 measurement was 14 kHz only. The fluorescence profile is a convolution of the atomic response and the laser spectrum. Therefore it is crucial to estimate possible asymmetries in the frequency spectrum of the spectroscopy laser. The dye laser was phase-locked to a frequency comb via a frequency doubled diode laser (Figure 4.6). The frequency spectrum of both involved lasers may shift against

the phase-locked carrier frequency. Correlated amplitude and phase modulation is an exemplary effect, which can lead to asymmetries in the otherwise Gaussian frequency spectrum of our dye laser. To understand the mechanism imagine two pairs of amplitude and phase modulation sidebands at a common modulation frequency. Amplitude modulation sidebands are in phase, while phase modulation sidebands are out of phase with each other. Thus the superposition of both sidebands can produce an asymmetry in the laser spectrum. To quantify this effect, we measured the in-loop heterodyne beat note between the frequency doubled transfer diode laser and the dye laser (Figure 4.6) with a properly referenced spectrum analyzer. We fitted a Gaussian profile to the beat note and found an average deviation from the offset lock frequency of 80(60) kHz at 560 nm, we double this value and assume an uncertainty of 160 kHz in the UV. We can not ultimately judge whether the transfer diode laser or the spectroscopy dye laser or both lasers caused the observed asymmetry in the beat note. Correlated amplitude and phase modulation is frequently oberved in laser diodes, in this case the asymmetry would not result in a shift of the measured transition frequency, since the phase-locked carrier frequency is the decisive quantity of the transfer laser. Yet we measure the transition frequency to a fraction of the spectroscopy laser linewidth and we think that the observed asymmetry in the beat note measurement is a justified quantification of our concerns of possible asymmetries in the broad dye laser spectrum. A consistency check with the frequency quadrupled fiber laser, which was directly locked to the IR frequency comb and should differently suffer from this effect, gave good agreement with the $^{24}Mg^{+}$ D_2 measurement (Measurement Day 11 in Figure 4.8b).

Further systematic effects

The method-inherent shifts due to residual temperature effects were quantified in [50] and reviewed in Section 4.2. They are expected to be smaller than 1 kHz for cooling laser intensity to spectroscopy laser intensity ratios typical to our experimental conditions. The Voigt fits to our data return an average reduced χ^2 close to one, which confirms the assumptions of our models.
Other systematic effects are: ac Stark shift due to residual intensity from the cooling laser at the position of the spectroscopy ion ($<$ 30 kHz), dc Stark shift from the trapping fields (0.1 Hz) and second-order Doppler shift (-0.3 Hz) [15]. A comparison between the free-running maser and the global positioning system showed a relative deviation smaller than 1.7×10^{-13} over the whole measurement period, i.e. the reference frequency from the free-running maser was sufficiently accurate for our purpose. The results given in Table 4.1 are corrected for the recoil shift of -106 kHz for $^{24}Mg^{+}$ and -98 kHz for $^{26}Mg^{+}$ transition frequencies.

Relative quantities

The reproducibility of our measurement over time periods of days and months indicates that the systematic uncertainty due to asymmetries of the exciting laser spectrum enters rather as a constant offset on the absolute frequency, than as a time-varying scatter. We therefore assume that the uncertainty of isotope shifts and fine-structure splittings is reduced due to cancellation in the difference calculation. A quadratic addition of the line center uncertainties would therefore overestimate the uncertainty of these difference quantities. But what is a proper uncertainty estimate then? The reproducibility over time and against changes in the setup indicates that the statistical uncertainty of a typical measurement day (60 kHz) is an appropriate upper bound on systematic deviations due to drifting asymmetries of the laser spectrum and residual detuning-dependent distortions of the intensity profile. We therefore quadratically add a systematic deviation of 60 kHz to the statistical uncertainty of the involved transition frequencies, when we determine the relative quantities summarized in Table 4.2. We note that the D_1 line was predominantly measured with two laser systems, while the D_2 line was measured with the double-pass AOM scheme (Figure 4.8), yet we always used the same spectroscopy laser except for one measurement day.

Mode number determination

The accuracy of comb-based frequency calibration demands an unambiguous determination of the mode number of the frequency comb. The determined center frequency may differ vastly from the real value, if the mode number of the comb was mistaken or any offset frequency was added with a wrong sign. The absolute frequency calibration was based on a frequency comb with 100 MHz repetition rate and 20 MHz carrier offset frequency, a mistaken mode number results in an error of 400 MHz, a wrong sign of the offset frequency amounts to 160 MHz in the UV. The signs of all involved offset frequencies were independently checked by different operators and the mode number associated with the $^{24}Mg^+$ D_2 component was determined with an additional fiber laser frequency comb of 250 MHz repetition rate[6]. The wavelength was measured with a High Finesse WS-7 wavemeter which is based on cascaded Fizeau interferometers, the specified accuracy of the wavemeter is 60 MHz. Two further wavemeters confirmed the fundamental wavelengths of our laser systems: A second WS-7 wavemeter, which showed consistent wavelengths for an accurately known laser for hydrogen spectroscopy and a Burleigh 1500WA wavemeter with internal He-Ne reference laser. We deduced the mode number for the remaining transitions relative to the known $^{24}Mg^+$ D_2 component. Here we used two independent wavemeters with a relative accuracy considerably better than the

[6]The usual approach is changing the repetition rate of a single frequency comb. We enjoyed the unusual comfort of two frequency combs delivered via optical fiber [65].

repetition rate of the 100 MHz frequency comb.
Our transition frequencies are in agreement with measurements based on ArII [20, 103, 104, 105, 106], MgI [20] and iodine wavelength calibration [2] (Figure 4.11). The fine-structure splittings are consistent with results for composite lines from Fourier transform spectroscopy [20, 103, 104, 105, 106] (the wavenumber uncertainty of ArII calibration drops out here). The isotope shift measurement by Drullinger and co-workers [2] as well as theoretical isotope shift predictions further validate the mode number of $^{26}Mg^+$ components with respect to the $^{24}Mg^+$ transition frequencies (Figure 4.10). A more detailed comparison with related measurements is given in Section 4.7.

4.5. Comparison with theoretical isotope shift predictions

Isotope shifts of atomic energy levels reflect the fact that atomic nuclei are not point-like charged objects with infinite mass. The isotope shift is defined as the difference between the frequency of corresponding transitions in different isotopes. All energy eigenstates in both atomic systems are shifted, because of differences in the reduced mass and non-vanishing electron wave functions within the spatial distribution of nuclear charge. The former effect due to different nuclear recoils is called 'mass shift', the charge distribution effect is called 'volume' or 'field' shift. The recoil energy shift results from the kinetic part of the Hamiltonian $(\sum \vec{p}_i)^2/2\mu$, where μ is the reduced mass of the electron-nucleus system. In many-electron atoms it is usually treated as the sum of the so-called normal mass shift (NMS) given by $\sum p_i^2/2\mu$ and the specific mass shift (SMS) $\sum_{i<j} \vec{p}_i\vec{p}_j/\mu$. The SMS reflects correlations between the electron momenta and is therefore more difficult to compute. The frequency shift for a transition between isotopes with atomic masses A' and A, respectively, can be written as [8, 107]

$$\delta\nu^{A',A} = (k_{\mathrm{NMS}} + k_{\mathrm{SMS}})(\frac{1}{A'} - \frac{1}{A}) + F_{FS}\ \delta\left\langle r^2\right\rangle^{A',A}, \tag{4.4}$$

where $\delta\nu^{A',A} := \nu^{A'} - \nu^A$ is the difference in the transition frequencies, k_{NMS} and k_{SMS} are the normal and specific mass shift constants, F_{FS} is the field shift constant and $\delta\left\langle r^2\right\rangle^{A',A} := \left\langle r^2\right\rangle^{A'} - \left\langle r^2\right\rangle^{A}$ is the difference between the root-mean-square (rms) nuclear charge radii of the involved isotopes. In case all involved constants are accurately known it is possible to probe nuclear charge distribution from precision spectroscopy of orbiting electrons.
Let us investigate Equation 4.4 in more detail. The normal mass shift constant is given to first order by $k_{\mathrm{NMS}} = -\nu m_e/\mathrm{amu}$ (transition frequency ν, electron mass m_e), here we use slightly corrected relativistic values from Table V in [21].

The NMS between $^{26}Mg^+$ and $^{24}Mg^+$ amounts to 1877.1 MHz for the D_1 line and 1879.3 MHz for the D_2 line[7]. F_{FS} and k_{SMS} are determined numerically, recent investigations [8, 21, 22, 109, 110] treat the 3s-3p energy levels in Mg^+. We use tabulated nuclear charge radii compiled from electron scattering and muonic atom x-ray data [111] and obtain a $^{26-24}Mg^+$ field shift of 18(20) MHz. The uncertainty of the field shift is dominated by experimental nuclear charge radii, while differences in the determination of F_{FS} are insignificant[8]. We may therefore treat the field shift as a common contribution to all theoretical isotope shifts. Values for total isotope shifts are plotted in Figure 4.10 and essentially reflect differences in the evaluation of the SMS. Following [8] we may also subtract the field shift and the normal mass shift to obtain an 'experimental value' for the SMS. Here we find 1189.9(20.0) MHz for the D_1 and 1190.3(20.0) MHz for the D_2 line. The 20 MHz uncertainty is due to common nuclear charge radii [111] and the difference of 0.4 MHz between the D_1 and the D_2 line may be meaningful on a 1 MHz scale or better, as indicated by the number of significant digits given in the theoretical treatments. Only the authors of [8] give uncertainties for their evaluation of the SMS, the uncertainty introduced by k_{SMS} and the uncertainty of the field shift are both on the order of 20 MHz. Thus our considerably more precise measurement can unfortunately neither set an accurate calibration point for SMS investigations nor give rigorous isotopic differences in the nuclear charge distribution. Yet the results of [8] and our measurement are in good agreement. Combining our results with the values given for k_{SMS} and F_{FS} from [8] allows to deduce the difference in the rms nuclear charge radii. Here we find $\delta\langle r^2\rangle^{24-26}$= 0.06 (15) fm^2 from the D_2 line and $\delta\langle r^2\rangle^{24-26}$= 0.07 (30) fm^2 from the D_1 result, consistent with the tabulated value of 0.14 (16) fm^2 [111].
The accuracy of our measurement resolves the $^{26-24}Mg^+$ isotope shift of the $3p_{1/2}$-$3p_{3/2}$ fine-structure splitting for the first time and we are presumably sensitive to relativistic effects in the 3s-3p isotope shifts. One result of the relativistic treatment by Korol and co-workers [21] was, that the final relativistic mass shifts for levels of a multiplet appear to be closer to each other, compared to mass shifts obtained with non-relativistic operators. This gave rise to a difference in the determined 3s-3p mass shifts of 2.2 MHz and -14.4 MHz for the relativistic and non-relativistic treatment, respectively (see Table V in [21]). The influence of inaccurately known field shifts is suppressed here and our measured value of 2.66 (13) MHz for the total isotope shift of the fine-structure splitting supports the relativistic result.

[7] We use masses from a compilation of Audi [108]. Atomic masses are measured with high precision and do not limit our investigations.

[8] Different values for F_{FS} result in marginally different field shifts between 17.6 MHz [110] and 18.1 MHz [21], Berengut and co-workers estimate an error smaller than 5 % for F_{FS}[8]. An updated set of nuclear charge radii was published in [112], the ^{24,25,26}Mg charge radii are slightly adjusted and the result for the field shift is 18(19) MHz. The authors do not specifically state if optical isotope shifts entered into the adjustment so we stay with the more transparent data compiled in [111].

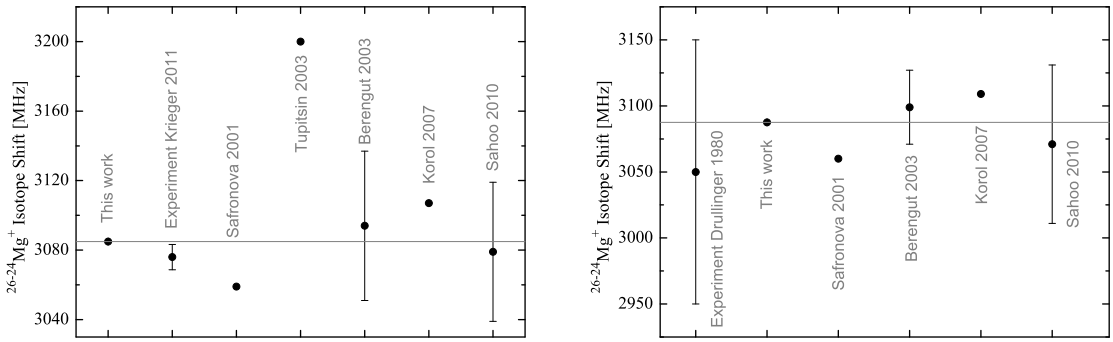

(a) $^{26-24}Mg^+$ isotope shift D_1 (b) $^{26-24}Mg^+$ isotope shift D_2

Figure 4.10.: Comparison of measured [2, 23] and predicted [8, 21, 22, 109, 110] $^{26-24}Mg^+$ isotope shifts. The field shift contributions of +18 (20) MHz (limited by experimental nuclear charge radii [111]) are included in theoretical investigations and set the minimum uncertainty level for the comparison of our measurement (see Table 4.2), which may be regarded as 'exact' on this scale. Uncertainty estimates for total theoretical isotope shifts are only given by Sahoo [22], uncertainties for the SMS contributions are given by Berengut [8]. Only the result of Korol and Kozlov [21] includes a relativistic treatment of the normal mass shift.

4.6. $^{25}Mg^+$ transition frequencies

Although we have not measured $^{25}Mg^+$ transition frequencies we are able to deduce them from $^{24,26}Mg^+$ measurements with good accuracy. $^{25}Mg^+$ has a nuclear spin $I = 5/2$. A measurement of $^{25}Mg^+$ transition frequencies requires additional laser beams for repumping from dark hyperfine states. The ground state (3s) hyperfine splitting of 1.788 GHz [113] is not easily bridged by modulation techniques[9]. It is possible to produce repumper beams for both the spectroscopy and the cooling laser, from the two available laser systems in our lab. But the fiber laser system was not operational at the appropriate time and the measurement scheme would have required a considerable change in the optical setup. Therefore we decided to proceed with the ion oscillator work described in Chapter 5, which was run in parallel.
Yet, having measured the $^{26-24}Mg^+$ isotope shifts, we can deduce $^{25}Mg^+$ transition frequencies. It is possible to evaluate $^{25-24}Mg^+$ isotope shifts directly from Equation (4.4), but we prefer to express the sum of the mass shift constants in terms of the accurately measured $^{26-24}Mg^+$ isotope shift and arrive at

$$\delta\nu^{25,24} = a\ \delta\nu^{26,24} + F_{FS}\ (\delta\left\langle r^2\right\rangle^{25,24} - a\ \delta\left\langle r^2\right\rangle^{26,24}), \tag{4.5}$$

[9] Modulators at 280 nm are not readily available at this frequencies. Other ion trapping groups use cascaded acousto optical modulators to bridge this splitting.

where $a = \frac{m_{26}(m_{25}-m_{24})}{m_{25}(m_{26}-m_{24})}$. Equation 4.5 eliminates the uncertainty in the specific mass shift from the treatment and we deduce $^{25-24}Mg^+$ isotope shifts with an uncertainty of 19 MHz using field shift constant determinations F_{FS} from [8, 109, 110] and tabulated root-mean-square nuclear charge radii [111]. The results are: $\delta\nu^{25,24}Mg^+$ D_1 = 1620.0 (19.1) MHz and $\delta\nu^{25,24}Mg^+$ D_2 = 1621.4(19.1) MHz, again the difference of 1.4 MHz between both components may be meaningful due to common uncertainties in the nuclear charge distribution.
Knowing the $^{25-24}Mg^+$ isotope shift one can evaluate transition frequencies between $^{25}Mg^+$ hyperfine structure levels relative to the hyperfine centroid. The magnetic dipole and electric quadrupole hyperfine energies W_{M1} and W_{E2} are given by [114]

$$W_{M1} = \frac{A}{2}K, \tag{4.6}$$

and

$$W_{E2} = \frac{B}{2}\frac{3K(K+1) - 4I(I+1)J(J+1)}{2I(2I-1)2J(2J-1)}, \tag{4.7}$$

where $K = F(F+1) - I(I+1) - J(J+1)$, A and B are the magnetic dipole and electric quadrupole hyperfine constants, I and J are the nuclear and orbital angular momenta and F denotes the total angular momentum. The ground state hyperfine constant was accurately measured in [113]. Magnetic dipole hyperfine constants for 3p states in $^{25}Mg^+$ are evaluated in [114, 115, 116]. Differences in the computations of magnetic hyperfine constants amount to a maximum deviation of 3.5 MHz ($3p_{3/2}$,F=1) [114, 115]. The electric quadrupole hyperfine constant for the $3p_{3/2}$ state is only given in [114]. Uncertainty estimates for theoretical hyperfine constants are not given, but the experimental value of the ground state hyperfine constant was reproduced within 0.6%. The largest shift to any 3p state amounts to 180 MHz ($3p_{1/2}$,F=2), the uncertainties of the 3p hyperfine constants (assuming that they are smaller than 10%) may therefore be neglected against the 19 MHz uncertainty in the determination of the $^{25}Mg^+$ hyperfine centroid. Using hyperfine constants tabulated in [114] we deduce the whole hyperfine structure of 3p states in $^{25}Mg^+$ with an uncertainty, that is smaller than the transition linewidth $\Gamma/2\pi$ = 41.8 MHz and smaller than the 40 MHz uncertainty requested for the modeling of astronomical spectra [11]. Numerical values are listed in Table 4.3. The absolute frequency of the widely used $3s_{1/2}$(F=3)-$3p_{3/2}$(F=4) cycling transition reads for instance: 1 072 085 225 (19) MHz. This value is in agreement with a previous, less accurate measurement [2], as we will see in the next section.

Table 4.3.: $^{25}Mg^+$ transition frequencies between hyperfine structure centroids and hyperfine structure multiplets, evaluated using external input from [8, 111, 113, 114]. The uncertainties of the hyperfine corrections are assumed to be small against the 19 MHz uncertainties of the $^{25-24}Mg^+$ isotope shifts. All frequencies are given in MHz, transitions with $\Delta F = 2$ are not dipole allowed.

Centroid $^{25}Mg^+$ D_1 ($3s_{1/2}$-$3p_{1/2}$)	1 069 339 963 (19)
Centroid $^{25}Mg^+$ D_2 ($3s_{1/2}$-$3p_{3/2}$)	1 072 084 556 (19)
$3s_{1/2}(F=2)$-$3p_{1/2}(F=3)$	Centroid D_1 - 1171
$3s_{1/2}(F=2)$-$3p_{1/2}(F=2)$	Centroid D_1 - 865
$3s_{1/2}(F=3)$-$3p_{1/2}(F=3)$	Centroid D_1 + 618
$3s_{1/2}(F=3)$-$3p_{1/2}(F=2)$	Centroid D_1 + 923
$3s_{1/2}(F=2)$-$3p_{3/2}(F=4)$	Centroid D_2 - 1120
$3s_{1/2}(F=2)$-$3p_{3/2}(F=3)$	Centroid D_2 - 1026
$3s_{1/2}(F=2)$-$3p_{3/2}(F=2)$	Centroid D_2 - 980
$3s_{1/2}(F=2)$-$3p_{3/2}(F=1)$	Centroid D_2 - 960
$3s_{1/2}(F=3)$-$3p_{3/2}(F=4)$	Centroid D_2 + 669
$3s_{1/2}(F=3)$-$3p_{3/2}(F=3)$	Centroid D_2 + 763
$3s_{1/2}(F=3)$-$3p_{3/2}(F=2)$	Centroid D_2 + 809
$3s_{1/2}(F=3)$-$3p_{3/2}(F=1)$	Centroid D_2 + 828

4.7. Comparison to literature and impact of our measurements

The only isotopically resolved reference data available so far stood alone since 1980, when Drullinger and co-workers measured the D_2 line on a cloud of laser-cooled Mg^+ ions in a Penning trap [2]. The transition frequency of the $^{24}Mg^+$ component was measured against an iodine reference line with an uncertainty of 120 MHz and the $^{26-24}Mg^+$ isotope shift was measured to be 3050 (100) MHz all in agreement with our results (Tables 4.1, Figure 4.10). The $3s_{1/2}(F=3)$-$3p_{3/2}(F=4)$ cycling transition in $^{25}Mg^+$ was also observed. The frequency shift to the $^{26}Mg^+$ component was 772 (60) MHz, we find 797 (19) MHz from the considerations in the previous chapter.

Previously there was no isotopically resolved measurement for the D_1 line, but it was evident (Section 4.5) that the D_2 isotope shift is a fair approximation for the isotope shift of the D_1 line on the previous accuracy level of 100 MHz. This assumption was made in line shape models for unresolved Fourier transform (FT) measurements [103] and quasar absorption spectra [90].

Given the fact that Mg^+ ions were trapped by several groups over three decades, it surprises that the transition frequencies were never really measured on single ions. Early spectroscopic work on single Mg^+ ions was reported from the groups of

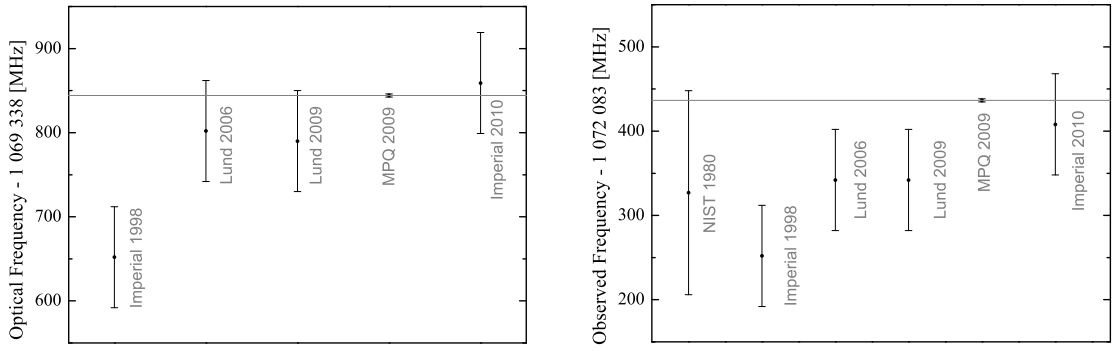

(a) Composite line center Mg^+ D_1 (b) Composite line center Mg^+ D_2

Figure 4.11.: Comparison of published transition frequencies for an isotopic composition of natural abundances. The NIST result was obtained by laser spectroscopy in a Penning trap [2], all other data was taken by UV Fourier transform spectroscopy using hollow cathode discharge lamps at Imperial College [20, 103] and Lund University [105, 106]. Common shifts in the transition frequencies of both fine-structure components indicate the presence of systematic effects in FT spectroscopy.

David Wineland in 1981 [3] and Hans Dehmelt in 1983 [4]. Both measurements were focused on the linewidth, while transition frequencies were not given. It is speculative if dipole-allowed transitions were 'perhaps not so interesting for high-resolution spectroscopy' [33] or if line-shape distortions [4] and the lack of a suitable frequency calibration scheme [5] prevented a measurement beyond the accuracy of [2].

The most accurate literature values for the D_1 and D_2 transition frequencies and fine-structure splittings originated from isotopically unresolved FT spectroscopy with hollow-cathode discharge lamps. An uncertainty of 60 MHz was reported when calibrated against (blue-visible) ArII lines [20, 103, 104, 105, 106]. In order to compare our isotopically resolved results to unresolved measurements we determine the center-of-gravity for a composition of natural isotope abundance (^{24}Mg: 78.99%, ^{25}Mg: 10%, ^{26}Mg: 11.01%) [117]. According to Landé's interval rule $\delta\nu^{25,24}$ represents the isotope shift between the center-of-gravity of the $^{25}Mg^+$ hyperfine structure multiplet and the $^{24}Mg^+$ component [118], so the center-of-gravity of the composite line is shifted by $0.1 \times \delta\nu^{25,24} + 0.1101 \times \delta\nu^{26,24}$ with respect to the $^{24}Mg^+$ transition frequency. For the center-of-gravity frequency we find $\nu_{cog}D_1 = 1\ 069\ 338\ 844.2\ (1.9)$ MHz and $\nu_{cog}D_2 = 1\ 072\ 083\ 436.4\ (1.9)$ MHz (Figure 4.11), the low natural abundance of ^{25}Mg reduces the uncertainty compared to the ^{25}Mg isotope shifts by a factor of 10 to 1.9 MHz.

Pickering and co-workers [103, 104] used isotope shifts and hyperfine constants reported in [2] for their line shape model fitted to the isotopically unresolved lines. While the $^{24}Mg^+$ transition frequencies deduced from their fits are in reasonable agreement with our measurements (Table 4.1), the transition frequencies given for

the composite lines deviate by 3 σ (Figure 4.11). In [103] the spacing between the ^{24}Mg components and the composite line centers were reported to be 378 MHz (D_1) and 360 MHz (D_2), where we find 501 MHz (D_1) and 502 MHz (D_2) from our measurement and 495 MHz from the D_2 measurement by Drullinger and co-workers [2]. This suggests that there is either an discrepancy in the definition of the composite line center or a systematic effect in the fit procedure of this FT analysis.
The authors of [20, 105, 106] neglect the isotopic substructure and fit a single Voigt profile to the fluorescence line. The published transition frequencies are in reasonable agreement with our center-of-gravity results (Figure 4.11). Still we think that this fitting procedure can introduce a systematic shift in the line center. This is of particular importance since Ruffoni and Pickering [20] recently used our measurement, together with further isotopically resolved and absolute frequency calibrated lines in neutral magnesium [70, 119], as an accurate 'magnesium wavenumber standard' for UV and VUV FT spectroscopy. Our measurement was also used for an adjustment of ArII calibration [120].
To quantify the systematic effect from the isotopic substructure we follow a bottom-up-approach: We create an artificial fluorescence profile by adding weighted Voigt profiles centered at their specific transition frequency (^{24}Mg, ^{26}Mg and ^{25}Mg HFS components). Then we fit a single Voigt profile to this artificial data-set. Afterwards we compare the fitted line center with our center-of-gravity result (Figure 4.12). We find that the fitted line centers systematically depend on the sample temperature. From the width of unresolved Mg lines we extract a lamp temperature of about 1800 K (Figure 3 in [20]) and find a 50 MHz deviation effect from our center-of-gravity results, which were used for calibration here. This systematic shift compares to an improved calibration uncertainty of 30 MHz reported for the transition frequencies for titanium lines measured against this magnesium wavenumber standard [20]. Though we are delighted that our data helps to reduce the calibration uncertainties in deep UV FT spectrometry we point out that the isotopic sub-structure may cause a significant calibration error here.
Finally we note that the $^{26-24}Mg^+$ isotope shift was recently measured by collinear laser spectroscopy on an ion beam [23], the result was 3076(2)(7) MHz for the D_1 line. Here our ion trap value serves as a benchmark test for a measurement on stable and short lived $^{21-32}$Mg isotopes and our data helped to resolve calibration issues in the acceleration voltage of the ISOLDE radioactive ion beam facility at CERN. This measurement is therefore not independent of our result.

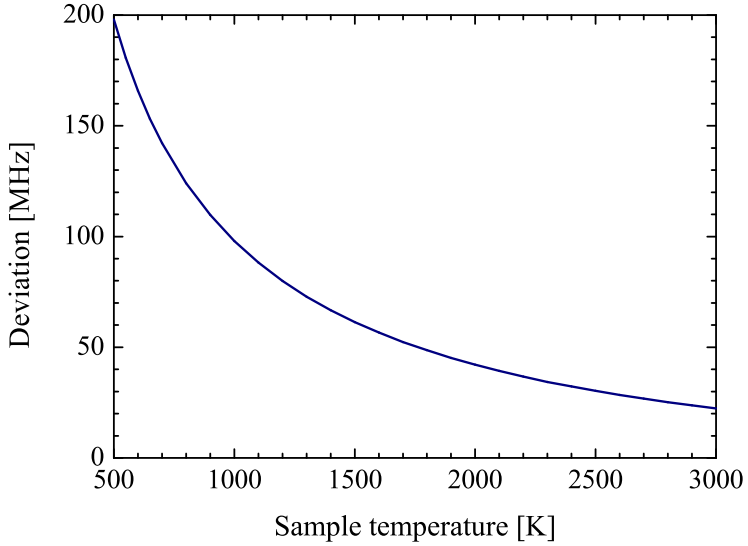

Figure 4.12.: Temperature dependence of the line center returned from single Voigt fits to a composite line of natural isotopic abundances due to the unresolved substructure (here shown for the D_1 line relative to our center-of-gravity result). The systematic dependence of the sample temperature, next to a possible calibration uncertainty, might be an explanation for the common shifts in Fourier transform spectroscopy (Figure 4.11). From Figure 3 in [20] we extract a typical sample temperature of about 1800 K, where we find a deviation of about 50 MHz.

4.8. Impact on many-multiplet analyses of quasar absorption spectra

Many-multiplet studies in the 'low' redshift region are mostly based on the frequency difference between Mg^+ 3s-3p transitions and Fe^+ lines between 234 nm and 260 nm (Figure 4.2). We estimate the required accuracy of laboratory reference data in many-multiplet studies from Equation 4.3, hereby we compare the frequency difference between Mg^+ ($q_{(\mathrm{Mg})} \approx 165$ cm^{-1}) and Fe^+ lines ($q_{(\mathrm{Fe})} \approx 1500$ cm^{-1}, see Figure 4.2).

$$\omega_{(\mathrm{Fe,z})} - \omega_{(\mathrm{Mg,z})} \approx \omega_{(\mathrm{Fe,lab})} - \omega_{(\mathrm{Mg,lab})} + 2(q_{(\mathrm{Fe})} - q_{(\mathrm{Mg})})\ \Delta\alpha \tag{4.8}$$

The fractional uncertainty in $\Delta\alpha$ in many-multiplet analyses is about 10^{-6} [92], which corresponds to a shift in this frequency difference of about 0.0027 cm^{-1} or 80 MHz. We conclude that the frequency difference between laboratory reference frequencies $\omega_{(\mathrm{Fe,lab})} - \omega_{(\mathrm{Mg,lab})}$ should be known to this precision or better (compare to Section 4.1).
The best measurements on the relevant Fe^+ transitions [11] originate from FT spectroscopy using discharge lamps [105, 106]. The measurement uncertainty of 60 MHz

is dominated by the wavenumber calibration against (blue-visible) ArII lines. Both, the Mg^+ and the Fe^+ lines were determined in the same apparatus. FT spectrometers are capable to measure large frequency differences relative to each other [20], which results in a suppression of possible calibration errors. Thus our more accurate absolute frequency measurement on Mg^+ might be less reliable for a comparison with Fe^+ lines in many-multiplet analyses, but we also identified a possible systematic effect due to the unresolved isotopic structure in Mg^+ (Figure 4.12). An absolute frequency measurement on the respective Fe^+ lines is therefore desirable[10].
Still, our isotope shift measurements can be directly used as input data for astrophysical line shape models. The $^{26-24}Mg^+$ isotope shift amounts to 3 GHz and different isotopic abundances can considerably influence the composite line. Knowledge about the isotope shift allows to fit both, the isotopic abundance and the fine-structure constant to match the astrophysical spectra [97]. A recent investigation used our data for the first measurement of magnesium isotope abundances at high redshifts [19].

4.9. Summary

In this chapter we described accurate measurements of the ^{24}Mg and ^{26}Mg components of the 3s-3p fine-structure doublet in Mg^+. From four absolute frequency measurements we deduce the corresponding isotope shifts and fine-structure splittings. The measurement accuracy exceeds previous results by more than two orders of magnitude and we resolve the isotope shift of the fine-structure splitting for the first time. We deduce transition frequencies for the ^{25}Mg hyperfine structure and the center-of-mass frequency of an isotope mixture of natural abundance. Our measurement may be regarded as exact reference for present and near future astrophysical spectra and for comparison with theoretical isotope shift predictions. Our data recently served for an improved wavenumber calibration for UV and VUV Fourier transform spectroscopy [20, 120], as a benchmark test for collinear spectroscopy on short lived Mg isotopes at CERN/ISOLDE [23] and for a measurement of isotope abundances at high redshifts [19].
Strong fluorescence is valuable for a variety of experiments and future applications might require an even more accurate calibration. The limiting systematic uncer-

[10] As a transition metal ion Fe^+ shows rich electronic level structure. An ion trap measurement based on quantum logic spectroscopy is envisaged in [14]. A more natural choice is fast beam laser spectroscopy since it meets the required precision and circumvents problems with pumping into dark states. The strongest line in Fe^+ is the $3d^64s$-$3d^64p$ transition at 41968 cm^{-1} ($\lambda =$ 238.2 nm) [11]. The transition connects the $J = 9/2$ ground state with a $J = 11/2$ upper state, all other possible decay channels require $\Delta J \geq 2$. Excitation with circular polarized light might result in an appreciable fluorescence signal from a large crystal of sympathetically cooled Fe^+ ions.

tainty of 160 kHz was caused by the rather broad frequency spectrum of our dye laser. Stabilization of the laser linewidth to an ultra-stable reference cavity can essentially remove this systematic effect. The statistical uncertainty of the $^{26}D_2$ line was only 14 kHz, indicating that our spectroscopy scheme should allow a further improvement of at least one order of magnitude. The error budget indicates no fundamental limit down to a measurement uncertainty of 1 kHz or better. Yet such a precision corresponds to $2.4 \cdot 10^{-5}\Gamma$ and would require long averaging times and a very cautious characterization of technical systematic effects with a duty cycle of weeks and months.

4.10. Outlook: Lifetime measurement

Apart from the transition frequency it is in particular important for the evaluation of astrophysical spectra to know the oscillator strength of a transition. The oscillator strength of a two-level atom is directly linked to the natural linewidth and thus to the upper state lifetime. The lifetime of the 3s-3p transitions in Mg^+ was therefore subject of a number of experimental and theoretical investigations (see [46] and References therein).

The well-controlled line shape of our spectroscopic experiments enables to extract the Gaussian and Lorentzian part of the Voigt profile from fits to the data, which corresponds to a measurement of the ion temperature and the upper-state lifetime in the frequency domain. A least square fit to a single, extensive line scan as shown in Figure 4.7 extracts the Lorentzian part of the spectrum with a statistical uncertainty of 800 kHz, which corresponds to about 2% of the natural linewidth Γ. The statistical uncertainty of a single measurement day is on a par with the best result from the literature (Figure 4.13), but the investigation of systematic effects turns out to be involved.

Spectroscopy method: The spectroscopy laser at different detunings induces only residual temperature variations (Figure 4.3). The resulting systematic deviation was investigated in Chapter 3.2 in [50]. It is smaller than 1 kHz for an intensity ratio between the spectroscopy laser and the cooling laser $r = S_{0,s}/S_{0,c} = 0.001$, which is typical for our experiments. The method has thus the potential to measure the Lorentzian part of the linewidth with a fractional uncertainty better than $10^{-4}\Gamma$. However we identified a number of technical systematic effects, which are larger and make a precise lifetime measurement more complicated.

Non-linear correlations: The Voigt-type fluorescence spectrum is a convolution of the Lorentzian natural linewidth and a Gaussian. The Gaussian part reflects the residual temperature of the ion and the (presumably) Gaussian laser spectrum. The main problem arises from a non-linear correlation of the Gaussian and the Lorentzian linewidth, which complicates the correct estimate of the Lorentzian linewidth from noisy data. For a quantification of the effect we investigated artificial sets of data.

Hereby we create many artificial Voigt profiles with known Lorentzian and Gaussian contributions and add Poissonian noise. Then we fit Voigt profiles to the noisy data and extract the Lorentzian part. When we average the data we observe a severe systematic deviation of up to 400 kHz from the initial Lorentzian contribution.
The non-linear correlations can be resolved with the following fitting procedure. We fix the Gaussian and the Lorentzian contribution within a certain range of parameters and fit only the offset, the amplitude and the line center of the Voigt profiles. This corresponds to a grid of fixed Gaussian and Lorentzian linewidths. At each grid point we run a least square fit to the whole available data set. We create a two-dimensional χ^2 landscape and extract the most likely minimum value. The maximum and the minimum Gaussian and Lorentzian contributions, which fulfill the condition $\chi^2 = \chi^2_{min} + 1$ define the statistical uncertainty. For artificial data sets representing typical experimental parameters we find agreement with the initial Lorentzian contribution within a statistical uncertainty of less than 20 kHz. A questionable assumption of this evaluation scheme is the constancy of the Gaussian contribution over the whole measurement period. We quantify the effect of a varying Gaussian contribution by adding access noise to the Gaussian linewidth and find a systematic deviation smaller than 50 kHz for reasonable assumptions. Thus we can control the uncertainty due to non-linear correlations on a level of 10^{-3} of the natural linewidth.
Detector non-linearities: Another complication arises from the non-linear response of our imaging photo-detector. The dead time characteristics of our single-photon camera shows an involved mixture of paralyzable, non-paralyzable and even position-dependent dead times. This results in a non-linearly reduced count rate and a Voigt fit will overestimate the Lorentzian part of the spectrum. For a peak count rate of 5 kHz, which is typical for our measurements, we found an overestimate of the Lorentzian linewidth of about 1 MHz. To correct for the non-linearities we simulated the camera dead time according to the specifications of the manufacturer. We create sets of photon arrival times assuming a Poissonian distribution and evaluate the count rate with respect to logic rejection criteria[11]. The manufacturer does

[11] Dead time characteristics according to the manufacturer: Two photons are detected within 400-500 ns. The camera will treat both events as single count with a position error. The position is encoded in X-Y voltages between 0.5 V and 4.5 V. Once the combined encoding voltage exceeds a discriminator level of 5 V both events are rejected. This leads to a position dependent dead time at high photon flux. When the second photon hits between 400-500 ns and 1 μs, both the first and second event are vetoed from processing. If the second photon hits in between 1 μs and 3.8 μs, the first count is valid, the second count is rejected. This dead time is paralyzable, i.e. another event in this timing window will extent the dead time by another 3.8 μs, which is owed to precise position readout. The last dead time applies when another photon hits in between 3.8 μs and 10 μs. This dead time is a property of the post-procession of the X-Y coordinates. The first count is valid, while the second count is rejected. This dead time is non-paralyzable, i.e. another event in this timing window will not extent this dead time by another 10 μs, but the aforementioned 3.8 μs paralyzable dead time applies.

not specify uncertainties associated with the dead times and we found in the laboratory that the non-linearities depend, e.g., on the acceleration voltage applied to the micro-channel plate of our single-photon camera. For simulated count rates we obtain good agreement of the non-linear response with a two-parameter correction function. This correction function is then fitted to measured count rates in the laboratory. From the maximum observed deviation from the fitted correction function we estimate a systematic uncertainty of 50 kHz due to falsely compensated detector non-linearities.

Further effects: The saturation parameter of the spectroscopy laser beam is typically set below $S_{0,s} = 0.001$ in our experiments, which corresponds to a saturation broadening of 20 kHz (Equation 2.16).

The presence of a magnetic field will split the magnetic sublevels according to the Zeeman effect, which results in a broadening of the line when multiple sublevels contribute to the fluorescence. A dedicated lifetime measurement will therefore employ circular polarized laser light resonant to the $3s_{1/2}$-$3p_{3/2}$ transition[12], hereby we are confident to control the influence of magnetic fields on a level of 20 kHz.

A Lorentzian contribution to the laser line-width will result in a deviation of the lifetime measurement. The fiber-laser system is now stabilized to a reference cavity via a transfer diode laser (see Chapter 2.2.3. in [56]). From the in-loop beat note between the fiber laser and the diode laser we estimate a laser linewidth <60 kHz in the IR, which corresponds to <240 kHz in the UV regime. The Schawlow-Townes linewidth of our fiber-laser is considerably smaller than 60 kHz and we expect a predominantly Gaussian laser spectrum due to technical excess noise. An investigation of the beat signal between the diode laser and the fiber laser did not reveal a significant Lorentzian contribution to the linewidth, but the noise pedestal introduced by the diode laser hindered ultimate conclusions. Thus residual non-Gaussian contributions to the linewidth remain an issue.

Preliminary result: Figure 4.13 compares previous literature measurements with our work. Our data represents a re-evaluation of all available data of our line center measurement and few additional data points recorded with the stabilized fiber laser. From our data we find a weighted average linewidth of 42.26 MHz with a statistical uncertainty of 0.15 MHz, which correspond to a lifetime of 3.766(13) ns and a fractional uncertainty of $3.5{\cdot}10^{-4}$, but non-statistical scatter clearly indicates the presence of systematic effects. Most of the data was measured with our spectrally broad dye laser (Section 3.1.6), moreover we evaluate existing data and it is difficult to investigate the influences of different laboratory conditions in the aftermath. With the remark that systematic effects require further investigation we conservatively assume a systematic uncertainty of 1 MHz, the preliminary result is then $\Gamma/2\pi = 42.3(1.0)$ MHz or $\tau = 3.77(9)$ ns.

[12] Also: Only the $3s_{1/2}$-$3p_{3/2}$ transition lies within the frequency range of our narrow-band fiber laser.

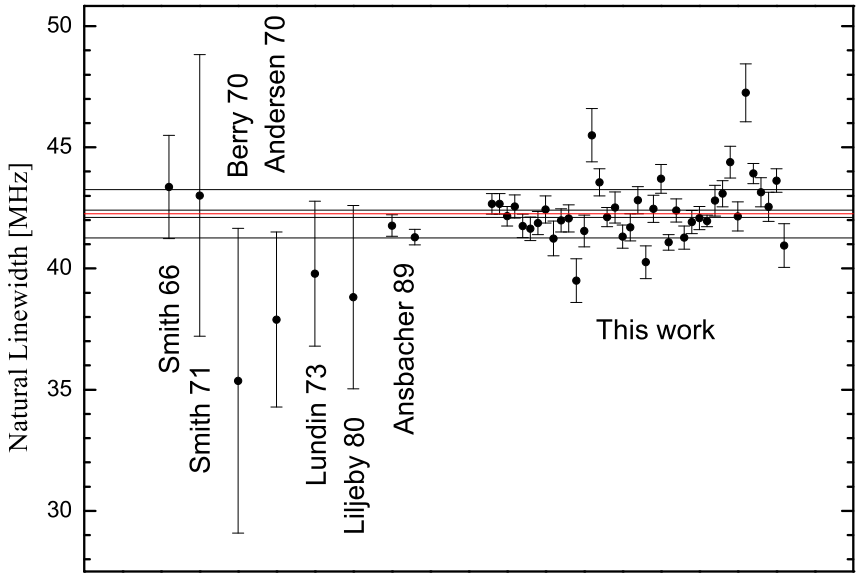

Figure 4.13.: Experimental values for 3s-3p lifetimes in Mg^+, here converted to the natural linewidth $\Gamma/2\pi$. Our data is binned into measurement days. The statistical uncertainty of a single measurement day is on a par with the uncertainty of the beam-laser measurements by Ansbacher and co-workers [46] and considerably smaller than the uncertainty of Hanle (Smith 66 [123]), phase (Smith 71 [124]) and beam-foil measurements (Berry [125], Andersen [126], Lundin [127], Liljeby [128]). Yet we suffer from non-statistical scatter, which indicates the presence of unidentified systematic effects. The red line is the weighted mean linewidth of our measurement, inner black lines represent the statistical uncertainty, outer black lines represent an estimate of a 1 MHz systematic uncertainty.

Outlook: A lifetime measurement on an uncertainty level of 1% (400 kHz) seems reasonable with our current experimental setup. The most accurate lifetime measurements on dipole-allowed transitions in trapped ions are performed in the time domain. A single trapped ion is excited with a short laser-pulse and the arrival times of the flourescence photons are recorded with a fast photo-multiplier. Lifetimes of dipole-allowed transitions were measured in single Cd^+ [121] and Yb^+ [122] ions, with fractional uncertainties of $3.5{\cdot}10^{-4}$ and $2.5{\cdot}10^{-4}$, respectively. At a corresponding uncertainty level of 100 kHz we face a number of technical systematic effects, yet it might be possible to perform a lifetime measurement at comparable precision in the frequency domain.

5. A single trapped-ion oscillator

In this chapter we review our opto-mechanical experiments with a single-ion oscillator. We investigated large amplitude oscillations of a single ion driven by blue-detuned laser light and observe analogies to optical lasers [24]. Additionally we studied injection locking to an external signal [25]. The subject was presented in the theses of Maximilian Herrmann [50] and Sebastian Knünz [56], here we give an illustrated overview. We follow a chronological path spanning from a subtlety observed in our spectroscopy work to the detection of ultra-weak forces by phase synchronization of the ion oscillator with a weak external signal.

5.1. From chain spectroscopy to single oscillating ions

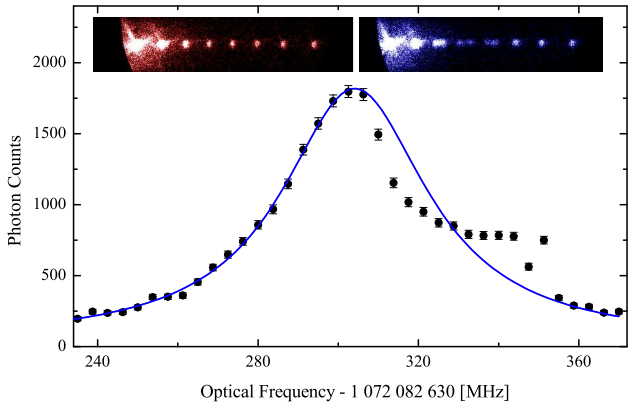

Figure 5.1.: Spectroscopic lineshape for center ions at insufficient damping, compare to our spectroscopy method in Figure 4.4. Typical pictures of ion chains are shown above the line scan. Ions addressed by the cooling laser appear bright, center ions are cooled at red detunings of the spectroscopy laser (left). Oscillating center ions are observed at certain values of blue detuning (right). The discontinuous feature at about 350 MHz gave an early hint on bi-stability in the system (compare Chapter 4 in [50]).

The spectroscopy method described in Section 4.2, employs two laser beams resonant to the same dipole-allowed transition in Mg^+ ions. One laser is red-detuned and damps the ion motion in the trap potential via Doppler cooling. The second laser scans over the resonance and is at times blue-detuned. A blue-detuned laser

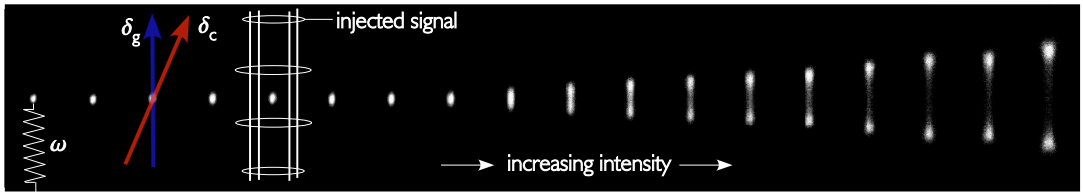

Figure 5.2.: This sequence of images shows a single trapped ion addressed by a constant red-detuned and a blue-detuned laser beam with incrementally increasing intensity. The threshold to oscillatory operation is visible. Above threshold we observe bright turning points, which indicate steady state oscillation. Overlayed sketches depict our experimental setup. The spring on the left symbolizes the axial trap potential with characteristic frequency ω. Resonant laser beams at detunings $\delta_{c,g}$ damp and drive axial motion, the red-detuned cooling beam has a finite projection on all trap axes to also cool radial motion. The strength of the axial potential is set by an enclosing DC voltage applied to the inner rings of our four-rod linear ion trap (Section 3.2.3). For injection locking experiments we apply an additional RF signal to one outer ring electrode (Figure 3.6). (This sequence was taken in the linear endcap trap, Section 3.2.2).

has the opposite effect on the ion's velocity: a scattering event is more likely when the ion moves in the propagating direction of the laser beam, thus a blue-detuned laser amplifies an existing motion.
For insufficient cooling we observed oscillating ions in the center of a short ion chain, while Doppler cooled ions at one end of the chain and ions located at the opposite end remained 'cool' (Figure 5.1). We learned that this surprising feature was due to certain axial oscillation eigenmodes of the chain, which were driven above their particular oscillation threshold.
Kerry Vahala, who joined our team for a sabbatical, suspected a non-linear, parametric behaviour and suggested to look for an oscillation threshold. We repeated the experiment with a single ion simultaneously addressed by a red-detuned and a blue-detuned laser. Again we restrict the treatment to the axial direction of our linear trap (see the beam geometry in Figure 5.2). The red-detuned laser was kept at constant intensity and constant detuning $\delta_c/2\pi \approx -70$ MHz ($\approx 1.7\,\Gamma$) to prevent immediate ion loss. We superimposed a weaker blue-detuned laser at $\delta_g/2\pi \approx 30$ MHz. As we increased the intensity of the blue-detuned laser beam we observed a large scale oscillation of the ion along the trap axis (Figure 5.2). The oscillations set in at an apparent threshold intensity and we measured oscillation amplitudes up to 100 μm. This marked the beginning of a series of theoretical and experimental investigations of this simple, yet feature rich system.

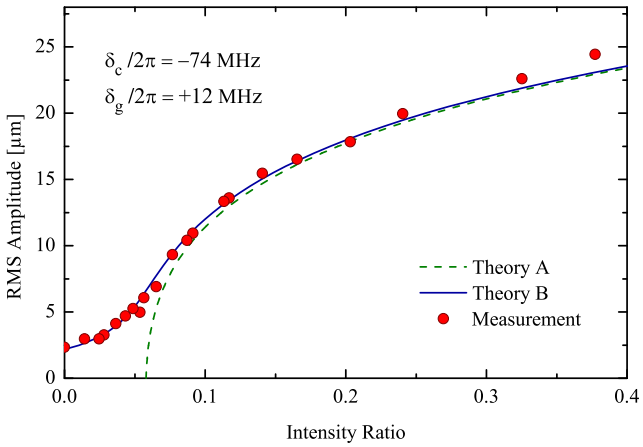

Figure 5.3.: Root-mean-square amplitudes of the ion oscillator as a function of the intensity ratio between the blue- and red-detuned laser ($\delta_c/2\pi = -74$ MHz and $\delta_g/2\pi = 12$ MHz). Theory A and B correspond to solutions of Equations 2 and 3 in [24]. Theory A shows a sharp threshold (dashed line). The threshold is less pronounced in theory B since it includes spontaneous emission.

5.2. A trapped-ion phonon laser

A trapped ion in ultra high vacuum is decoupled from its environment to a great extent. Damping and amplification of the ion's motion is dominated by the interaction with the near-resonant (red- and blue-detuned) laser beams and can be described by including blue detunings into the well-known framework of Doppler cooling [43, 51]. The oscillation frequency is a property of the trap and it is defined by the axial electrostatic potential. Thus, most features of the ion oscillator are well controlled and can be independently chosen within a large range of parameters. We can, e.g., freely select the damping and therefore the quality-factor of the oscillator by setting cooling laser parameters. A single atom is a delicate object, yet we obtain in-vivo information about the undisturbed system from fluorescence photons, which are inherent to the oscillation process. The conjunction of all these features enables good agreement between the data and ab initio descriptions (Figure 5.3).
Two different theoretical approaches were developed by Kerry Vahala and Maximilian Herrmann. The latter, more intuitive treatment, identifies stable operation points based on the power balance of a laser-driven classical ion oscillator in steady-state [50]. It explains why the ion is not just expelled from the trap center when the 'gain' of the blue-detuned laser overcomes the cooling power: The detunings are modulated during an oscillation cycle due to the Doppler effect, so the corresponding cycle-averaged scattering rates of both laser beams depend on the oscillation amplitude. In particular the gain saturates towards large oscillation amplitudes and

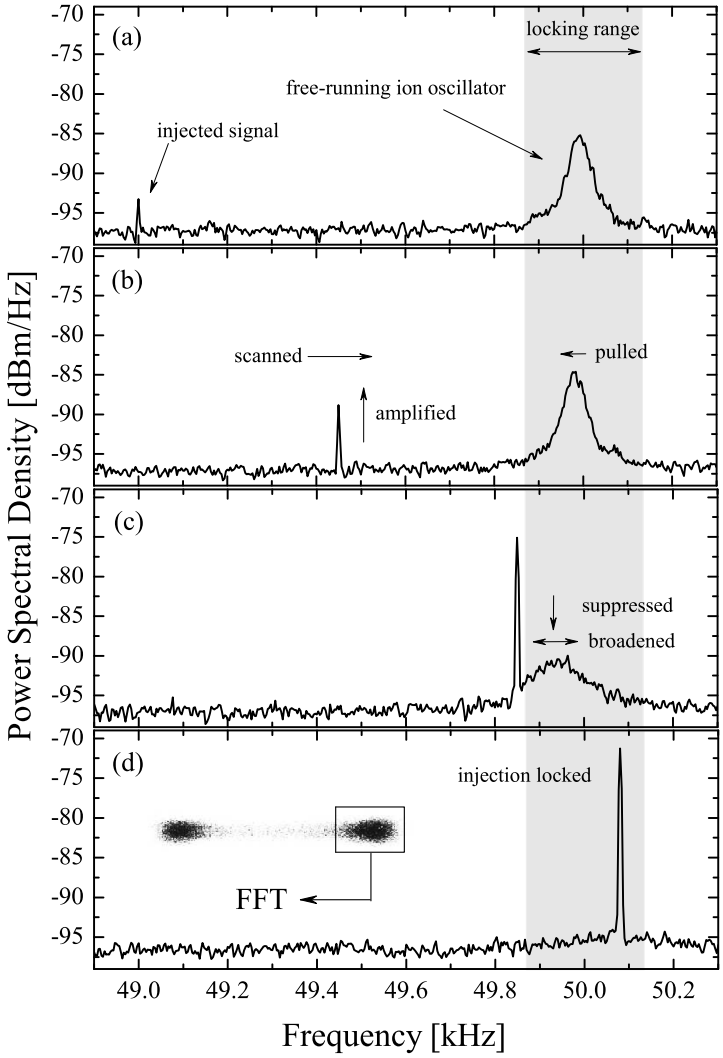

Figure 5.4.: Motional spectrum of a laser-driven oscillating ion in the presence of a weak external signal for different detunings of the external signal with respect to the free running oscillation frequency. The cartoon in sub-figure (d) depicts the experimental method: We observe the oscillating ion, record modulated photon signals from a chosen spatial origin around one of the turning points and obtain the spectra via Fourier analysis. (a) Essentially free-running oscillation, a modulation by the external signal at large detuning is visible. (b) The injected signal is amplified by the oscillator as the detuning decreases, the free-running oscillation frequency gets pulled towards the injected signal. (c) Amplification and frequency pulling are increasingly pronounced, the linewidth of the free-running part is significantly broader, as it is suppressed towards its oscillation threshold (note the logarithmic scale). (d) Injection locking. The oscillation frequency is governed by the external signal and the linewidth is smaller than the 5 Hz resolution limit of our FFT device.

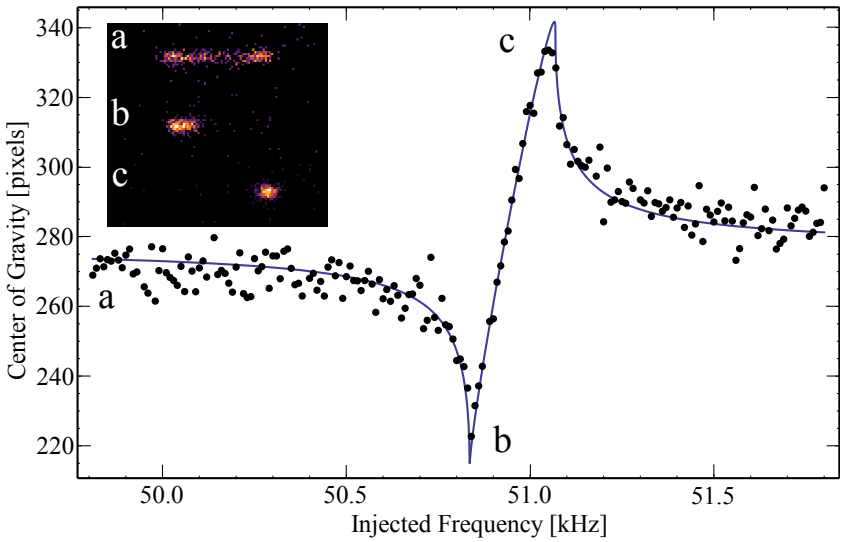

Figure 5.5.: Phase between the external drive signal and the ion oscillator. We gate our camera with the injected signal and extract the phase from the center-of-gravity of stroboscopic images, as illustrated in the inset. The data points were recorded in randomized order. The solid line is a fit to a numerical solution of the Adler equation [129]. Inside the locking range the stroboscopic image of the oscillatory pattern collapses to a spot (positions b,c) and we observe a π phase shift of the constant phase lag between the injected signal and the oscillator. Outside the locking range we observe pulling of the time-averaged phase. The slight asymmetry is due to an uncompensated time delay in our electronics.

stable operation points are found at defined oscillation amplitudes[1]. A quantized treatment shows that the amplification process arises from stimulated generation of phonons, thus the system can be considered as a phonon laser [24]. Here, the term 'phonon' is associated with the quantized vibrational excitation in the axial trap potential. The ion oscillator exhibits further, macroscopic features known from optical laser oscillators, such as gain saturation, a threshold between thermal and oscillatory operation, and a Schawlow-Townes like behavior of the above-threshold linewidth of its motional spectrum [25].

5.3. Injection locking and force detection

To deepen the analogy to optical lasers we demonstrated injection locking of the system. The steady state operation of oscillators is based on a balance of gain and losses. The presence of a gain mechanism, in our case established by the blue-detuned laser, enables the amplification of weak oscillatory signals close to the free-running

[1]This argument holds true for $|\delta_c| > |\delta_g|$ and a certain range of intensity ratios [50].

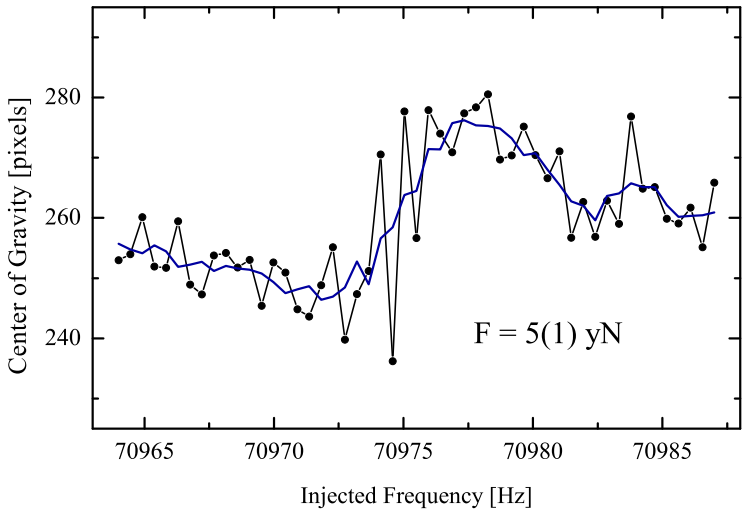

Figure 5.6.: Footprint of synchronization with a weak external signal at $\omega_{ax}/2\pi =$ 71 kHz. Here, the blue line is a smoothened average to guide the eye. The applied voltage corresponds to a driving force of 5(1) yN amplitude.

oscillation frequency. We introduce such an 'injected' RF signal[2] with an additional electrode (Figure 5.2). The weak oscillation induced by the injected signal is amplified and the free-running oscillation is suppressed due to gain competition. The free-running oscillation ultimately drops below threshold and the oscillator is injection locked to the external source [25].
For an experimental investigation we utilize the excellent timing resolution of our single photon camera (Section 3.4.3). We electronically restrict the field of view to a turning point of the oscillation. The ion appears periodically and a Fourier analysis of the modulated fluorescence signal reveals the oscillator's motional frequency spectrum (Figure 5.4). We observe characteristic features which are expected from injection locking theory, such as amplification of the external signal and frequency pulling as the injected signal approaches the locking range. The ion's motion follows the drive signal inside the locking range and the linewidth of the oscillator is presumably given by the linewidth of the injected signal (detection limited).
Insight in the phase behavior was obtained from stroboscopic images (Inset of Figure 5.5). Here we gated our camera with a phase window of the injected signal and observe only fluorescence photons in coincidence with a specific phase interval of the oscillation cycle. A closer investigation of stroboscopic images enabled a striking view on the phase behavior in- and outside the locking range (Figure 5.5). We find good agreement with the Adler equation, a differential equation which describes the

[2]We also observed synchronization with amplitude modulated laser beams. However, a constantly driven oscillator locked to an external signal is a cleaner demonstration of injection locking principles.

phase between the injected signal and the oscillator [25, 129].
Trapped ions represent lightweight oscillators cooled to mK temperatures. Their application as sensitive detectors for oscillatory forces was recently proposed [130] and a related experimental demonstration on Be^+ ions in a Penning trap resulted in a smallest detected force of 170 yN (yocto = 10^{-24}) [131]. For calibration of the electric force which acts on our ion we apply a static electric field (U = 1 kV) to the signal electrode and measure the resulting displacement in the trap potential. We obtained phase synchronization footprints for oscillatory driving forces as small as 5(1) yN (Figure 5.6), which corresponds to a displacement of only 1.5 nm in an axial potential with secular frequency $\omega_{ax}/2\pi = 71$ kHz. At $\omega_{ax}/2\pi = 111$ kHz we detected forces, which correspond to sub-nanometer displacements (0.7 nm). A comparison with the 3000 times larger thermal distribution at Doppler cooling temperatures and a 80 times larger extent of the ground state wave function of $^{24}Mg^+$ illustrates the sensitivity of our phase-detection scheme. A possible application might be the detection of weak forces acting on other atomic scale systems. In [25] we proposed the detection of periodically driven nuclear spin-flips in single, co-stored ions. The modulated magnetic moment can induce detectable oscillatory forces on the order of 10 yN in an inhomogeneous magnetic field with a gradient of 200 T/m [56].

6. Further prospects

This chapter describes possible prospects of our ion trapping project. Section 6.1 reports on progress with a fiber-based cooling laser system for Be^+ ions. Be^+ is the lightest ion with a convenient cooling transition. It is therefore the superior coolant ion for proposed spectroscopic experiments on He^+ [53] and Li^+ ions [63], moreover beryllium itself shows accessible transitions of fundamental interest. In Section 6.2 we propose a dual frequency trap which is supposed to store heavy ionic species together with light atomic ions. Sympathetic cooling in such a dual trap might provide a broad range of molecular ions at mK temperatures. Finally we propose a spectroscopic experiment with a full repetition rate frequency comb at deep UV wavelengths. High harmonic generation [132] in gas jets is a well-known process for the generation of ultra-short wavelengths. Frequency combs are a promising approach to extend precision spectroscopy into a new wavelength regime [133, 134], but a demonstration experiment is still pending. In Section 6.3 we show that spectroscopy of dipole-allowed transitions in trapped ions might produce reasonable signal rates from state-of-the-art frequency comb sources.

6.1. A cooling laser system for beryllium ions

The initial objective of our ion trap group was preparatory work towards spectroscopy of the 1s-2s transition in $^4He^+$ [53]. $^4He^+$ itself has no suitable cooling transition, therefore we intend to cool sympathetically and require a co-stored ion species as coolant. At an early stage of this thesis we tried to produce two-species Coulomb crystals containing $^4He^+$ and laser cooled $^{24}Mg^+$ ions. Here we did not obtain conclusive evidence for the presence of sympathetically cooled $^4He^+$ ions, for the particular experimental conditions in our six-rod trap (Section 3.2.1).
The dynamics of a charged particle in a RF trap depends on its charge-to-mass ratio (Section 2.1.1). The lowest order stability region contains the case of vanishing confinement, therefore there is no hard theoretical limit for the charge-to-mass ratio difference of co-stored ions. A similar behavior applies for sympathetic cooling. Molecular dynamics simulations [135, 136, 137, 138] revealed a lower bound on the mass of singly charged particles that can be sympathetically cooled by a heavier species (Figure 6.1). This bound depends on the trap parameters and the involved particle numbers [136].
The scheme for 1s-2s spectroscopy in $^4He^+$ as envisaged in [53] relies on destructive

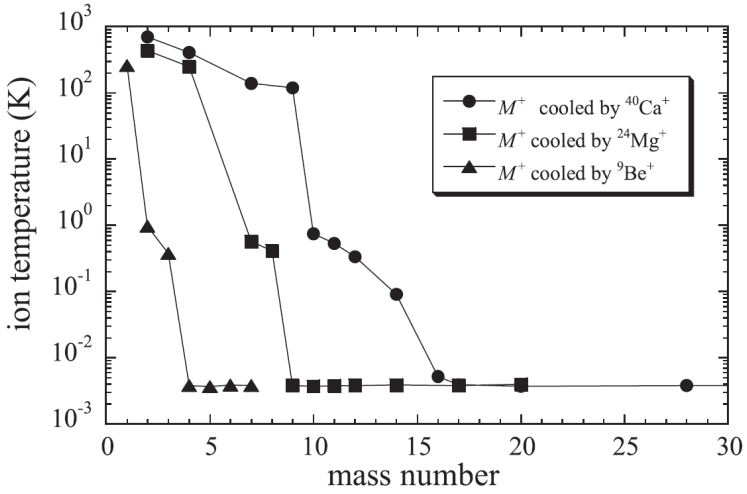

Figure 6.1.: Molecular dynamics simulation of sympathetic cooling of light ion species from [138]. The simulation is for 20 light mass M^+ ions and 60 heavier coolant ions ($^9Be^+$,$^{24}Mg^+$,$^{40}Ca^+$). The q parameter is set to 0.078 for each coolant species, while the trap is operated at a common drive frequency $\Omega/2\pi = 5.65$ MHz. Sympathetic cooling of $^4He^+$ ions to mK temperatures is only observed with $^9Be^+$ ions for this specific choice of parameters.

ionization detection and therefore requires frequent reloading. In particular, this proposal involves the storage of many $^4He^+$ ions in a reservoir, reliable ion transport in a segmented trap and finally storage of the naked $^4He^{2+}$ nucleus for readout. We expect that $^9Be^+$ as lightest ion with a suitable cooling transition will simplify the experimental realization of each step, since we increase the available parameter space with a coolant ion of more favorable charge-to-mass ratio.
The choice of $^{24}Mg^+$ was motivated by the availability of a much more convenient cooling laser system at the time the decision was made [58]. Meanwhile fiber laser systems are available for laser cooling of $^9Be^+$ ions, as we demonstrate here. The cooling laser system for $^9Be^+$ is more complex, since it incorporates two fiber lasers and the generation of a repumper sideband. Still we think that advantages on the trap side justify the manageable extra work on the laser systems.

Laser system - overview

Light resonant to the 2s-2p transitions at 313 nm is required for laser cooling of Be^+ ions. In a first step we create a laser beam at 626 nm by sum frequency generation (SFG) with two fiber lasers at 1050 nm and 1550 nm. This approach was pioneered in the group of David Wineland and Dietrich Leibfried at NIST [139]. Both wavelengths are close to the gain maximum of ytterbium and erbium doped fiber lasers respectively, so high power lasers are available and we hope for reliable turn-

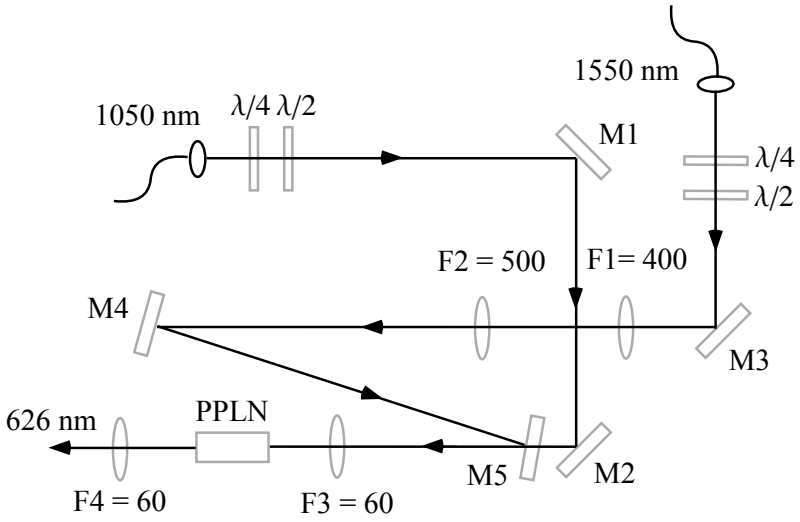

Figure 6.2.: Sum frequency generation. Two fiber lasers at 1050 nm and 1550 nm are overlapped and focused into PPLN material to generate light at 626 nm. A combination of quarter and half-wave-plates ($\lambda/4, \lambda/2$) adjusts the required linear polarization in each beam. All free space distances and lens positions where optimized by Gaussian beam propagation in order to achieve good spatial overlap and a near optimum confocal parameter within the PPLN crystal. All lenses are mounted onto translational stages for fine adjustments with respect to the output power at 626 nm. Distances are: Output facet 1050 nm - F3: 481 mm, Output facet 1550 nm - F1: 164 mm, F1-F2: 72 mm, F2-F3: 516 mm. M1-M4 are dielectric mirrors with high reflectivity for the respective wavelengths. M5 is a dichroic mirror, which is highly reflective for 1550 nm and anti-reflection coated for 1050 nm. The distance between the focusing lens F3 and the PPLN surface is about 54 mm. Another 60 mm lens behind the crystal is used for mode-matching into the subsequent frequency doubling unit.

key operation. High power levels at the fundamental wavelengths enable single pass SFG in a bulk PPLN structure. The advantages of a single pass process are superior intensity stability and the absence of a cavity and locking electronics. Once set up and adjusted we expect several 100 mW of red light at 626 nm in a maintenance-free manner. The light at 626 nm is then resonantly frequency doubled in a BBO crystal to obtain 313 nm.

Sum frequency generation

The fundamental light is produced by two commercial fiber lasers at 1050 nm and 1550 nm (Menlo Systems). Both lasers are specified to deliver up to 5 W of single-frequency radiation with a linewidth smaller than 70 kHz. Like the fiber laser for

Mg^+ cooling (Section 3.1.1), they incorporate a DFB fiber laser oscillator and amplifiers made from polarization independent fiber. Both lasers are tuned by a temperature change of the oscillator and have a piezoelectric actuator for fine-adjustment and feedback. The 2p fine-structure splitting in Be^+ is 197 GHz and both 2s-2p transitions can be reached with this laser system. The laser beams are overlapped and sent into a 40 mm long congruently grown lithium niobate chip (Stratophase). The chip has three periodically poled gratings with periods 10.90 μm, 10.95 μm and 11.00 μm and 0.5×0.5 mm^2 aperture. The phase matching temperature is about 178°C for the 10.95 μm grating.
In the case of second harmonic generation and non-critical phase-matching Boyd and Kleinman give a condition for optimum focusing $b = 2.84/L$ [140], where b is the confocal parameter in the material and L is the length of the crystal. Second harmonic generation is a special case of sum frequency generation with degenerate input frequencies. We took the optimum focusing condition for second harmonic generation of the mean wavelength as starting point for an optimization process with respect to the red output power.
The beam parameters after both fiber collimators were measured with the knife-edge method. We assume Gaussian beam propagation and extract minimal beam waists from fits to the data. For the ytterbium laser we obtained $w_{0,1050} = 385$ μm in 136 mm distance behind the collimator facet and for the erbium laser $w_{0,1550} = 223$ μm in 7 mm distance behind the collimator. From Gaussian beam propagation we determine free-space distances and positions for lenses with standard focal length for mode matching. We approximately match the optimum focusing condition for the 1050 nm beam with a single $f = 60$ mm lens, then we place a dedicated telescope in the 1550 nm beam path and adjust the overlap of both beams, which are combined by a dichroic mirror (Figure 6.2).
Two special features of the design are due to the use of standard mirrors. We combine the beam directly in front of the crystal, since dielectric standard mirrors with high reflectivity for both fundamental wavelengths were not available, metallic mirrors introduce losses and are suspected to cause wavefront distortions at high intensities. Second we use a dichroic mirror which was designed for a different application at 0° incidence. At 1550 nm we measured no significant transmission up to incidence angles of 15°, the angle dependence of the anti-reflection coatings at 1050 nm is less pronounced. In the current setup we use the mirror at an incidence angle of 10°. At a combined fundamental laser power of about 10 W from both fiber lasers, we demonstrated up to 2.16 W optical power at 626 nm, which is far beyond our requirement.

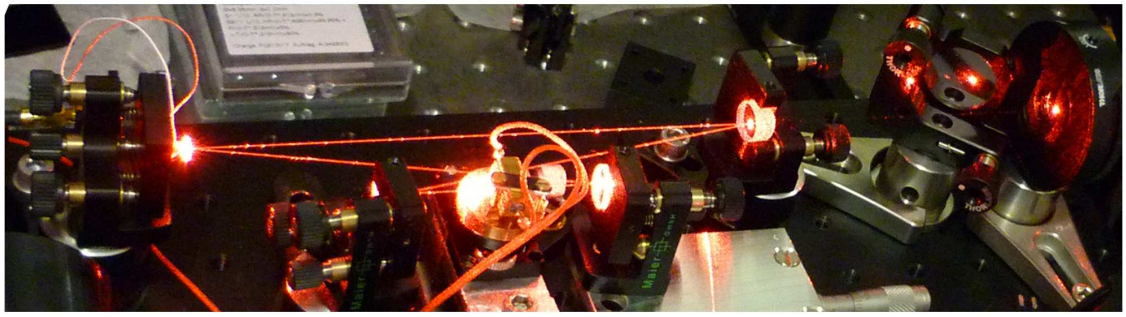

Figure 6.3.: Resonant second harmonic generation. The laser beam at 626 nm enters the bow-tie resonator through the upper right (flat) mirror, the enhanced TEM_{00} mode inside the cavity is clearly visible. A 8 mm long BBO crystal resides in a heated mount between two focusing mirrors (short arm). UV light at 313 nm leaves through the left focusing mirror. The small upper left mirror (flat) is glued on a piezoelectric actuator and keeps the cavity on resonance.

SHG stage

For frequency doubling we use a home-built enhancement cavity in a bow-tie configuration and stabilize the resonator length with the Hänsch-Couillaud method [60]. The design is similar to the 560 nm → 280 nm SHG stage of the Mg^+ laser system (Section 3.1.2). The crystal is a critically phase-matched 8 mm long BBO crystal, it is rectangularly cut and anti-reflection coated. The crystal is heated to about 50°C to prevent moisture absorption. The reason why we did not choose a Brewster cut crystal is that our particular optical table is not equipped with a 'flow box'. We clean the cavity mirrors of the Mg^+ SHG stage every 2-3 days to maintain a decent enhancement. BBO is hygroscopic, surface cleaning of a Brewster-cut BBO crystal is therefore delicate and the AR coating acts as a protective layer here. We also revised the oven design such that the AR coated crystal surfaces are accessible for cleaning.
The analytic optimization of the confocal parameter for critically phase-matched second-harmonic generation is involved, we use a numerical approximation given in [141]. The case of resonant SHG is treated in [142], in theory all fundamental light can be converted to UV light in a loss-less resonator, given perfect mode matching and perfect impedance matching at a defined reflectivity of the incoupling mirror. When we introduce absorption losses in the crystal we obtain nearly complete conversion in the limit of vanishing crystal length. Once we introduce an artificial round trip loss, we can evaluate the optimum crystal length and incoupling mirror reflectivity for a certain input power. Since we aim at reliable day-to-day performance we conservatively assume an additional round trip loss of about 1% and find good conversion for an 8 mm long BBO crystal. Impedance matching is then achieved for an incoupling mirror reflectivity of 97.8% at 1 W fundamental power.

We acquired mirrors with reflectivity 97.5%, 98%, 98.5%. The optimum confocal parameter ($b = 5.77$ mm) is fixed by the chosen crystal length and we try to match the confocal parameter in the focussing arm of the bow-tie resonator by ABCD matrix formalism. The folding angles of the focusing mirrors (curvature: $R = 50$ mm) of the bow-tie resonator necessarily introduce astigmatism, which limits the geometric overlap of the input beam with the resonant mode. We try to minimize this effect and decrease the folding angles to a practical minimum of 6°. We demonstrated 580 mW UV light at 313 nm generated from 1.58 W fundamental power at 626 nm.

Implementation

The $2s_{1/2}$-$2p_{3/2}$ transition at 313 nm in Be^+ has a linewidth of $\Gamma/2\pi = 18$ MHz, which corresponds to a saturation intensity of 765 W/m^2. A power level of 580 mW of our laser system is considerably higher than the few mW needed for Doppler cooling applications. With this power margin we will reduce the fundamental power levels to limit stress on components and we may also tolerate losses in the further beam path. We need to generate a re-pumper sideband to bridge the ground state hyperfine splitting of 1.25 GHz [143]. Following the NIST approach we will center the cooling laser frequency in between the hyperfine splitting, split the beam and employ two double-pass AOM setups at 312.5 MHz to create the desired laser frequencies. We then plan to recombine the beams in a single mode fiber, which is available at 313 nm wavelengths and ensures superior spatial overlap and good beam profile.

Experiments with Be^+ ions

We are mainly interested in Be^+ as superb coolant ion for precision spectroscopy of fundamental atomic systems like He^+ and $^*Li^+$. But Be^+ itself is a few-electron system of fundamental interest, too. Numeric ab-initio calculations of transition frequencies [7] reveal meaningful information of the nuclear charge radius from precision spectroscopy, which enables studies of the short-lived halo nucleus ^{11}Be. A recent measurement on a fast ion beam at CERN [144] is not consistent with an unpublished measurement at RIKEN. A benchmark measurement on the ^{9}Be 2s-2p transition frequencies, similar to the spectroscopy in Chapter 4, would help to identify possible systematic deviations[1].
In Section 6.3 we propose a measurement scheme of the 2s-3p transition in Be^+ at 103.9 nm, here we could compare a frequency measurement at challenging wavelength with ab initio calculations.

[1] W. Nörtershäuser, private communication

Table 6.1.: Comparison of dipole-allowed transitions between the metastable 2^3S_1 - $2^3P_{0,1,2}$ triplet states in helium-like Li^+ and Be^{2+}. Transitions wavelengths and linewidths are taken from the NIST atomic spectra database. Theoretical and experimental results for the fine-structure intervals (FS) are adopted from Table III in [6] and converted to MHz.

	Li^+	Be^{2+}
Wavelength 2^3S_1 - 2^3P_l	548 nm	372 nm
Linewidth 2^3S_1 - 2^3P_l	3.6 MHz	5.4 MHz
Lifetime 2^3S_1 [145]	49 s	1.8 s
2^3P_0-2^3P_1 FS theory [6]	155 704.584 (48) MHz	346 492.81 (99) MHz
2^3P_0-2^3P_1 FS exp.	155 704.27 (66) MHz [146]	346 518 (15) MHz [147]
2^3P_0-2^3P_2 FS theory [6]	93 025.266 (34) MHz	-99 970.68 (30) MHz
2^3P_0-2^3P_2 FS exp.	93 025.86 (61) MHz [146]	-100 023 (15) MHz [147]

The mass ratio of $^4He^+$ to $^9Be^+$ is similar to the mass ratio between $^9Be^+$ and $^{24}Mg^+$ so we may simulate important steps of the planned 1s-2s experiment in $^4He^+$ using two ionic species, which can be monitored and manipulated with resonant laser beams. In principle we could even simulate the frequency comb spectroscopy itself, ionizing two-photon transitions in Mg^+ or Be^+ are available at convenient or extreme UV wavelengths.

^{10}Be

^{9}Be is the only stable beryllium isotope. ^{10}Be is quasi-stable and has a half life of 1.5 million years. It naturally occurs in traces and is, e.g., used to study solar activity from arctic ice samples. ^{10}Be shows no nuclear magnetic moment and is therefore free of hyperfine-structure. We could obtain a macroscopic sample of 950 mg with slightly enriched ^{10}Be content from reflector elements of the former research reactor FRM I on campus[2]. The ^{10}Be/^{9}Be ratio in this sample is $4(4) \cdot 10^{-6}$ only and it remains to be shown, if we can predominately load $^{10}Be^+$ using mass selective properties of quadrupole RF traps and isotope selective photo-ionization techniques[3]. If it is possible to load this rare species, we may perform interesting measurements. A $^{10-9}Be^+$ isotope shift measurement can serve as benchmark test for the mentioned isotope shift investigations on short lived Be-Halo nuclei [144].
A more fundamental measurement may be carried out in $^{10}Be^{2+}$. Precise spectroscopy of the fine-structure in metastable helium is a candidate for the determination of the fine-structure constant α [149]. The evaluation of α requires theoretical

[2] Jörg Gerhard, private communication

[3] The isotope shift on the 234.8 nm photo-ionization transition amounts to 8.8 GHz [148], the Doppler broadening at room temperature is 5.3 GHz

input from bound-state QED calculations [6] and the estimate of neglected higher-order corrections sets the current uncertainty limit [149]. Upper bounds for the magnitude of such higher-order corrections may be obtained from precision measurements of the corresponding transitions in He-like ions [6]. A measurement on metastable Li^+ is planned in our group [63], the corresponding transitions at 372 nm (UV diode laser wavelength) may be measured in metastable $^{9,10}Be^{2+}$, a comparison of these transitions is given in Table 6.1.
$^{10}Be^{2+}$ shows no hyperfine-structure, which is an advantage on the theoretical side, since the hyperfine-structure is difficult to calculate and introduces additional uncertainty[4]. The higher-order corrections of interest are also more pronounced in Be^{2+}, which relaxes the requirements on experimental precision. A technical advantage may be the possibility to create metastable Be^{2+} ions by electron bombardment of a crystallized Be^+ sample, thus parent ions can be stored, monitored and provide sympathetic cooling at mK temperatures. The main disadvantage is a considerably reduced metastable life-time of 1.8 s in Be^{2+} compared to 49 s in Li^+ [145] (factor 27 in life-time, at a 1.5 times higher scattering rate). The theoretical uncertainty in the 2^3P_0-2^3P_1 fine-structure splitting corresponds to an experimental precision of $\Gamma_{Li}/75$ and $\Gamma_{Be}/5.45$ in terms of the 2^3S - 2^3P linewidth in Li^+ and Be^{2+} (Table 6.1). From this we estimate that spectroscopy on Li^+ requires $(75/5.45)^2 = 190$ times higher count rate to reduce the statistical uncertainty to a given fraction of the theoretical uncertainty limit. The theoretical uncertainties of about 1 MHz in Be^{2+} compared to 50 kHz in Li^+ may also account for significant differences in the investigation of systematic effects, when the transitions are to be measured to a certain fraction of the theoretical uncertainty (compare Section 4.4). The experimental uncertainty of a previous measurement [147] on Be^{2+} is poor (about 3 Γ) and deviates up to 3.5 σ from the more accurate theoretical result (Table 6.1).
A measurement on both metastable $^9Be^{2+}$ and $^{10}Be^{2+}$, as well as $^6Li^+$ and $^7Li^+$, may allow an interesting check of hyperfine-structure corrections in two-electron systems.

[4] Krzysztof Pachucki, private communication.

6.2. A dual frequency trap for ions with large mass difference

The mass range of singly charged ions, which can be simultaneously trapped in a linear Paul trap is limited by their dynamic stability in the RF potential. Can we circumvent this problem?
As a starting point we consider the stability diagram for a single charged particle in a linear quadrupole trap as depicted in Figure 6.4. The stability parameters

$$a = \frac{4QU_{dc}}{m\Omega^2 r_0^2} \quad , \qquad q = \frac{2QU_{rf}}{m\Omega^2 r_0^2} \tag{6.1}$$

are explained in Section 2.1.1. They depend on the trap characteristics (U_i,Ω,r_0) and the charge-to-mass ratio Q/m of the particle. 'a' considers a possible static quadrupole potential, which is usually set to zero in ion trapping and 'q' describes the stability of the particle trajectory in the RF potential. Since the stability diagram contains points where $m \to \infty$ there is no theoretical upper mass limit for single ions in a given RF trap. This case corresponds to vanishing trap potential and a number of 'soft' limits apply. For a practical q-parameter range we quote 0.05-0.4 from a related publication [137], where the upper bound reflects RF heating. In this section we propose a dual frequency trap, which is capable to trap heavy ionic species together with light atomic ions with suitable cycling transitions for laser cooling.

Basic idea

We first investigate the stability diagram for a light coolant species. We apply a RF field to a linear quadrupole trap such that $q_f \approx 0.4$ (f: fast). We add a static quadrupole field, but keep stable trapping conditions for the light species. Now the static quadrupole is slowly varied, hereby we ensure stable trapping conditions at every instant of time (Figure 6.4). We assume that the particle stays trapped also in the dynamic case, which is not necessarily true, for example when the slow frequency is in resonance with the secular oscillation frequency of the light ion.
Now we co-store a much heavier ionic species in the dynamic pseudo-potential, which is created by the adiabatically modulated 'static' quadrupole. The amplitude of the slow RF signal is predefined by the stability condition for the light particle, but the slow frequency may be arbitrarily set to achieve a convenient 'q_s' (s: slow) parameter for the massive ion species. How does the fast RF signal at considerably higher voltage effect the massive particle? The massive ion is inert and barely follows the fast RF oscillation. The case where only the fast field is applied falls within the

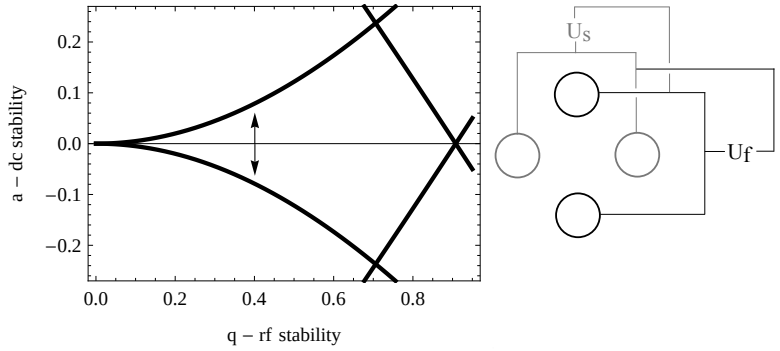

Figure 6.4.: Basic idea. Depicted is the stability diagram for the light cooling species in the radial RF potential of a four rod ion trap. The q parameter ($\propto U_f$) for the light cooling species is set to about 0.4. Then we apply an a value ($\propto U_s$) such that stable trapping of light ions is maintained. Now we adiabatically vary this a value and trap a heavy ion species in the secondary RF potential. The initial RF signal has a considerably higher amplitude than the slow variation and creates an additional, but shallow restoring potential for the heavy ion.

stability diagram for the massive particle, yet the q_f parameter is very low and the fast trap turns out to be shallow for the heavy ion.

Equation of motion

The radial quadrupole potential for a conventional RF trap was given in Equation 2.1 and is now modified to

$$\Phi(x,y,t) = \frac{1}{4r_0^2}[U_s cos(\Omega_s t) + U_f cos(\Omega_f t)](x^2 - y^2), \tag{6.2}$$

again we find the equation of motion from Newtonian mechanics

$$\ddot{x} = -\frac{Q}{2m_i r_0^2}[U_s cos(\Omega_s t) + U_f \cos(\Omega_f t)]x, \tag{6.3}$$

where m_i is either the mass of the heavy or the light species. In analogy to Section 2.1.1 we evaluate stable trajectories separately for a single light ion and a single heavy ion. The limits $m_l \ll m_h$, $\Omega_s \ll \Omega_f$ were discussed above and we expect the trajectories to approximate the motion in the classical quadrupole trap. Equation 6.3 is difficult to solve analytically, so we choose initial conditions and numerically integrate the trajectories. Before we do so we discuss a possible realization of a proof-of-principle experiment.

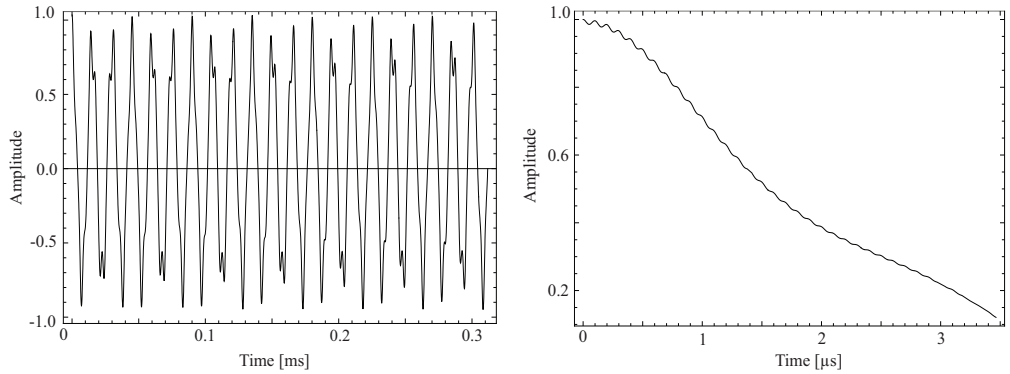

Figure 6.5.: Trajectory of a C_{60}^+ ion in a dual trap ($\Omega_f/2\pi$ = 10 MHz, $\Omega_s/2\pi$ = 289 kHz, U_f = 200 V, U_s = 5 V, r_0 = 1 mm). Left: Single ion trajectory integrated over 90 cycles of the slow radio-frequency Ω_s. Right: Zoom into the first cycle. An oscillation with Ω_f is visible, but the modulation amplitude is small, since the heavy ion is too inert to follow the fast radio-frequency at much higher voltage amplitude U_f. The modulation amplitude vanishes towards the center of the quadrupolar trap.

Proposed proof-of-principle experiment

As light cooling ion we choose either Be^+ or Mg^+, since cooling laser systems are available in our laboratory. An experiment with organic molecular ions like peptides would be of great interest, but is technically demanding. Common loading techniques of heavy organic ions require electron spray ionization, differential pumping and RF ion guides for transport into the experimental section of the trap [150]. $C_{60,70}^+$ fullerenes are medium mass ions which can be conveniently loaded. Fullerenes are available in a UHV-proof solid state phase (powder), they can be evaporated from a conventional atomic oven and ionized by electron impact. Simultaneous trapping of $^{24}Mg^+$ and C_{60}^+ (mass ratio 30) was demonstrated in [151], while the mass ratio of 80 between $^9Be^+$ and C_{60}^+ is beyond current records of RF ion trapping.
For the numerical investigation of Equation 6.3 we separately study single $^{24}Mg^+$ and C_{60}^+ ions. We apply a fast RF signal at $\Omega_f/2\pi$ = 10 MHz to two opposing electrodes of an ideal linear quadrupole trap with r_0 = 1 mm. We choose U_f = 200 V to obtain q_f = 0.4 for $^{24}Mg^+$ ions in the fast trap. The slow RF signal is applied to the otherwise grounded electrode pair (Figure 6.4). At a given signal amplitude U_s we obtain $q_f = q_s$ for

$$\Omega_s = \sqrt{\frac{2QU_s}{m_h q_f r_0^2}}, \tag{6.4}$$

where m_h is the mass of the heavy species. In this example we chose $U_s = U_f/40 = 5$V[5] and obtain q_s = 0.4 at $\Omega_s/2\pi$ = 289 kHz for a C_{60}^+ ion. Such a signal can be gen-

[5]This corresponds to a_f = 0.02, the edge of the stability diagram is a = 0.078 at q = 0.4.

erated directly from a synthesizer. We integrate Equation 6.3 and obtain stable trajectories for single $^{24}Mg^+$ and C_{60}^+ ions in this dual trap (Figure 6.5).
Low drive frequencies and accordingly low voltage amplitudes would prevent trapping of light particles at room temperature, this is different for molecular ions of higher inertial mass. We may estimate the trap depth for C_{60}^+ from the pseudo potential approximation. We rewrite Equation 2.7 in terms of the trap voltage and obtain

$$\Phi = \frac{1}{8} q Q U_i \frac{x^2}{r_0^2}. \tag{6.5}$$

The trap depth is therefore about $U_f/U_s = 40$ times shallower for the heavy species[6]. Since trap depths for light coolant ions exceed 100.000 K we expect that trapping at room temperature is also possible for the heavy ion species. In a large mixed ion sample we expect the formation of a core of laser cooled light ions surrounded by the heavy species. But we may hope for sympathetically cooled heavy ions within a one-dimensional chain of coolant ions, since the axial DC enclosure couples only to the charge of the ion. Here we emphasize the need for low residual RF confinement for the coolant ions, such that we can sufficiently decrease the axial potential to prevent heavy ions from radial displacement.
Molecular dynamics simulations for a conventional Paul trap revealed no upper mass limit for sympathetic cooling of heavy ions with a lighter coolant species [135, 136, 137], since the momentum of a heavy ion is efficiently transfered to a light particles. We expect a similar behavior in the dual trap, but we also point to the large difference in the trap potential. Tightly bound coolant ions may form a crystallized core and act like an effective particle of combined mass and charge. Different regimes may be analyzed in a proof-of-principle experiment and molecular dynamics simulations.
Equation 6.5 is independent of the mass of the heavy ion. When we adapt the slow drive frequency Ω_s according to Equation 6.4 we expect a mass independent trap potential in axial and in radial direction for the heavy species. We conclude that the trapping conditions can be preserved for an unlimited mass range and we may dream of trapping nano-particles and a wide range of organic molecules at mK temperatures.

[6] In case of $^{24}Mg^+/C_{60}^+$ we find a significant contribution from the fast trap to the trap depth of C_{60}^+, this contribution vanishes for heavier species.

6.3. Spectroscopy of dipole-allowed transitions at XUV wavelength

A lively activity in our group is the development of high repetition rate extreme ultraviolet (XUV) frequency comb sources [133, 152]. The goal is a precision measurement of the 1s-2s transition in He^+ at 60 nm, an experiment of great fundamental interest [53]. The output power of state-of-the-art frequency combs at 60 nm is not yet sufficient for this ambitious project. Here we propose a less demanding intermediate spectroscopy experiment based on a deep UV frequency comb and trapped ions. We aim at the wavelengths range between 120 nm and 200 nm, which is favorable for several reasons. We excite dipole-allowed transitions for high event rate and perform spectroscopy on ionic species with cooling transitions, which simplifies an experiment.

Two-photon vs. one-photon spectroscopy

Two-photon spectroscopy with a frequency comb has the advantage that all equally spaced comb modes can add up pairwise to the required transition frequency. Thus the power of the whole comb spectrum may contribute to the excitation [153]. This is a remarkable feature, but the tempting conclusion that frequency combs can only drive two-photon transitions with good efficiency falls short. The two-photon Rabi frequency for the 1s-2s transition in He^+ is given by Equation 3 in [53], with the squared transition matrix element β_{12} from Table I in [53] and assuming an intensity of 10 $\mu W/\mu m^2$ we obtain

$$\Omega = 2(2\pi\beta_{12})I \;=\; 289 \text{ Hz}. \tag{6.6}$$

This might be compared to the scattering rate of a dipole-allowed transition driven by the same laser intensity at 60 nm, which is given by the excitation cross section (Equation 2.15) times the photon flux. Of course only a single comb mode would be resonant to this transition. We consider a spectral bandwidth $\Delta\nu = 3$ THz (150 fs Fourier-limited pulses) at a repetition rate $r_{rep} = 100$ MHz and arrive at a single ion excitation rate

$$r_e = \frac{3\lambda^3 I}{2\pi hc}\frac{r_{rep}}{\Delta\nu} = \; 173 \text{ kHz}, \tag{6.7}$$

for conditions designated for two-photon spectroscopy in He^+. We emphasize that the experimental challenges for one-photon spectroscopy are considerably relaxed. One-photon transitions are not expected to suffer from frequency chirp and do not require spatial and temporal overlap of focused femto-second pulses. In fact, loose focusing optimizes the many-particle excitation rate for dipole-allowed transitions and relaxes alignment issues. An apparent feature of Equation 6.7 is the wavelength

scaling of the excitation rate. A proof-of-principle experiment may be performed at larger wavelength in the 120-200 nm range, in addition we expect higher power levels for low-order harmonics. Transparent media are available in this wavelength range (vacuum windows, lenses) so an experiment does not require differential pumping at the interface between the high harmonic generation chamber (gas jet) and the ion trap. Sympathetic cooling could provide a variety of cold ion samples, yet it is favorable to start with spectroscopy on ions with closed cooling transitions, hereby we optimize the particle number in the interaction volume and simplify the experiment.

Excitation rate

The excitation rate for a large ion sample depends on the number of ions in the focal volume of the laser beam. The focal volume may be approximated by the 1/e area at the minimum beam waist πw_0^2 times the confocal parameter $b = 2z_0 = 2\pi w_0^2/\lambda$. The ion density $n(\omega_s)$ in a Coulomb crystal is given by [154, 155]

$$n(\omega_s) = \frac{2\epsilon_0 m \omega_s^2}{Q^2}, \tag{6.8}$$

it depends on the trap stiffness characterized by the secular frequency ω_s, mass m and charge Q of the ion species. With the single particle excitation rate (Equation 6.7) we obtain the excitation rate

$$R_e = \frac{3\lambda^2 w_0^2 n(\omega_s)}{hc} P(\lambda) \frac{r_{rep}}{\Delta\nu}. \tag{6.9}$$

The excitation rate increases with the wavelength λ, beam waist w_0, laser power $P(\lambda)$, ion density, high repetition rate r_{rep} and small spectral bandwidth $\Delta\nu$.

Example

As an example we evaluate the excitation rate for the $3p_{1/2}$-$4d_{3/2}$ transition in Mg^+ at 173.5 nm (Figure 6.6). The XUV source is a Yb fiber laser frequency comb at 1041 nm, the output of the fiber laser is frequency-doubled and fed into an enhancement resonator, where the third harmonic is produced in a gas jet. The specifications[7] are $P = 6$ mW at the 6th harmonic and 166 fs pulses at a repetition rate of 128 MHz. We assume a spectral bandwidth of 5 THz, which is nearly twice as broad as the Fourier limit. The XUV output coupler, a fused silica plate at Brewster's angle, has poor reflectivity at 173.5 nm. Novel XUV output couplers based on anti-reflection-coated grazing incidence plates are proposed to provide >50% reflectivity

[7] Birgitta Bernhardt, private communication.

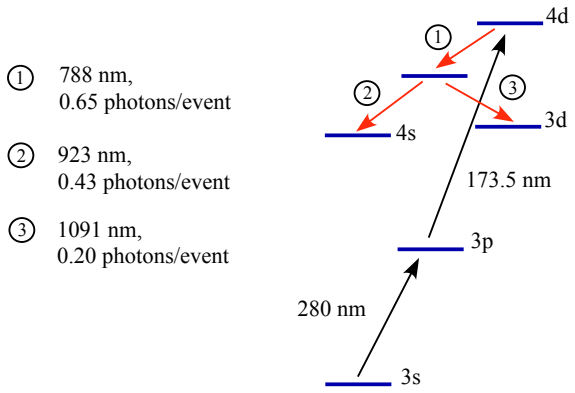

Figure 6.6.: Proposed excitation and detection scheme. Selected Mg^+ energy eigenstates are shown, energy differences are not to scale, fine-structure splittings are neglected. A cw laser slightly red-detuned to the $3s_{1/2}$-$3p_{1/2}$ transition at 280 nm cools the ion sample to mK Temperatures. We further excite to the $4d_{3/2}$ level with a single mode of a deep UV frequency comb at 173.5 nm and record cascading IR photons as low background fluorescence signal. All intermediate energy states have fast decay channels to the ground state.

in the range between 155-175 nm [156], therefore we proceed with a power level of 3 mW after such an output coupler. Further we assume a beam waist of 20 μm, a secular frequency of $\omega_s/2\pi = 1$ MHz and arrive at an excitation rate of about 15 GHz. Hereby we excite about 20.000 ions within $2z_0 = 14$ mm. As signal we employ infra-red photons from the cascading decay of the $4d_{3/2}$ state (Figure 6.6). From an investigation of branching ratios we expect in total 1.28 IR photons per excitation event (0.65 at 788 nm, 0.43 at 923 nm, 0.2 at 1091 nm), thus we obtain a fluorescence rate of 19.2 GHz.
A real experiment will suffer from losses. Optical components at 174 nm will cause significant loss. 20.000 addressed ions is a realistic estimate since we observed up to 10^6 trapped magnesium ions in our six-rod trap [62], but the lengthy interaction volume due to weak focusing at small wavelength might result in poor spatial overlap of the focal volume of the laser beam and an ion crystal. The $3p_{1/2}$ transition is not the ground state in Mg^+, it is the upper level of the D_1 cooling transition and we expect a reduced effective lower state population. We conservatively assume a factor of 10 for each of the three mentioned loss channels. With a detection efficiency of 10^{-3} we arrive at a signal rate of 19.2 kHz for low background, dichroic detection.
From the possible decay channels of the $4d_{3/2}$ transition we infer an upper state linewidth of $\Gamma/2\pi = 19.4$ MHz, thus the repetition rate of 128 MHz is sufficient to resolve the line. The $3p_{1/2}$ line is chosen as intermediate state since excitation to the nearby $4d_{5/2}$ level violates the selection rules for dipole-allowed transitions and only one line would be observed. Addressing the D_1 line with a narrow bandwidth cw-laser also eliminates residual signals from isotopic impurities.

Conclusion

The proposed experiment would be the first spectroscopic measurement with a deep UV frequency comb at full repetition rate. Estimated signal rates seem reasonable and we do not expect technical difficulties on the ion trap side. Especially the $3p_{1/2}$-$4d_{3/2}$ transition in Mg^+ at 173.5 nm looks promising for a proof-of-principle experiment.
With the 7th harmonic of a Ti:Sa frequency comb at 868 nm we may also drive the 3s-4p transitions from the ground-state of Mg^+ at 124 nm, a transition of astrophysical interest. Be^+ shows dipole-allowed transitions at shorter wavelengths, spectroscopy is therefore more demanding. With the 10th harmonic of a frequency comb at 1036 nm we may measure the 2s-3p transitions. Be^+ is a fairly simple atomic system and we could compare a measurement at deep UV frequencies with ab initio calculations here. The spectroscopy technique may also be applied to a variety of sympathetically cooled ion species.

A. Appendix: A pulsed dye laser for photo-ionization of Mg atoms

Cw photo-ionization light for the experiments in Chapter 4 was provided by a Coherent 699 single-frequency ring dye laser, pumped by a Coherent Innova 400 argon ion laser. The optical output at 570 nm was resonantly frequency-doubled to generate light at 285 nm. This laser system caused a lot of maintenance work and it was operated on an interim basis only, as it is dedicated for an experiment with metastable Li^+ ions [63]. So we searched for an alternative photo-ionization light source.
Light at 285 nm or 570 nm is not easily created by simple solid state laser systems[1], but 570 nm is well in the gain profile of efficient Rhodamine dyes, which can be conveniently pumped by green diode pumped solid state (DPSS) lasers. The requirements for a photo-ionization laser are considerably less stringent than for laser cooling or ion manipulation. Pulsed lasers are an attractive option, since their high peak power enables simple and compact designs. Commercial pulsed dye laser systems with narrow linewidth and high output power are available from different companies[2], but they are bulky and expensive. Simple nitrogen laser pumped systems are compact and in-expensive, but offer low average power[3]. We decided to have a home-built dye laser based on a compact DPSS pump laser, an old dye pump and few optical standard components. The system was set up by Camille Estienne in her four months master thesis. The thesis [157] contains a good technical description and a comparative study of different resonator concepts. Here we present the laser in its current, slightly modified setup and depict basic considerations.

Pulsed vs. cw photo-ionization

Based on order of magnitude considerations we interpret the resonant two-photon ionization process as one-photon ionization from a saturated intermediate level for pulsed and cw ionization. For photo-ionization we address the $3s^2\ ^1S$ - $3s3p\ ^1P$ dipole-allowed transition at 285 nm in neutral magnesium (Figure 3.7). The upper

[1] LEDs at 285 nm are available but the optical power of about 1 mW distributed over 10 nm spectral width is not yet promising.
[2] e.g. Radiant Dyes, Sirah, Fine Adjustment.
[3] e.g. LTB Lasertechnik Berlin.

state lifetime is about 2 ns. The corresponding saturation intensity of 4400 W/m^2 is obtained with loosely focused cw-lasers at mW optical power. A pulsed laser strongly saturates the transition and we may assume a mean excited state occupation approaching 1/2, which quickly decays as the pulse is gone. The mean velocity of a ^{24}Mg atom at an oven temperature of 400°C is about 770 m/s, such an atom travels 7.7 μm within a typical pulse duration of 10 ns, which may be neglected against the beam diameter of a loosely focused laser. Particles in the interaction volume may be viewed 'nearly frozen' during one pulse and 'decayed and exchanged' in between pulses at kHz repetition rate. The ionization cross section for the intermediate level is $\sigma = 8.1(2.3)\cdot 10^{-21}\mathrm{m}^2$ measured in a 285 nm magneto-optical trap [71]. We obtain an excited state ionization rate of

$$r_{ion} = \frac{\lambda \sigma P}{2hc\pi\omega_0^2} \tag{A.1}$$

from the photon flux density at laser power P, wavelength λ and beam waist w_0, the factor 1/2 approximates the 3s3p ^{1}P occupation. As saturation condition we require an ionization rate of 100 MHz, which is the inverse duration of a 10 ns pulse. We obtain a saturation intensity of 17.2 GW/m^2, which corresponds, e.g., to $P = 2$ kW at a beam waist of $w_0 = 200$ μm. We do not saturate the ionization step with our high repetition rate system (the peak power of our 532 nm pump pulse is about 25 kW), but we point towards the difference to pulsed lasers with lower repetition rate and higher pulse energy. We maximize pulsed ionization rates by loose focusing, also because the number of addressed atoms increases with w_0^3 while the intensity scales $1/w_0^2$.

Two further differences are associated with pulsed and cw-excitation schemes. We can enhance the cw ionization rate with additional cooling laser photons at 280 nm (Figure 3.7), but the cooling laser intensity is negligible against the peak intensity during a ns-pulse. Second, the spectral overlap between a single frequency cw-laser[4] and the resonant transition is reduced to the ratio between the natural linewidth ($\Gamma/2\pi = 78$ MHz) and the Doppler broadening of 4 GHz at 400°C oven temperature (a reduction due to the atomic beam geometry may apply). Pulsed photo-ionization with a linewidth of several GHz is more efficient here since more velocity classes are saturated.

To summarize: Viewed as an unsaturated one photon transition we expect similar ionization rates for pulsed and cw sources of same average power. In our particular case we expect higher ionization rates for pulsed excitation, due to spectral overlap with several velocity classes of a thermal neutral atom sample. We identify high

[4]Single frequency operation with a typical linewidth of few MHz is required for conventional external SHG cavities, a dedicated cw laser for photo-ionization may be based on intra-cavity frequency doubling, which removes this limitation and the need for electronic stabilization schemes.

average power as main design goal of a pulsed laser source, since the resonant dipole-allowed transition is strongly saturated. Narrow linewidth of a pulsed laser is only required for secondary ambitions like isotope selective trap loading or conversion efficiency in a nonlinear crystal.

Pump laser

The pump laser is an air-cooled, compact Nd:YAG laser for industrial application (Elforlight FQ-500-5-Y-532). The frequency-doubled average power at 532 nm is 0.6 W at 1 kHz and about 2.5 W at 5 kHz repetition rate. The maximum pulse energy is about 0.5 mJ. The pulse duration is 15-30 ns and the output is linearly polarized. The laser is continuously pumped by fiber-coupled cw-laser diodes located in a control box. An intra cavity acousto-optical modulator switches the Q(uality)-factor of the laser resonator. It is externally triggered by TTL pulses and the repetition rate can be set from single shot to 20 kHz. Average power, peak power and the temporal pulse width vary with the power to the pump laser diodes and the repetition rate (see Chapter 3.1.1 in [157] for details). In practice we optimize the pump diode current and the repetition rate with respect to the output power of the dye laser. Thermal effects are the reason why the manufacturer 'optimizes' the laser for a customized repetition rate. Our laser system is optimized for operation at 5 kHz since the company stated that such a laser usually runs equally well at lower repetition rate.

Dye cell

The implementation of the laser medium in cw and gain-switched dye lasers is of fundamental difference, the reason is adverse optical pumping to long-lived triplet states of the dye molecules (compare Section 2.1.2 in [157]). A pulsed laser at low repetition rate may contain a simple sealed cell with dye solution. Efficient operation beyond 100 Hz repetition rate requires a constant exchange of dye molecules, i.e. a moderate flow through such a cell, while cw dye lasers employ a high pressure free-space dye jet for fast exchange. The pump volume of a cw dye laser is 'spot-like' as a consequence, while it is significantly larger in pulsed dye lasers.
Our rectangular Quartz cell[5] is 20 mm long and it is not anti-reflection coated. The dye recipe was optimized in [157], a workable concentration was determined to be 0.15 g Rhodamine 6G solved in 1 l Ethanol.
We pump the dye cell perpendicular to the lasing direction, as it is common in commercial pulsed dye lasers. The pump laser is linearly polarized. The output from the

[5] We found the cell and the pump in our group's storage. The single-speed pump does not allow to adjust the dye flow, but it showed superior performance compared to two other pumps.

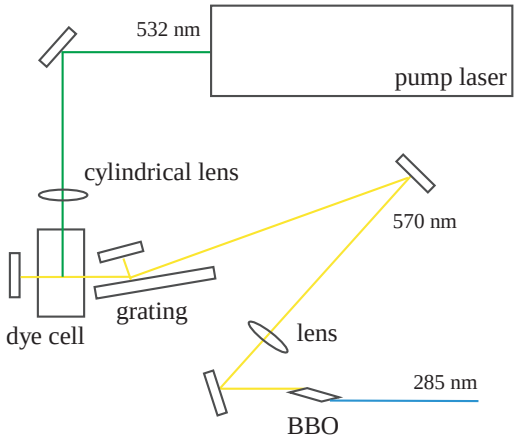

Figure A.1.: Pulsed dye laser. Pulsed operation enables a compact setup, which consists of few optical components only. The pump laser pumps the dye cell from above (the second pump mirror is not shown in this schematic). The heart of the laser system is a Littman type resonator. The first diffraction order of a grazing incidence grating is reflected by a tuning mirror and provides frequency-selective feedback. The zero-order reflection is utilized as an output coupler and focused into a BBO crystal for single-pass frequency doubling.

dye laser is also linear polarized when the pump polarization is perpendicular to the output beam, as depicted in Figures 3.5 to 3.9 in [157], the dye laser is unpolarized when the pump polarization is parallel to the output beam. The efficiency of the grating in the resonator (see Figure A.1) has a strong polarization dependence in grazing incidence. This forced us to tilt either the pump beam or the resonator out of the plane parallel to the optical table. We decided to pump the dye cell from above.
The beam diameter of the pump laser is about 2 mm, in first place we expanded the pump beam to match the pump volume to the 20 mm length of the cell. Later we found more efficient operation at a reduced length of the pump volume and we currently focus the unexpanded 2 mm beam with a single cylindrical lens ($f = 15$ mm).

Resonator

The high gain of the pulsed dye laser results in some remarkable features. The Fresnel reflections from the uncoated rectangular quartz cell form a resonator by themselves and establish a parasitic loss channel. Also amplified spontaneous emission along the prolate pump volume stands in serious competition for the inversion created by the pump pulse[6]. We observed that the output power sharply decreased with increasing cavity length, simply because the inversion is quickly depleted by

[6]Tilting the cell prevents that both effects amplify each other.

parasitic processes. At ns resolution we observed no appreciable build up time (delay between pump and laser pulse) and the temporal characteristic of the dye laser pulse resembled the pump pulse. All resonator mirrors are flat, the cavity operates at the edge of stability and all light is emitted after few round trips.
The current design has a grazing incidence grating as frequency selective element (see Figure A.1). The first diffraction order is fed back by a highly reflective mirror, which can be tilted for frequency tuning, while the zero order reflection is used as output coupler. This approach is commonly know as Littman type laser [158], though it was independently pioneered by Shoshan and co-workers [159]. We choose a 5 cm long holographic aluminum grating with 2400 grooves/mm (Optometrics No 5-2403) to obtain only one propagating diffraction order and a convenient diffraction angle of about 22° for grazing incidence illumination at 570 nm.
The initial design goal was a linewidth smaller than the Doppler broadening of about 4 GHz at 285 nm and 400°C magnesium oven temperature. Hereby we would have obtained some isotope selectivity by predominately loading ^{24}Mg when we set the laser frequency slightly red-detuned to the composite line (the unresolved $^{26-24}$Mg isotope shift is about 1.4 GHz [70]). We observed a single shot linewidth of about 1 GHz at 570 nm and could obtain stable single frequency operation with an additional glass plate in the resonator, but the effective spectral width was always broadened to 5-10 GHz at 570 nm by shot-to-shot frequency jitter [157].
Isotope selectivity can also be obtained by resonant excitation of secular ion motion (Section 3.3.3). Once we omit isotope selectivity we may further relax our requirements on the linewidth, since the resonant dipole-allowed transition is strongly saturated and additional photons are primarily desired for the ionization into the continuum. Different from the setup described in [157] we meanwhile use a smaller dielectric tuning mirror (Thorlabs BB1-E02) and choose a slightly larger incidence angle of about 10°. The change was made to obtain more output power from a more compact setup (suppression of parasitic depletion) and increased feedback from the Littman arrangement (the diffraction efficiency towards grazing incidence drops sharply). Hereby we sacrificed frequency selectivity due to a reduced number of illuminated grooves and the angle dependence of the dispersion in grazing incidence. We measured an output power up to 300 mW at 3 kHz repetition rate, which corresponds to a conversion efficiency of about 10%. The beam profile of the dye laser output is poor, it widely resembles the geometry of the pump volume, which is rectangular due to transverse pumping.

Frequency doubling

For frequency doubling we use a 1 cm long Brewster cut BBO crystal. This crystal was formerly employed in a resonant 560 nm → 280 nm SHG stage. It was exchanged since it showed minor surface defects, which can be tolerated in single-pass

configuration. Different to [157] we focus with a single $f = 10$ mm lens into the crystal. The conversion efficiency is only about 2% to 3%. Disappointing conversion efficiency is a commonly known feature of many pulsed dye lasers due to the deficient beam profile [160].

Photo-ionization

The pulsed dye laser proved to be a reliable photo-ionization system and we demonstrated isotope selective trap loading via secular excitation sweeps (Section 3.3.3). We observed superior performance of our particular pulsed dye laser compared to the former cw dye laser system. The loading rate was enhanced, as a consequence we reduced the electric power to the atom oven from 1 W to about 0.8 W to maintain one-by-one loading of single ions. In contrast to the short-term frequency instabilities we found a good day-to-day reproducibility. We operate the laser for weeks without adjustments, which is a great reduction in maintenance compared to the former system, a particular advantage is the absence of electronic feedback loops. The cw-laser was soon taken out of service and the pulsed dye laser is now our only photo-ionization source.

Outlook

Much of our experience with such laser systems was gathered during setup. Many improvements could be made, if we would re-start from scratch and with custom made components. Superior performance is expected when a shorter, Brewster angled or anti-reflection coated dye cell is used. A more powerful dye pump for high repetition rate operation will likely increase the output power (available e.g. from Sirah, Radiant Dyes).
The most significant improvement is expected from pumping the dye cell collinear with the laser beam, through a custom-made dichroic pump mirror. Collinear pumping is expected to increase the efficiency of the laser itself and greatly improve the beam profile [160]. Good beam profile increases the SHG conversion efficiency and is beneficial for focusing into the trap. A well defined pump volume in the dispersive direction of the grating may speculatively affect the observed frequency instabilities.
A pulsed dye laser is also an attractive approach for resonant photo-ionization of beryllium atoms. The required laser light at 234.8 nm could be obtained by frequency doubling of 469.6 nm light, which is generated with Coumarin 47 as laser dye and a frequency tripled Nd:YAG laser at 355 nm as pump source.

Bibliography

[1] W. Neuhauser, M. Hohenstatt, and P. E. Toschek, "Localized visible Ba^+ mono-ion oscillator," *Phys. Rev. A*, vol. 22, p. 1137–1140, 1980.

[2] R. E. Drullinger, D. J. Wineland, and J. C. Bergquist, "High-Resolution Optical Spectra of Laser Cooled Ions," *Appl. Phys.*, vol. 22, pp. 365–368, 1980.

[3] D. J. Wineland and W. M. Itano, "Spectroscopy of a Single Mg^+ ion," *Phys. Lett.*, vol. 82, pp. 75–78, 1981.

[4] W. Nagourney, G. Janik, and H. Dehmelt, "Linewidth of single laser-cooled $^{24}Mg^+$ ion in a radiofrequency trap," *Proc. Natl. Acad. Sci. USA*, vol. 80, pp. 643–646, 1983.

[5] S. A. Diddams, D. J. Jones, J. Ye, S. T. Cundiff, and J. L. Hall, J. K. Ranka and R. S. Windeler, R. Holzwarth, T. Udem, and T.W. Hänsch, "Direct Link between Microwave and Optical Frequencies with a 300 THz Femtosecond Laser Comb," *Phys. Rev. Lett.*, vol. 84, p. 5102–5105, 2000.

[6] C. Pachucki and V. A. Yerokhin, "Fine Structure of Heliumlike Ions and Determination of the Fine Structure Constant," *Phys. Rev. Lett.*, vol. 104, p. 070403, 2010.

[7] Z.-C. Yan, W. Nörtershäuser, and G. W. F. Drake, "High Precision Atomic Theory for Li and Be^+: QED Shifts and Isotope Shifts," *Phys. Rev. Lett.*, vol. 100, p. 243002, 2008.

[8] J. C. Berengut, V. A. Dzuba, and V. V. Flambaum, "Isotope-shift calculations for atoms with one valence electron," *Phys. Rev. A*, vol. 68, p. 022502, 2003.

[9] V. A. Dzuba, V. V. Flambaum, and J. K. Webb, "Space-Time Variation of Physical Constants and Relativistic Corrections in Atoms," *Phys. Rev. Lett.*, vol. 82, pp. 888–891, 1999.

[10] J. K. Webb, K. John, V. V. Flambaum, C. W. Churchill, M. J. Drinkwater, and J. D. Barrow, "Search for Time Variation of the Fine Structure Constant," *Phys. Rev. Lett.*, vol. 82, pp. 884–887, 1999.

[11] J. C. Berengut and V. V. Flambaum, "Laboratory spectroscopy and the search for variation of the fine-structure constant," *Hyperfine Interactions*, vol. 196, pp. 269–278, 2010.

[12] A. L. Wolf, S. A. van den Berg, C. Gohle, E. J. Salumbides, W. Ubachs, and K. S. E. Eikema, "Frequency metrology on the 4s $^2S_{1/2}$-4p $^2P_{1/2}$ transition in $^{40}Ca^+$ for a comparison with quasar data," *Phys. Rev. A*, vol. 78, p. 032511, 2008.

[13] A. L. Wolf, S. A. van den Berg, W. Ubachs, and K. S. E. Eikema, "Direct Frequency Comb Spectroscopy of Trapped Ions," *Phys. Rev. Lett.*, vol. 102, p. 223901, 2009.

[14] P. O. Schmidt, B. Hemmerling, B. Brandstätter, and D. Nigg, "Quantum Logic for Precision Spectroscopy," *PTB-Mitteilungen*, vol. 119, pp. 54–59, 2009.

[15] M. Herrmann, V. Batteiger, S. Knünz, G. Saathoff, Th. Udem, and T. W. Hänsch, "Frequency Metrology on Single Trapped Ions in the Weak Binding Limit: The $3s_{1/2}$-$3p_{3/2}$ Transition in $^{24}Mg^+$," *Phys. Rev. Lett.*, vol. 102, p. 013006, 2009.

[16] V. Batteiger, S. Knünz, M. Herrmann, G. Saathoff, H. A. Schüssler, B. Bernhardt, T. Wilken, R. Holzwarth, T. W. Hänsch, and Th. Udem, "Precision spectroscopy of the 3s-3p fine-structure doublet in Mg^+," *Phys Rev. A*, vol. 80, p. 022503, 2009.

[17] J. K. Webb, J. A. King, M. T. Murphy, V. V. Flambaum, R. F. Carswell, and M. B. Bainbridge, "Evidence for spatial variation of the fine structure constant," *arXiv:1008.3907v1*, 2010.

[18] T. Ashenfelter, G. J. Mathews, and K. A. Olive, "Chemical Evolution of Mg Isotopes versus the Time Variation of the Fine Structure Constant," *Phys. Rev. Lett.*, vol. 92, p. 041102, 2004.

[19] I. I. Agafonova, P. Molaro, S. A. Levshakov, and J. L. Hou, "First measurement of Mg isotope abundances at high redshifts and accurate estimate of $\Delta\alpha/\alpha$," *Astron. Astrophys.*, vol. 529, p. A28, 2011.

[20] M. P. Ruffoni and J. C. Pickering, "Accurate Laboratory Wavelengths of the 1910 Å Ti II Resonance Transitions Relevant to Studies of Possible Variations of the Fine-Structure Constant," *The Astrophysical Journal*, vol. 725, p. 424–429, 2010.

[21] V. A. Korol and M. G. Kozlov, "Relativistic calculations of isotope shifts in highly charged ions," *Phys. Rev. A*, vol. 76, p. 022103, 2007.

[22] B. K. Sahoo, "Accurate estimate of α variation and isotope shift parameters in Na and Mg^+," *J. Phys. B: At. Mol. Opt. Phys.*, vol. 43, p. 231001, 2010.

[23] A. Krieger, Ch. Geppert, R. Catherall, F. Hochschulz, J. Krämer, R. Neugart, S. Rosendahl, J. Schipper, E. Siesling, Ch. Weinheimer, D. T. Yordanov, and W. Nörtershäuser, "Calibration of the ISOLDE acceleration voltage using a high-precision voltage divider and applying collinear fast beam laser spectroscopy," *Nucl. Instr. Meth. Phys. Res. A*, vol. 632, pp. 23–31, 2011.

[24] K. Vahala, M. Herrmann, S. Knünz, V. Batteiger, G. Saathoff, T.W. Hänsch and Th. Udem, "A phonon laser," *Nat. Phys.*, vol. 5, p. 682, 2009.

[25] S. Knünz, M. Herrmann, V. Batteiger, G. Saathoff, T.W. Hänsch, K. Vahala and Th. Udem, "Injection locking of a trapped-ion phonon laser," *Phys. Rev. Lett.*, vol. 105, p. 013004, 2010.

[26] W. Paul, "Electromagnetic traps for charged and neutral particles," *Rev. Mod. Phys.*, vol. 62, p. 531–540, 1990.

[27] J. D. Prestage, G. J. Dick, and L. Maleki, "New ion trap for frequency standard applications," *J.Appl.Phys.*, vol. 66, pp. 1013–1017, 1989.

[28] G. R. Janik, J. D. Prestage, and L. Maleki, "Simple Analytic Potentials for Linear Ion Traps," *J. Appl. Phys.*, vol. 67, pp. 6050–6055, 1990.

[29] M. G. Raizen, J. M. Gilligan, J. C. Bergquist, W. M. Itano and D. J. Wineland, "Linear trap for high-accuracy spectroscopy of stored ions," *Journal of Mod. Optics*, vol. 39, pp. 233–242, 1992.

[30] W. Neuhauser, M. Hohenstatt, and P. E. Toschek, and H. Dehmelt, "Optical-Sideband Cooling of Visable Atom Cloud Confined in Parabolic Well," *Phys. Rev. Lett.*, vol. 41, no. 4, pp. 233–236, 1978.

[31] D. J. Wineland, R. E. Drullinger, and F. L. Walls, "Radiation-pressure cooling of bound resonant absorbers," *Phys. Rev. Lett.*, vol. 40, pp. 1639–1642, 1978.

[32] W. Nagourney, J. Sandberg, and H. Dehmelt, "Shelved optical electron amplifier: Observation of quantum jumps," *Phys. Rev. Lett.*, vol. 56, p. 2797–2799, 1986.

[33] D. J. Wineland, "Trapped Ions, Laser Cooling, and Better Clocks," *Science*, vol. 226, pp. 395–400, 1984.

[34] F. Diedrich, J. C. Bergquist, W. M. Itano, and D. J. Wineland, "Laser Cooling to the Zero-Point Energy of Motion," *Phys. Rev. Lett.*, vol. 62, pp. 403–406, 1989.

[35] C. Monroe, D. M. Meekhof, B. E. King, S. R. Jefferts, W. M. Itano, D. J. Wineland, and P. L. Gould, "Resolved-Sideband Raman Cooling of a Bound Atom to the 3D Zero-Point Energy," *Phys. Rev. Lett.*, vol. 75, pp. 4011–4014, 1995.

[36] J. I. Cirac and P. Zoller, "Quantum Computations with Cold Trapped Ions," *Phys. Rev. Lett.*, vol. 74, p. 4091–4094, 1995.

[37] D. J. Wineland and D. Leibfried, "Quantum information processing and metrology with trapped ions," *Laser Phys. Lett.*, vol. 8, pp. 175–188, 2011.

[38] D. P. DiVincenzo, "The Physical Implementation of Quantum Computation," *Fortschr. Phys.*, vol. 48, pp. 771–783, 2000.

[39] C. E. Pearson, D. R. Leibrandt, W. S. Bakr, W. J. Mallard, K. R. Brown, and I. L. Chuang, "Experimental investigation of planar ion traps," *Phys. Rev. A*, vol. 73, p. 032307, 2006.

[40] S. Seidelin et al., "Microfabricated Surface-Electrode Ion Trap for Scalable Quantum Information Processing," *Phys. Rev. Lett.*, vol. 96, p. 253003, 2006.

[41] C. W. Chou, D. B. Hume, J. C. J. Koelemeij, D. J. Wineland, and T. Rosenband, "Frequency Comparison of Two High-Accuracy Al^+ Optical Clocks," *Phys. Rev. Lett.*, vol. 104, p. 070802, 2010.

[42] R. Blatt and D. Wineland, "Entangled states of trapped atomic ions," *Nature*, vol. 453, pp. 1008–1015, 2008.

[43] D. Leibfried, R. Blatt, C. Monroe and D. Wineland, "Quantum dynamics of single trapped ions," *Rev. Mod. Phys.*, vol. 75, pp. 281–324, 2003.

[44] F. G. Major, V. N. Gheorghe and G. Werth, *Charged Particle Traps*. Berlin: Springer Series on Atomic, Optical, and Plasma Physics, 1 ed., 2005.

[45] F. Diedrich, E. Peik, J. M. Chen, W. Quint, and H. Walther, "Observation of a Phase Transition of Stored Laser-Cooled Ions," *Phys. Rev. Lett.*, vol. 59, pp. 2931–2934, 1987.

[46] W. Ansbacher, Y. Li, and E. H. Pinnington, "Precision lifetime measurement for the 3p levels of Mg II using frequency-doubled laser radiation to excite a fast ion beam," *Phys. Lett. A*, vol. 139, pp. 165–169, 1989.

[47] W. Demtröder, *Laserspektroskopie*. Berlin: Springer, 4 ed., 2000.

[48] T. W. Hänsch and A. L. Schawlow, "Cooling of Gases by Laser Radiation," *Opt. Commun.*, vol. 13, pp. 68–69, 1975.

[49] D. J. Wineland and D. H. Dehmelt, "Proposed 10^{14} $\Delta\nu/\nu$ laser fluorescence spectroscopy on Ti^+ mono-ion oscillator III," *Bull. Am. Phys. Soc.*, vol. 20, p. 637, 1975.

[50] M. Herrmann, *Precision spectroscopy and optomechanics of single trapped ions in the weak-binding limit.* PhD thesis, Ludwig-Maximilians-Universität, Munich, Germany, 2008.

[51] D. J. Wineland and W. M. Itano, "Laser cooling of atoms," *Phys. Rev. A*, vol. 20, no. 4, pp. 1521–1540, 1979.

[52] W. D. Phillips and H. Metcalf, "Laser Deceleration of an Atomic Beam," *Phys. Rev. Lett.*, vol. 48, pp. 596–599, 1982.

[53] M. Herrmann, M. Haas, U.D. Jentschura, F. Kottmann, D. Leibfried, G. Saathoff, C. Gohle, A. Ozawa, V. Batteiger, S. Knünz, N. Kolachevsky, H.A. Schüssler, T.W. Hänsch and Th. Udem, "Feasibility of coherent xuv spectroscopy on the 1S-2S transition in singly ionized helium," *Phys. Rev. A*, vol. 79, p. 052505, 2009.

[54] G. E. Uhlenbeck and L. S. Ornstein, "On the Theory of the Brownian Motion," *Phys. Rev.*, vol. 36, pp. 823–841, 1930.

[55] R. Blatt, P. Zoller, G. Holzmüller, and I. Siemers, "Brownian Motion of a Parametric Oscillator: A Model for Ion Confinement in Radio Frequency Traps," *Z. Phys. D*, vol. 4, pp. 121–126, 1986.

[56] S. Knünz, *A trapped-ion phonon laser and the detection of ultra-weak forces.* PhD thesis, Ludwig-Maximilians-Universität, Munich, Germany, 2011.

[57] D.F.V. James, "Quantum dynamics of cold trapped ions with application to quantum computation," *Appl. Phys. B*, vol. 66, pp. 181–190, 1998.

[58] A. Friedenauer, F. Markert, H. Schmitz, L. Petersen, S. Kahra, M. Herrmann, Th. Udem, T. W. Hänsch, and T. Schätz, "High power all solid state laser system near 280 nm," *Appl. Phys. B*, vol. 84, no. 3, pp. 371–373, 2006.

[59] F. Markert, "Ein UV-Festkörperlasersystem zur Kühlung von Mg^+-Ionen," Master's thesis, Ludwig-Maximilians-Universität, Munich, Germany, 2005.

[60] T. W. Hänsch and B. Couillaud,, "Laser frequency stabilization by polarization spectroscopy of a reflecting reference cavity," *Opt. Comm.*, vol. 35, pp. 441–444, 1980.

[61] J. Magnes, D. Odera, J. Hartke, M. Fountain, L. Florence, and V. Davis, "Quantitative and Qualitative Study of Gaussian Beam Visualization Techniques," *arXiv:physics/0605102v1*, 2006.

[62] S. Knünz , "Magnesium ions in radio frequency trap," Master's thesis, Ludwig-Maximilians-Universität, Munich, Germany, 2007.

[63] M. Semczuk, "An ion trap for laser spectroscopy on lithium ions," Master's thesis, University of Warsaw, Warsaw, Poland, 2009.

[64] E. A. Donley, T. P. Heavner, F. Levi, M. O. Tataw, and S. R. Jefferts, "Double-pass acousto-optic modulator system," *Rev. Sci. Instrum.*, vol. 76, p. 063112, 2009.

[65] B. Bernhardt, T. W. Hänsch, R. Holzwarth, "Implementation and characterization of a stable optical frequency distribution system," *Optics Express*, vol. 17, pp. 16849–16860, 2009.

[66] M. Prevedelli, T. Freegarde, and T.W. Hänsch, "Phase locking of grating-tuned diode lasers," *Appl. Phys. B*, vol. 60, pp. 241–248, 1995.

[67] V. H. Ludsteck, *Experimente mit einer linearen Ionenkette zur Realisierung eines Quantencomputers*. PhD thesis, Ludwig-Maximilians-Universität, Munich, Germany, 2004.

[68] P. F. Staanum, K. Højbjerre, P. S. Skyt, A. K. Hansen and M. Drewsen, "Rotational laser cooling of vibrationally and translationally cold molecular ions," *Nature Physics*, vol. 6, pp. 271–274, 2010.

[69] K. Hayasaka, "Preparation of an Ion Chain Consisting of Ca^+ and In^+ with a Specified Arrangement," *Lasers and Electro-Optics 2009 and the European Quantum Electronics Conference. CLEO Europe - EQEC 2009. DOI: 10.1109/CLEOE-EQEC.2009.5192357*, 2009.

[70] E. J. Salumbides, S. Hannemann, K. S. E. Eikema and W. Ubachs, "Isotopically resolved calibration of the 285-nm MgI resonance line for comparison with quasar absorptions," *Mon. Not. R. Astron. Soc.*, vol. 373, p. L41–L44, 2006.

[71] D. N. Madsen, and J. W. Thomsen, "Measurement of absolute photo-ionization cross sections using magnesium magneto-optical traps," *J. Phys. B: At. Mol. Opt. Phys.*, vol. 35, pp. 2173–2181, 2002.

[72] N. Kjaergaard, L. Hornekaer, A. M. Thommesen, Z. Videsen, and M. Drewsen, "Isotope selective loading of an ion trap using resonance-enhanced two-photon ionization," *Appl. Phys. B*, vol. 71, p. 207–210, 2000.

[73] S. Gulde, D. Rotter, P. Barton, F. Schmidt-Kaler, R. Blatt, and W. Hogervorst, "Simple and efficient photo-ionization loading of ions for precision ion-trapping experiments," *Appl. Phys. B*, vol. 73, p. 861–863, 2001.

[74] D. M. Lucas, A. Ramos, J. P. Home, M. J. McDonnell, S. Nakayama, J. P. Stacey, S. C. Webster, D. N. Stacey, and A. M. Steane, "Isotope-selective photoionization for calcium ion trapping," *Phys. Rev. A*, vol. 69, p. 012711, 2004.

[75] A. V. Steele, L. R. Churchill, P. F. Griffin, and M. S. Chapman, "Photoionization and photoelectric loading of barium ion traps," *Phys. Rev. A*, vol. 75, p. 053404, 2007.

[76] U. Tanaka, I. Morita, and S. Urabe, "Selective loading and laser cooling of rare calcium isotope $^{43}Ca^{+}$," *Appl. Phys. B*, vol. 89, p. 195–200, 2007.

[77] N. Beverini, E. Macconi, D. Pereira, F. Strumia, G. Vissani and Yu-Zhi Wang, "Wavelength, isotopic shift, and transition rate of the MgI resonance line," *Mon. Not. R. Astron. Soc.*, vol. 77, pp. 299–302, 1990.

[78] U. J. Sofia, J. A. Cardelli, and B. D. Savage, "The Abundant Elements in Interstellar Dust," *The Astrophysical Journal*, vol. 430, pp. 650–666, 1994.

[79] P. M. Gondhalekar and R. Wilson, "The Interstellar Ionization Balance due to Ultraviolet Radiation," *Philosophical Transactions of the Royal Society of London. Series A, Mathematical and Physical Sciences*, vol. 279, pp. 331–336, 1975.

[80] B. D. Savage et al., "The Hubble Space Telescope Quasar Absorption Line Key Project. XV. Milky Way Absorption Lines," *The Astrophysical Journal Supplement Series*, vol. 129, pp. 563–610, 2000.

[81] M. T. Murphy, J. K. Webb, V. V. Flambaum, V. A. Dzuba, C. W. Churchill, J. X. Prochaska, J. D. Barrow, and A. M. Wolfe, "Possible evidence for a variable fine-structure constant from QSO absorption lines: motivations, analysis and results," *Mon. Not. Roy. Astron. Soc.*, vol. 327, pp. 1208–1222, 2001.

[82] S.G. Karshenboim and E. Peik, "An Introduction to Varying Fundamental Constants," *Lecture Notes Phys.*, vol. 648, pp. 1–18, 2004.

[83] J.-P. Uzan, "The fundamental constants and their variation: observational and theoretical status," *Rev. Mod. Phys.*, vol. 75, pp. 403–455, 2003.

[84] J. N. Bahcall and M. Schmidt, "Does the Fine-Structure Constant Vary with Cosmic Time," *Phys. Rev. Lett.*, vol. 19, pp. 1294–1295, 1967.

[85] M. P. Savedoff, "Physical Constants in Extra-Galactic Nebulae," *Nature*, vol. 178, pp. 688–689, 1956.

[86] A. M. Wolfe, R. L. Brown, and M. S. Roberts, "Limits on the Variation of Fundamental Atomic Quantities over Cosmic Time Scales," *Phys. Rev. Lett.*, vol. 37, pp. 179–181, 1976.

[87] H. Chand, P. Petitjean, R. Srianand and B. Aracil, "Probing the time-variation of the fine-structure constant: Results based on Si IV doublets from a UVES sample," *Astron. Astrophys.*, vol. 430, pp. 47–58, 2005.

[88] M. T. Murphy, J. K. Webb, V. V. Flambaum, J. X. Prochaska and A. M. Wolfe, "Further constraints on variation of the fine-structure constant from alkali-doublet QSO absorption lines," *Mon. Not. Roy. Astron. Soc.*, vol. 327, p. 1237–1243, 2001.

[89] L. D. Thong, T. van Hung, N. T. T. Huong, and H. H. Bang, "Constraining the Cosmological Time Variation of the Fine - Structure Constant," *Astrophysics*, vol. 53, pp. 446–452, 2010.

[90] M. T. Murphy, J. K. Webb, V. V. Flambaum, "Further evidence for a variable fine-structure constant from Keck/HIRES QSO absorption spectra," *Mon. Not. Roy. Astron. Soc.*, vol. 345, pp. 609–638, 2003.

[91] J. K. Webb, M.T. Murphy, V.V. Flambaum, V. A. Dzuba, J. D. Barrow, C.W. Churchill, J. X. Prochaska, and A. M. Wolfe, "Further Evidence for Cosmological Evolution of the Fine Structure Constant," *Phys. Rev. Lett.*, vol. 87, p. 091301, 2001.

[92] M. T. Murphy, V. V. Flambaum, J. K. Webb, V. V. Dzuba, J. X. Prochaska and A. M. Wolfe, "Constraining Variation in the Fine-Structure Constant, Quark Masses and the Strong Interaction," *Lecture Notes Phys.*, vol. 648, pp. 131–150, 2004.

[93] R. Srianand, H. Chand, P. Petitjean and B. Aracil, "Limits on the Time Variation of the Electromagnetic Fine-Structure Constant in the Low Energy Limit from Absorption Lines in the Spectra of Distant Quasars," *Phys. Rev. Lett.*, vol. 92, p. 121302, 2004.

[94] M. T. Murphy, J. K. Webb, V. V. Flambaum, "Revision of VLT/UVES constraints on a varying fine-structure constant," *Mon. Not. Roy. Astron. Soc.*, vol. 384, pp. 1053–1062, 2008.

[95] Y. Fenner, M. T. Murphy, and B. K. Gibson, "On variations in the fine-structure constant and stellar pollution of quasar absorption systems," *Mon. Not. Roy. Astron. Soc.*, vol. 358, p. 468–480, 2005.

[96] M. T. Murphy, J. K. Webb, V. V. Flambaum, C. W. Churchill and J. X. Prochaska, "Possible evidence for a variable fine-structure constant from QSO absorption lines: systematic errors," *Mon. Not. Roy. Astron. Soc.*, vol. 327, p. 1223–1236, 2001.

[97] M. G. Kozlov, V. A. Korol, J. C. Berengut, V. A. Dzuba, and V. V. Flambaum, "Space-time variation of the fine-structure constant and evolution of isotope abundances," *Phys. Rev. A*, vol. 70, p. 062108, 2004.

[98] W. M. Itano, J. C. Bergquist, and D. J. Wineland, "Frequency Ratio of Al^+ and Hg^+ Single-Ion Optical Clocks; Metrology at the 17th Decimal Place," *Science*, vol. 319, pp. 1808–1812, 2008.

[99] J. C. Berengut and V. V. Flambaum, "Astronomical and laboratory searches for space-time variation of fundamental constants," *arXiv:1009.3693v1*, 2010.

[100] W. M. Itano, J. C. Bergquist, and D. J. Wineland, "Laser Spectroscopy of Trapped Atomic Ions," *Science*, vol. 237, pp. 612–617, 1987.

[101] J. C. Bergquist, W. M. Itano, and D. J. Wineland, "Recoilless optical absorption and Doppler sidebands of a single trapped ion," *Phys. Rev. A*, vol. 36, p. 428–430, 1987.

[102] T. Nakamura, et al., "Laser spectroscopy of $^{7,10}Be^+$ in an online ion trap," *Phys. Rev. A*, vol. 74, p. 052503, 2006.

[103] J. C. Pickering, A. P. Thorne, and J. K. Webb, "Precise laboratory wavelengths of the Mg I and Mg II resonance transitions at 2853, 2803 and 2796 Å," *Mon. Not. Roy. Astron. Soc.*, vol. 300, pp. 131–134, 1998.

[104] J. C. Pickering, A. P. Thorne, J. E. Murray, U. Litzen, S. Johansson, V. Zilio, and J. K. Webb, "Accurate laboratory wavelengths of some ultraviolet lines of Cr, Zn and Ni relevant to time variations of the fine structure constant," *Mon. Not. Roy. Astron. Soc.*, vol. 319, pp. 163–167, 2000.

[105] M. Aldenius, S. Johansson, and M. T. Murphy, "Laboratory wavelengths for cosmological constraints on varying fundamental constants," *Mon. Not. Roy. Astron. Soc.*, vol. 370, pp. 444–452, 2006.

[106] M. Aldenius, "Accurate laboratory ultraviolet wavelengths for quasar absorption-line constraints on varying fundamental constants," *Phys. Scr.*, p. 014008, 2009.

[107] G. W. F. Drake, *Handbook of Atomic, Molecular, and Optical Physics*. Springer, 2006.

[108] G. Audi, A. H. Wapstra, and C. Thibault, "The AME2003 atomic mass evaluation," *Nuclear Physics A*, vol. 729, p. 337–676, 2003.

[109] M. S. Safronova, and W. R. Johnson, "Third-order isotope-shift constants for alkali-metal atoms and ions," *Phys. Rev. A*, vol. 64, p. 052501, 2001.

[110] I. I. Tupitsyn, V. M. Shabaev, J. R. Crespo Lopez-Urrutia, I. Draganic, R. Soria Orts, and J. Ullrich, "Relativistic calculations of isotope shifts in highly charged ions," *Phys. Rev. A*, vol. 68, p. 022511, 2003.

[111] I. Angeli, "A consistent set of nuclear rms charge radii: properties of the radius surface R(N,Z)," *Atomic Data and Nuclear Data Tables*, vol. 87, p. 185–206, 2004.

[112] I. N. Boboshin, V. V. Varlamov, Yu. P. Gangrsky, B. S. Ishkhanov, S. Yu. Komarov, K. P. Marinova, "New Nuclear Charge Radii Database, http://cdfe.sinp.msu.ru/services/radchart/radmain.html," *Bulletin of the Russian Academy of Sciences: Physics*, vol. 73, p. 810–815, 2009.

[113] W. M. Itano and D. J. Wineland, "Precision measurement of the ground-state hyperfine constant of $^{25}Mg^{+}$," *Phys. Rev. A*, vol. 20, pp. 1364–1373, 1979.

[114] C. Sur, B. K. Sahoo, R. K. Chaudhuri, B. P. Das, and D. Mukherjee, "Comparative studies of the magnetic dipole and electric quadrupole hyperfine constants for the ground and low lying excited states of $^{25}Mg^{+}$," *Eur. Phys. J. D*, vol. 32, p. 022103, 2005.

[115] B. K. Mani and D. Angom, "Atomic properties calculated by relativistic coupled-cluster theory without truncation: Hyperfine constants of Mg^{+}, Ca^{+}, Sr^{+}, and Ba^{+}," *Phys. Rev. A*, vol. 81, p. 042514, 2010.

[116] M. S. Safronova, A. Derevianko, and W. R. Johnson, "Relativistic many-body calculations of energy levels, hyperfine constants, and transition rates for sodiumlike ions," *Phys. Rev. A*, vol. 58, pp. 1016–1028, 1998.

[117] J. R. de Laeter, J. K. Böhlke, P. de Bievre, H. Hidaka, H. S. Peiser, K. J. R. Rosman, and P. D. P. Taylor, "Atomic Weigths of the Elements," *Pure Appl. Chem.*, vol. 75, p. 683–800, 2003.

[118] I. I. Sobelman, *Atomic Spectra and Radiative Transitions*. Springer, 1996.

[119] S. Hannemann, E. J. Salumbides, S. Witte, R. Th. Zinkstok, E.-J. van Duijn, K. S. E. Eikema, and W. Ubachs, "Frequency metrology on the Mg $3s^2$ $^1S \rightarrow 3s4p$ ^1P line for comparison with quasar data," *Phys. Rev. A*, vol. 74, p. 012505, 2006.

[120] G. Nave and C. J. Sansonetti, "Wavelengths of the $3d^6(^5D)4s\ a^6D$ - $3d^5(^6S)4s4p\ y^6P$ multiplet of Fe II (UV 8)," *J. Opt. Soc. Am. B*, vol. 28, p. 737–745, 2011.

[121] D. L. Moehring, B. B. Blinov, D. W. Gidley, R. N. Kohn, Jr., M. J. Madsen, T. D. Sanderson, R. S. Vallery, and C. Monroe, "Precision lifetime measurements of a single trapped ion with ultrafast laser pulses," *Phys. Rev. A*, vol. 73, p. 023413, 2006.

[122] S. Olmschenk, D. Hayes, D. N. Matsukevich, P. Maunz, D. L. Moehring, K. C. Younge, and C. Monroe, "Measurement of the lifetime of the $6p\ ^2P_{1/2}$ level of Yb^+," *Phys. Rev. A*, vol. 80, p. 022502, 2009.

[123] W. W. Smith and A. Gallagher, "Radiative Lifetime of the First $^2P_{3/2}$ State of Ionized Calcium and Magnesium by the Hanle Effect," *Phys. Rev.*, vol. 145, pp. 26–35, 1965.

[124] W. H. Smith and H. S. Liszt, "Absolute Oscillator Strengths for Some Resonance Multiplets of Ca I,II, Mg I,II, B I, and Al I," *J. Opt. Soc. Am.*, vol. 61, pp. 938–941, 1971.

[125] H. G. Berry, J. Bromander, and R. Buchta, "Some Mean Life Measurements in the NaI and MgI Isoelectronic Sequences," *Physica Scripta*, vol. 1, pp. 181–183, 1970.

[126] T. Andersen, J. Desesquelles, K. A. Jessen and G. Sorensen, "Measurements of Atomic Lifetimes for Neutral and Ionized Magnesium and Calcium," *J. Quant. Spectrosc. Radiat. Transfer.*, vol. 10, pp. 1143–1150, 1970.

[127] L. Lundin, B. Engman, J. Hilke and I. Martinson, "Lifetime Measurements in Mg I-Mg IV," *Physica Scripta*, vol. 8, pp. 274–278, 1973.

[128] L. Liljeby, A. Lindgard, S. Mannervik, E. Veje, and B. Jelenkovic, "Lifetimes in Mg I and Mg II; Beam-Foil Measurements and Numerical Coulomb-Approximation Calculations," *Physica Scripta*, vol. 21, pp. 805–810, 1980.

[129] R. Adler, "A Study of Locking Phenomena in Oscillators," *Proc. IRE*, vol. 34, no. 6, pp. 351 – 357, 1946.

[130] R. Maiwald, D. Leibfried, J. Britton, J. C. Bergquist, G. Leuchs and D. J. Wineland, "Stylus ion trap for enhanced access and sensing," *Nat. Phys.*, vol. 5, pp. 551–554, 2009.

[131] M. J. Biercuk, Hermann Uys, J. W. Britton, A. P. VanDevender, and J. J. Bollinger, "Ultrasensitive detection of force and displacement using trapped ions," *Nat. Nanotech.*, vol. 5, p. 646–650, 2010.

[132] P. B. Corkum, "Plasma Perspective on Strong-Field Multiphoton Ionization," *Phys. Rev. Lett.*, vol. 71, pp. 1994–1997, 1993.

[133] Christoph Gohle, Thomas Udem, Maximilian Herrmann, Jens Rauschenberger, Ronald Holzwarth, Hans A. Schuessler, Ferenc Krausz, and Theodor W. Hänsch, "A frequency comb in the extreme ultraviolet," *Nature*, vol. 436, pp. 234–237, 2005.

[134] R. J. Jones, K. D. Moll, M. J. Thorpe, and J. Ye, "Phase-Coherent Frequency Combs in the Vacuum Ultraviolet via High-Harmonic Generation inside a Femtosecond Enhancement Cavity," *Phys. Rev. Lett.*, vol. 94, p. 193201, 2005.

[135] T. Baba and I. Waki, "Sympathetic cooling rate of gas-phase ions in a radio-frequency-quadrupole ion trap," *Appl. Phys. B*, vol. 74, pp. 375–382, 2002.

[136] T. J. Harmon, N. Moazzan-Ahmadi, and R. I. Thompson, "Instability heating of sympathetically cooled ions in a linear Paul trap," *Phys Rev. A*, vol. 67, p. 013415, 2003.

[137] S. Schiller and C. Lämmerzahl, "Molecular dynamics simulation of sympathetic crystallization of molecular ions," *Phys Rev. A*, vol. 68, p. 053406, 2003.

[138] K. Okada, M. Wada, T. Takayanagi, S. Ohtani, and H. A. Schuessler, "Characterization of ion Coulomb crystals in a linear Paul trap," *Phys. Rev. A*, vol. 81, p. 013420, 2010.

[139] A. C. Wilson, C. Ospelkaus, A. P. VanDevender, J. A. Mlynek, K. R. Brown, D. Leibfried, and D. J. Wineland, "A 750 mW, continuous-wave, solid-state laser source at 313 nm for cooling and manipulating trapped $^{9}Be^{+}$ ions," *arXiv:1105.5356v1*, 2011.

[140] R. W. Boyd, *Nonlinear Optics*. Academic Press, 2nd ed., 2003.

[141] Y. F. Chen and Y. C. Chen, "Analytical functions for the optimization of second-harmonic generation and parametric generation by focused Gaussian beams," *Appl. Phys. B*, vol. 76, p. 645–647, 2003.

[142] A. H. F. v. M. M. Brieger, H. Busener and A. Renn, "Enhancement of Single Frequency SHG in a Passive Ring Resonator," *Opt. Commun.*, vol. 38, pp. 423–426, 1981.

[143] D. J. Wineland, J. J. Bollinger, and W. M. Itano , "Laser-Fluorescence Mass Spectroscopy," *Phys. Rev. Lett.*, vol. 50, pp. 623–626, 1983.

[144] W. Nörtershäuser et al., "Nuclear Charge Radii of ^{7,9,10}Be and the One-Neutron Halo Nucleus ^{11}Be," *Phys. Rev. Lett.*, vol. 102, p. 062503, 2009.

[145] G. W. F. Drake, "Theory of Relativistic Magnetic Dipole Transitions: Lifetime of the Metastable 2 ^{3}S State of the Heliumlike Ions," *Phys. Rev. A*, vol. 3, pp. 908–915, 1971.

[146] E. Riis, A. G. Sinclair, O. Poulsen, G. W. F. Drake, W. R. C. Rowley, and A. P. Levick, "Lamb shifts and hyperfine structure in $^6Li^+$ and $^7Li^+$: Theory and experiment," *Phys. Rev. A*, vol. 49, pp. 207–220, 1994.

[147] T. J. Scholl, R. Cameron, S. D. Rosner, L. Zhang, R. A. Holt, C. J. Sansonetti, and J. D. Gillaspy, "Precision Measurement of Relativistic and QED Effects in Heliumlike Beryllium," *Phys. Rev. Lett.*, vol. 71, pp. 2188–2191, 1993.

[148] K. T. Chung and X.-W. Zhu, "Energies, fine structures, and isotope shifts of the $1s^22snl$ excited states of the beryllium atom," *Phys. Rev. A*, vol. 48, pp. 1944–1954, 1993.

[149] M. Smiciklas and D. Shiner, "Determination of the Fine Structure Constant Using Helium Fine Structure," *Phys. Rev. Lett.*, vol. 105, p. 123001, 2010.

[150] D. Offenberg, C. B. Zhang, Ch. Wellers, B. Roth, and S. Schiller, "Translational cooling and storage of protonated proteins in an ion trap at subkelvin temperatures," *Phys. Rev. A*, vol. 78, p. 061401, 2008.

[151] V. L. Ryjkov, X. Zhao, and H. A. Schuessler, "Sympathetic cooling of fullerene ions by laser-cooled Mg^+ ions in a linear rf trap," *Phys. Rev. A*, vol. 74, p. 023401, 2006.

[152] A. Ozawa et al., "High Harmonic Frequency Combs for High Resolution Spectroscopy," *Phys. Rev. Lett.*, vol. 100, p. 253901, 2008.

[153] J. N. Eckstein, A. I. Ferguson, and T. W. Hänsch, "High-Resolution Two-Photon Spectroscopy with Picosecond Light Pulses," *Phys. Rev. Lett.*, vol. 40, pp. 847–850, 1978.

[154] L. Hornekær, N. Kjærgaard, A. M. Thommesen, and M. Drewsen, "Structural Properties of Two-Component Coulomb Crystals in Linear Paul Traps," *Phys. Rev. Lett.*, vol. 86, pp. 1994–1997, 2001.

[155] L. Hornekær, *Single- and Multi-Species Coulomb Ion Crystals: Structures, Dynamics and Sympathetic Cooling*. PhD thesis, University of Aarhus, Aarhus, Denmark, 2000.

[156] Oleg Pronin, Vladimir Pervak, Ernst Fill, Jens Rauschenberger, Ferenc Krausz, and Alexander Apolonski, "Ultrabroadband efficient intracavity XUV output coupler," *Optics Express*, vol. 19, pp. 10232–10240, 2011.

[157] C. Estienne, "A pulsed dye laser for photo-ionization of magnesium atoms," Master's thesis, Swiss Federal Institute of Technology, Zürich, Switzerland, 2009.

[158] M. G. Littman and H. J. Metcalf, "Spectrally narrow pulsed dye laser without beam expander," *Appl. Opt.*, vol. 17, pp. 2224–2227, 1978.

[159] I. Shoshan, N. N. Danon, und U. P. Oppenheim, "Narrowband expansion of a pulsed dye laser without intracavity beam expansion," *J. of Appl. Phys.*, vol. 48, no. 11, pp. 4495–4497, 1977.

[160] U. Brackmann, *Lambdachrome, Laser Dyes.* Göttingen, Germany: Lambda Physik AG, 2000.